Investigations into the Natural Variation of Pyrite Reactivity

Thesis submitted to the School of Chemical and Physical Sciences, Faculty of Science and Engineering, Flinders University in fulfilment of the requirements for the degree of Doctor of Philosophy

Owen D. Osborne

BTech (Forens&AnalytChem), BSc (Hons)

Flinders
UNIVERSITY

Flinders University, South Australia

Faculty of Science and Engineering

School of Chemical and Physical Sciences

June 2013

Declaration

"I certify that this thesis does not incorporate without acknowledgment any material previously submitted for a degree or diploma in any university; and that to the best of my knowledge and belief it does not contain any material previously published or written by another person except where due reference is made in the text."

_____on_____

Owen D. Osborne

Acknowledgements

I would first like to acknowledge that acknowledgements are hard, to say something meaningful about all of the people who have aided me and supported me over the past 5 or so years would be no small feat. So to anyone who I don't mention specifically, thank you, the journey wouldn't have been the same without you.

Primarily, I would like to thank my principal supervisor Associate Professor Claire Lenehan. I cannot thank you enough for the knowledge, guidance and support you have provided, from my undergraduate degree right through to the production of this tome. You are undoubtedly the person from whom I have learnt the most and your encouragement and positive attitude have been invaluable to my motivation and self-confidence.

Thank you to my co-supervisor Professor Allan Pring. The depth and breadth of your knowledge amazes me, and I have benefitted immensely from your expertise. The experience I have gained from working with you over the past few years has been invaluable.

To Dr Rachel Popelka-Filcoff, thank you for offering your expertise in the collection and analysis of my neutron activation analysis data, your enthusiasm and friendliness made learning from you a pleasure.

I would like to thank the staff at Adelaide Microscopy, in particular Aoife McFadden, for her help with sample preparation, data collection and for putting up with my numerous requests for instrument time.

I would like to acknowledge my fellow students, past and present, for making my time at Flinders that much more enjoyable. Special mention must go to Darko Bogdanovic for teaching me to use LabVIEW and introducing me to a music genre I can only describe as Serbian gypsy punk. To my longest serving office mates Christine Ta and Jessirie Dilag, thank you for your moral support, for feeding me, and generally looking after me, without you I would have probably lost the plot a long time ago. To my substitute office mates Rachel Hughes and Andrew Blok, thank you for your help and enduring friendship over the years.

To my Mum, Dad, Brother and Sister, your support and confidence in me has always been beyond reproach, I love the lot of you.

The partners of postgraduate students have a very real and well established role; to provide unwavering support, absolute understanding and, at a very specific point, the statement *“just finish it already!”* spoken through gritted teeth, and I want to thank you, Kate for fulfilling your duties to perfection. I couldn’t have done it without you.

So in the words of the great John Cleese: *“And now for something completely different...”*

Dedicated to my family.

Contents

Publications from this Thesis

1. Osborne, O.D., Pring, A., and Lenehan, C.E., *A simple colorimetric FIA method for the determination of pyrite oxidation rates.* Talanta, **2010**. 82(5), p.1809-1813.

2. Osborne, O.D., Pring, A., Popelka-Filcoff, R.S., Bennett, J.W., Stopic, A., Glascock, M.D., and Lenehan, C.E., *Comparison of the relative comparator and k0 neutron activation analysis techniques for the determination of trace-element concentrations in pyrite.* Mineralogical Magazine, **2012**. 76(5), p.1229-1245.

Summary

Pyrite (FeS_2) is widely accepted to be the most abundant sulfide mineral on the surface of the planet and its abundance in mining waste is well established. The significance of pyrite lies in its potential to oxidise in the environment and cause a process called acid mine drainage. It has been observed that pyrites from different geographical locations will undergo oxidation at different rates, however, the reasons for this are not well understood. This thesis presents investigations into the proposed variation of pyrite reactivity and the mineral characteristics which may contribute to this variation.

A method for the rapid determination of the oxidation rate of naturally occurring pyrite samples was developed. The progress of the oxidation reaction was followed by measurement of the concentration of total dissolved Fe using flow injection analysis. Iron was determined using ultraviolet-visible detection after reaction with the colorimetric reagent 5-sulfosalicylic acid in the presence of ammonia. The calibration function was linear between 5 and 150mg.L^{-1}, and the detection limit was 0.46mg.L^{-1}. The relative standard deviation was typically less than 1% (n=10) and the measurement frequency was 60 per hour. The method was used to quantify the oxidation rate of 40 ground and cleaned pyrite samples (53µm<x<106µm) from various international locations that were subjected to accelerated oxidation in acidic hydrogen peroxide. Results of these experiments showed over a 6-fold difference in oxidation rates across the pyrite samples.

Thirty pyrite samples from a range of geological locations were analysed using relative comparator and k_0-NAA (neutron activation analysis) at MURR (University of Missouri Research Reactor, Columbia, Missouri, USA) and ANSTO (Australian Nuclear Science and Technology Organisation, Lucas Heights, NSW, Australia) respectively. In general, statistical analysis of the trace element data for the two methods showed a good correlation, with the majority of elemental concentrations of paired data reported by MURR and ANSTO being indistinguishable at the 0.05 significance level. Comparison of results presented here for pyrite from Victoria Mine (Spain) compared well

with previously published NAA data. Both methods show applicability to the trace element analysis of pyrite.

The trace element data for the samples, collected by NAA was compared to their measured semiconductor types. The results showed that p-type samples generally had an abundance of hole donating impurities while n-type pyrites generally had an abundance of electron donating impurities. Semiconducting type was compared with the reactivity of the samples and no correlation was observed. Interestingly, the inclusion of elements common in clay and silicate layer minerals was found to correlate with sample reactivity. By investigating the geology of samples with large and small measured reactivities a trend emerged indicating that samples from sedimentary origins were significantly more reactive than those from higher temperature hydrothermal origins.

Figures

Tables

Equations

Mechanisms

Abbreviations

%	percent
%RSD	percentage relative standard deviation
%v/v	percent volume for volume
%w/v	percent weight for volume
%w/w	percent weight for weight
°C	degrees Celsius
<	less than
>	greater than
Å	Angstrom
a_0	unit cell dimension
AAS	atomic absorption spectroscopy
AINSE	Australian Institute for Nuclear Science and Engineering
AMD	acid mine drainage
ANSTO	Australian Nuclear Science and Technology Organisation
BET	Brunauer–Emmett–Teller
BSE	backscattered electron
cm	centimetre
$cm^{-2}.s^{-1}$	per centimetre per second
conc.	concentration
CPS	counts per second
DC	direct current
e^-	electron
EDS	energy dispersive X-ray spectrometer
EMF	electromotive force
eV	electron volt
FIA	flow injection analysis
g	gram
h	hour
Hz	hertz
i.d.	internal diameter
i.f	in-line filter
ICP	inductively coupled plasma
ICP-AES	inductively coupled plasma atomic emission spectrometry
ICP-MS	inductively coupled plasma mass spectrometry
$J.cm^{-2}$	joules per centimetre squared
k	rate constant
Kbar	kilobar
km	kilometre
KV	kilovolts
L	litre
LA-ICP-MS	laser ablation inductively coupled plasma mass spectrometry
LTM	Leadville type mineralisation
LOD	limit of detection
LOQ	limit of quantitation

m	metre
M	molar
$M^{-1}.cm^{-1}$	per molar per centimetre
$m^2.g^{-1}$	metres squared per gram
Ma	megaannum
mg	milligram
$mg.L^{-1}$	milligrams per litre
min	minute
mJ	millijoule
mL	millilitre
$mL.min^{-1}$	millilitres per minute
mm	millimetre
$mmol.kg^{-1}$	millimole per kilogram
$mol.kg^{-1}$	mole per kilogram
$mol.L^{-1}.min^{-1}$	moles per litre per minute
moles $pyrite.h^{-1}.g^{-1}$	moles of pyrite per hour per gram
MURR	University of Missouri research reactor
mV	millivolt
MΩ	mega ohm
n-type	negative type
nA	nanoamp
NAA	neutron activation analysis
ND	not detected
nm	nanometre
OPAL	open pool Australian lightwater (reactor)
p-type	positive type
PAP	Pouchou and Pichoir
ppb	parts per billion
ppm	parts per million
PT	pressure and temperature
QC	quality control
RM	reference material
s	second
SEM	scanning electron microscope
SRM	standard reference material
UV	ultra violet
Unc.	uncertainty
USGS	United States Geological Survey
UV-VIS	ultra violet-visible
vs.	versus
WDS	wavelength dispersive spectroscopy
XPS	X-ray photoelectron spectroscopy
XRD	X-ray diffraction
XRF	X-ray fluorescence
µL	microlitre
µm	micrometre
µM	micromolar

$\mu M.h^{-1}.g^{-1}$	micromolar per hour per gram
$\mu M.L^{-1}$	micrograms per litre
$\mu mol.kg^{-1}$	micromole per kilogram
$\mu mol.L^{-1}.min^{-1}$	micromolar per litre per minute
$\Omega^{-1}.cm^{-1}$	per ohm per centimetre

Chemical abbreviations

5-SSA	5-sulfosalicylic acid
CoS_2	colbalt sulfide
$Fe(OH)_3$	ferric hydroxide
$Fe(SSA)_3$	acidic iron-sulfosalicylic acid complex
Fe^{2+}	ferrous iron
Fe^{3+}	ferric iron
FeAsS	arsenopyrite
FeS_2	pyrite / iron disulfide
$FeSO_4$	iron sulfate
$FeSO_4.7H_2O$	melanterite
FeSSA	basic iron-sulfosalicylic acid complex
H^+	proton
H_2O	water
H_2O_2	hydrogen peroxide
HCl	hydrocholric acid
HO_2^-	hydroperoxyl ion
NaCl	sodium chloride
O_2	oxygen
$O2^-$	superoxide anion
OH•	hydroxide radical
OH^-	hydroxide anion
PTFE	polytetrafluoroethylene
PVC	polyvinylchloride
S_2^{2-}	disulfide ion
$S_2O_3^{2-}$	thiosulfate
SO_4^{-2}	sulfate
ZnS	zinc sulfide

Chapter 1

Introduction

1.1 Introduction

Pyrite (iron disulfide, FeS_2) is a mineral in the sulfide group of minerals. Pyrite has been known since ancient times and was described even in early Greek works [1]. The name derives from the Greek word *πνρ* meaning fire, owing to the fact that it produced sparks when struck with flint (leading to its later use in flint-lock muskets). The fact that we have known about pyrite for such a length of time is not surprising as it is widely acknowledged as one of, if not the most abundant and widespread of the sulfide minerals on the Earth's surface [2-7]. The abundance of pyrite and its association with coals and mineral ores [8] means that humans have been digging it out of the ground for millennia. At one time, pyrite was mined and used as a major source of iron sulfate for making dyes, inks and sulfuric acid [9], however, as technology advanced and different, more efficient ways of producing these chemicals were discovered, pyrite became a waste product of mining processes.

In nature the oxidation of pyrite is thought to be an important natural process which links global sulfur, oxygen, iron and carbon cycles [10]. However, anthropological inputs such as mining create conditions where the rate of oxidation of pyrite is accelerated immensely. In the process of extracting the pyrite from the more valuable ores with which it is associated, it is crushed and discarded to waste heaps. The enormous increase in surface area coupled with exposure to water and air increases the rate of pyrite oxidation to a point where environmental problems begin to arise. In the case of pyrite oxidation, the problem takes the form of a process called acid mine drainage (AMD), where large quantities of acid are produced and are discharged into the surrounding environment. The natural oxidation of pyrite is known to proceed via the stoichiometric reactions presented in Equations 1.1, 1.2, 1.3 1.4 [11]. These reactions are initiated by contact of pyrite with dissolved oxygen and water.

As oxidation proceeds and the concentration of ferric ions increases the reaction, described by Equation 1.3, becomes the dominant reaction and for every mole of pyrite oxidised, 16 moles of acid are produced. This may lead to the release of heavy metals (which are often present as impurities within the pyrite) into the surrounding environment [12]. Furthermore, the

acidification of waters may also lead to the leaching of heavy metals from otherwise stable minerals. As the acidity increases the capacity for more acid to be produced and for heavy metals to be leached also increases [13]. This can lead to increased bioaccumulation and biomagnification of heavy metals in local flora due to the increased concentrations of the heavy metals in waterways [14]. AMD has been described as *"the largest environmental problem facing the U.S. mining industry"* [15].

$$2FeS_{2(s)} + 7O_{2(g)} + 2H_2O_{(l)} \rightarrow 2Fe^{2+}_{(aq)} + 4SO^{2-}_{4(aq)} + 4H^{+}_{(aq)}$$

Equation 1.1 Initial oxidation of pyrite by oxygen.

$$4Fe^{2+}_{(aq)} + O_{2(g)} + 4H^{+}_{(aq)} \rightarrow 4Fe^{3+}_{(aq)} + 2H_2O_{(l)}$$

Equation 1.2 Oxidation of ferrous to ferric ions by oxygen.

$$FeS_{2(s)} + 14Fe^{3+}_{(aq)} + 8H_2O_{(l)} \rightarrow 15Fe^{2+}_{(aq)} + 2SO^{2-}_{4(aq)} + 16H^{+}_{(aq)}$$

Equation 1.3 Oxidation of pyrite by ferric ions.

$$Fe^{3+}_{(aq)} + 3H_2O_{(l)} \rightarrow Fe(OH)_{3(s)} + 3H^{+}_{(aq)}$$

Equation 1.4 Precipitation of iron hydroxide at pH>4.5.

A puzzling observation that has caused much discussion in pyrite literature is that pyrite specimens from different locations appear to oxidise at different rates. For example, museum specimens of pyrite of similar age and storage conditions have been noted to deteriorate at such markedly different rates that it is visibly noticeable, where one sample may be lustrous another may be crumbling apart [7]. Figure 1.1 and 1.2 show two different pyrite samples which have been stored at the South Australian Museum in the same conditions for approximately the same period of time and they show a visibly marked difference in reactivity.

Figure 1.1 Image of oxidised pyrite. *A museum sample of pyrite showing extensive oxidation [16].*

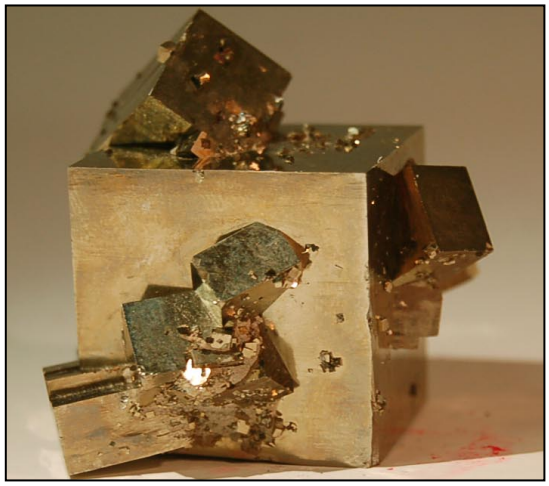

Figure 1.2 Image of unoxidised pyrite. *A museum sample of pyrite showing negligible oxidation [17].*

Pyrite has also shown variable behaviour during flotation separation from other base metal sulfides [3] making the flotation processes less efficient and therefore, making the reclamation of the ore of interest less economically viable.

1.2 Pyrite mineralogy

Pyrite belongs to a group of iron sulfide minerals, of which a selection of the most abundant are shown in Table 1.1 (more extensive lists of iron sulfide mineral data can be found at various sources, most notably a free to access online resource of the Handbook of Mineralogy [18]).

The structure of pyrite was one of the very first crystals to be analysed by W.L. Bragg using X-ray analysis [19]. The crystal structure of pyrite, presented in Figure 1.3, is most easily described as analogous to the NaCl crystal structure with Fe occupying the Na positions and the middle of the disulfide bond occupying the Cl position [3, 5, 13]. In more detail the ferrous ions (Fe^{2+}, low-spin d^6, t_{2g}^6) have a face centred cubic arrangement and the disulfide ions (S_2^{2-}) are situated at the centre of the cube, and also midway along each of the unit cell sides. Pyrite is known to have a unit cell length of a_0=5.4179(11)Å [18].

Table 1.1 Common iron sulfide minerals.
A summary of some common iron sulfide minerals [5, 18, 20].

Sulfide minerals	Stoichiometry	Crystal structure	Stability	Abundance
Pyrite	FeS_2	Cubic	Stable	The most abundant sulfide mineral
Marcasite	FeS_2	Orthorhombic	Metastable	A common mineral in hydrothermal and sedimentary systems, formed in low temperature, highly acidic environments
Greigite	Fe_3S_4	Cubic	Metastable	Widespread, associated with freshwater systems
Pyrrhotite (monoclinic)	Fe_7S_8	Monoclinic	Metastable	Sulfur deficient pyrrhotite where the formula tends toward FeS, the structure is hexagonal. When it is high in sulfur, the structure is monoclinic
Pyrrhotite (hexagonal)	$Fe_{1-x}S$ (x<0.2)	Hexagonal	Stable	Very abundant but rare in marine systems
Troilite	FeS	Hexagonal	Stable	Rare, mainly found in meteorites
Mackinawite	$(Fe,Ni)_{1+x}S$ (x<0.12)	Tetragonal	Metastable	Widespread in low-temp aqueous environments
Smythite	Fe_3S_4	Hexagonal	Metastable	Low temperature oxidation product of monoclinic, magnetic pyrrhotite and as inclusions in calcite crystals in quartz geodes

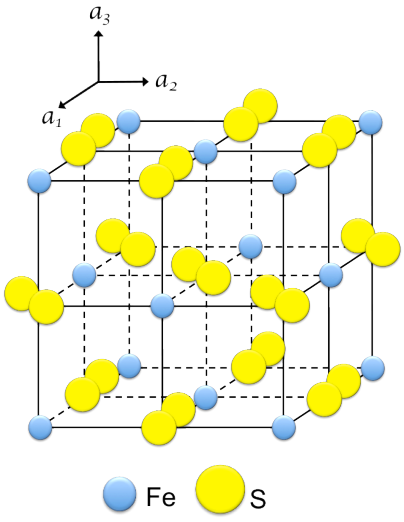

Figure 1.3 Pyrite unit cell structure.
Diagram showing the unit cell structure of pyrite reproduced from [21].

Pyrite occurs in two main crystal forms: euhedral and framboidal. Euhedral refers to pyrite with a well developed crystal form. The most common crystal forms for pyrite are the cube {100} (Figure 1.4) and the pentagonal dodecahedron {012} (or pyritohedron, Figure 1.5) [20].

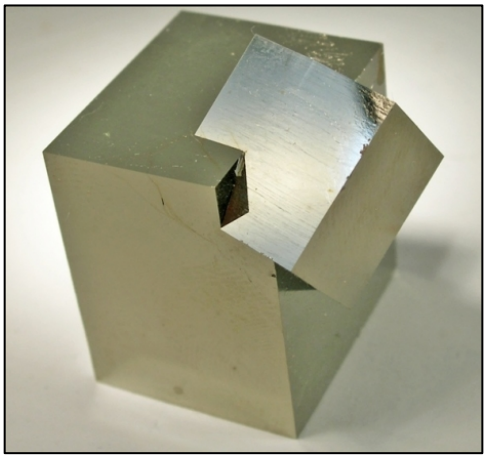

Figure 1.4 Image of cubic pyrite. *Example of cubic euhedral pyrite from La Roja, Spain [22].*

Figure 1.5 Image of pyritohedral pyrite. *Example of pyritohedral euhedral pyrite from Magma Mine, Arizona [23].*

Framboidal (meaning raspberry like) pyrite consists of poorly formed grains of pyrite between 2μm-5μm in diameter which tend to agglomerate into balls of between 10μm-30μm diameter [20]. Framboidal pyrite is thought to be formed predominantly in organic rich sediments which have been subject to marine waters [24]. A study by Butler [25] and review by Ohfuji [26] concluded that the size and crystal form of pyrite formation products is the result of the rate of crystal growth versus rate of nucleation, where nucleation is controlled by the saturation of the solution with respect to pyrite. The reduction potential, pH and temperature of the solution control the solution chemistry, with supersaturation occurring at circumneutral pH values in slight oxic conditions (Eh>-250mV). Framboids form when nucleation is favourable (generally in supersaturated solutions with respect to pyrite) but growth may be limited by substrate availability. Euhedral pyrite is then thought to form in solutions with a lower reduction potential (Eh≈-400mV) where the solution is less saturated with respect to pyrite.

1.3 Semiconductivity and trace elements

Pyrite is a semiconductor with a band gap of 0.95eV and has been shown to exhibit both p-type and n-type semiconductor behaviour [27], and its conductivity has been shown by Pridmore and Shuey [28] and Doyle and Mirza [29] to vary in the range of 0.014-562Ω^{-1}.cm^{-1} (average 52.3Ω^{-1}.cm^{-1}). This variable behaviour has been attributed to two main factors.

The first is variations in the stoichiometry of the mineral; pyrites that are slightly S rich (S:Fe ratio >2) have been found to be p-type, as excess S acts as an electron acceptor. Conversely Fe rich pyrites (S:Fe ratio <2) have been found to be n-type [28]. This theory is questioned by Doyle and Mirza [29] who measured 12 pyrite samples and did not find any significant deviation from ideal stoichiometric ratio of 2 (range found to be 1.983-2.015 approximately 0.5% deviation from the ideal) and the work by Smith [30] also showed only minor deviation from the ideal ratio.

The second factor reported to affect the semiconductor properties of pyrite is impurities present in the mineral. Elements frequently found as impurities in significant quantities (up to a few %w/w) in pyrite include: Ag, As, Au, Co, Cu, Ni, Sb and Sn. Other elements found in smaller quantities include Bi, Cd, Hg, Mo, Pb, Pd, Ru, Se, Te, Tl and Zn [3]. The p-type often contains significant quantities of As and Se which act as an electron acceptors, and n-types often contain metals such as Co and Ni which act as electron donors [31, 32].

Trace element impurities can be incorporated into pyrite in two ways; as lattice substitutions or as mineral inclusions. According to a review by Abraitis *et al*. [3], lattice impurities can present as either stoichiometric or non-stoichiometric: stoichiometric substitutions occur when ions are substituted for other ions of similar charge and radius, for example substituting an Fe^{2+} for a Co^{2+}; non-stoichiometric substitutions occur when ions of differing charge and/or size replace the archetypal ion. These non-stoichiometric substitutions are likely to have a much greater effect on the electronic structure of the mineral, which in turn are thought to have a greater effect on the reactivity of the specimen. Differing electron transport processes may occur depending on the semiconductor properties of the mineral, and the electrochemical oxidation processes discussed in section 1.4.1 may also differ with trace element impurities. In this context arsenic anions are expected to be an important substituent in the disulfide anion (S_2^{2-}).

The other way in which trace elements may be present in pyrite is through inclusions of other minerals or native elements. These inclusions can be relatively large (on the scale of 10s of microns) and can contribute a

significant percentage of the mineral sample or can be very small as nano-particles [33]. These inclusions are not expected to influence the chemistry of pyrite to as great an extent as lattice substitutions. They do, however, pose a separate challenge; gold bearing inclusions in minerals such as pyrite, which are not visible using standard optical techniques are termed “invisible gold”. Invisible gold is commonly present in pyrite and some other minerals in concentrations which range from 69ppb to 2,298ppm [34]. This may not seem significant, but given the sheer amount of pyrite that is processed around the world there are potentially tonnes of gold that could be recovered from waste material. The problem is to make the extraction of this invisible gold economic. By studying the causes of the variation in the reactivity of pyrite it may be possible to find a means of extracting this gold using an efficient method that will result in a net monetary gain.

1.4 Previous studies

1.4.1 Reaction mechanism

There have been many studies which aim to describe the kinetics of pyrite oxidation using mechanisms and rate equations. The studies have been performed in a variety of conditions, using various oxidising agents including dissolved oxygen [35-39], ferric ions [7, 40], and hydrogen peroxide [2, 4, 41-43], and several studies have investigated the influence of two or more of the listed oxidants either concurrently or separately [31, 44-46]. The effects of various other factors thought to influence reaction kinetics have also been investigated including pH, temperature, illumination and presence of metal ions [27, 47-49].

Given the semiconducting nature of pyrite, it has been proposed that an electrochemical method of oxidation can be applied to pyrite. Rimstidt and Vaughan [31] published possibly the most highly cited paper on the mechanism of pyrite oxidiation (over 140 citations at the time of writing), proposing a step by step electrochemical mechanism of pyrite oxidation. They separated the process into three broad stages; the cathodic reaction, electron transport (between the anodic and cathodic sites) and the anodic reaction. Mechanisms 1.1, 1.2, 1.3 and 1.4 illustrate the process presented in the Rimstidt and Vaughan paper (note: between each of the following steps

an electron is transferred from an anodic site to reduce the ferric ion back to ferrous). They found that as the rate of the reaction is positively dependent on the concentration of the oxidising agent, the electron transfer to the oxidant from iron sites is the rate limiting step, supporting previously published work by Smith and Shumate [50].

In the initial step of the mechanism, the oxidant (in this case O_2) adsorbs to a ferrous ion site at the pyrite surface and an electron is transferred to it (Mechanism 1.1), resulting in a superoxide anion at the pyrite surface.

$$py - Fe^{2+} \cdots O_2 \rightarrow py - Fe^{3+} \cdots O_2^-$$
$$\begin{pmatrix} py - indicates\ the\ pyrite\ surface \\ \cdots indicates\ adsorbtion \end{pmatrix}$$

Mechanism 1.1 Production of superoxide anion.

In acidic conditions, the resulting ferric ion gains an electron from an anodic site within the mineral and the superoxide anion reacts with a proton to form hydroperoxyl species on the surface. Electron transfer from the ferrous ion to the hydroperoxyl species follows (Mechanism 1.2):

$$py - Fe^{2+} \cdots O_2H \rightarrow py - Fe^{3+} \cdots O_2H^-$$

Mechanism 1.2 Production of hydroperoxyl anion.

In the third step of the mechanism, a further electron is transferred to the iron from an anodic site and a second hydrogen ion reacts with the hydroperoxyl anion. This results in a ferrous ion and H_2O_2 on the surface. A subsequent electron is transferred to the peroxide from the ferrous ion to create a hydroxide radical and anion (Mechanism 1.3). Borda *et al.* [51] presents data that confirms the production of hydrogen peroxide and hydroxyl radicals from the reaction of pyrite with water.

$$py - Fe^{2+} \cdots H_2O_2 \rightarrow py - Fe^{3+} \cdots OH\bullet + OH^-$$

Mechanism 1.3 Dissociation of hydroxide anion.

Again, an electron is transferred from an anodic site to reduce the iron. The electron is then transferred from the ferrous ion to convert the radical to an anion which dissociates into solution (Mechanism 1.4).

$$py - Fe^{2+} \cdots OH\bullet \rightarrow py - Fe^{3+} + OH^-$$

Mechanism 1.4 Dissociation of a second hydroxide anion.

Finally, an electron moves from the anodic site to leave the iron site as a ferrous ion, meaning that the iron site remains unchanged despite having transferred four electrons through it.

According to this mechanism, the anodic sites are where the reaction products are formed and are released into solution. This process involves the removal of seven electrons from the disulfide to form sulfate. Removal of electrons from cathodic sites (Mechanisms 1.1, 1.2, 1.3 and 1.4,) causes the sulfur atoms to become increasingly electropositive (Mechanism 1.5).

$$py - S - S \rightarrow py - S - S^+ + e^-$$

Mechanism 1.5 Formation of an electropositive sulfur site.

Water is able to nucleophilically attack the electropositive sulfur releasing a proton into solution, balancing the loss of an electron to the oxidant at the cathodic site.

$$py - S - S^+ + H_2O \rightarrow py - S - S - OH + H^+$$

Mechanism 1.6 Nucleophilic attack of the sulfur site by water.

As a further electron is removed at the cathode, a second proton is removed to balance it from the anode.

$$py - S - S - OH \rightarrow py - S - SO + e^- + H^+$$

Mechanism 1.7 Dissociation of a proton into solution.

The process is repeated twice more to remove a total of six electrons and six protons (Mechanism 1.8 and 1.9).

$$py - S - SO \rightarrow py - S - SO_2 + 2e^- + H^+$$

Mechanism 1.8 Nucleophilic attack by a second water molecule.

$$py - S - SO_2 \rightarrow py - S - SO_3 + 2e^- + H^+$$

Mechanism 1.9 Oxidation by nucleophilic attack by a third water molecule.

At high pH, the terminal S-SO_3 is ionised making the S-S bond stronger than the Fe-S bond and the moiety is released into solution as thiosulfate complexed with a cation (M) (Mechanism 1.10).

$$py - S - S - O_3 \rightarrow py + MS_2O_3$$

Mechanism 1.10 Dissociation of thiosulfate at high pH.

At low pH the sulfur group retains a proton S-SO_3H which increases the proportion of electrons across the S-S bond making them more easily stolen by the cathode which leaves the terminal sulfur very electropositive, allowing a fourth nucleophilic attack by water (Mechanism 1.11).

$$py - S - SO_3 \rightarrow py - S + HSO_4^- + e^- + H^+$$

Mechanism 1.11 Dissociation of sulfate at low pH.

The stepwise removal of electrons from a sulfur group involves the formation of several intermediate sulfur compounds which have been analysed in several studies [2, 45], however, they have not been found in any great proportions compared to sulfate, and thus they suggested that Mechanism 1.11 is the dominant mechanism. In total, per mole of sulfate produced seven electrons are removed from the mineral, four water molecules are consumed and eight hydrogen ions are released into the solution.

Rimstidt and Vaughan [31] suggest that for the studies performed which compare the reactivity of pyrite from different locations any reported variation in reactivity can be explained by the variation in band gap (the energy difference between the top of the valence band and the bottom of the conduction band) caused by impurities in the minerals. A variation in band gap energy would affect the proportion of electrons in the valence band available for transfer to the oxidant. Manaka [38] provides evidence for this hypothesis, showing that as the total concentration of impurities decreases, the ratio of ferrous ions produced (Equation 1.2) compared to sulfate ions produced (Equation 1.1) increases, suggesting that the rate of oxidation of pyrite increases with increasing concentration of impurities. Manaka [38] also suggests that differences in impurity concentrations can change the overall reaction stoichiometry, leading to slightly different reaction orders with respect to dissolved oxygen. Where impurity concentrations were greater

than 1000ppm the reaction order with respect to dissolved oxygen was close to 1, below this value it was closer to 0.5. This held true for rate laws they compiled from several other authors. Doyle and Mirza [29] also presented evidence of differences in rate order with regard to dissolved oxygen with different impurity levels; their electrochemical tests showed that generally samples with low resistivity and high charge carrier concentration had a higher charge density (i.e. electric current per unit area of cross section). This property would make it “easier” for electrons to move from the cathodic to anodic sites during pyrite reaction. These results were mirrored by their chemical dissolution tests which showed that, in general, the samples with low resistivity and a higher density of charge carriers were more reactive in terms of the overall amount pyrite reacted.

Further evidence for an electrochemical mechanism of pyrite oxidation is provided in work by Schoonen *et al.* [49] who show tentative evidence toward the increase in reaction rate when the pyrite is under illumination compared to when it is in the dark. This could be explained by an increase in ease of electron transport due to more available charge carriers as electrons are promoted to the valence band across the band gap by the incident photons. However, it is also possible that the increase in rate was due to a heating effect from the illumination source.

Borda *et al.* [51] found using X-ray photoelectron spectroscopy (XPS) that after exposing a clean pyrite surface to water in anoxic conditions that ferric sites are converted to ferrous sites, though this may not be due directly to reduction of ferric ions by water but due to nucleophilic attack by water at an electron deficient sulfur at an anodic site.

Furthermore Holmes and Crundwell [44] investigate the electrochemical mechanism of pyrite dissolution in the presence of ferric ions and dissolved oxygen. They used half reactions analogous to the mechanisms proposed by Rimstidt and Vaughan [31] with the anodic reaction for the oxidation of pyrite (Equation 1.5) and the cathodic reaction for the reduction of the oxidants (Equation 1.7).

$$FeS_2 + 8H_2O \rightarrow Fe^{2+} + 2SO_4^{2-} + 16H^+ + 14e^-$$

Equation 1.5 Anodic reaction of sulfur during pyrite oxidation.

$$Fe^{3+} + e^- \rightarrow Fe^{2+}$$

Equation 1.6 Cathodic reduction of ferric ion during pyrite oxidation.

$$O_2 + 4H^+ + 4e^- \rightarrow 2H_2O$$

Equation 1.7 Cathodic reduction of dissolved oxygen during pyrite oxidation.

The rates of Equation 1.5, 1.6 and 1.7 are dependent on the potential across the mineral-solution interface: they occur over the whole pyrite surface that is available for reaction simultaneously and satisfy the condition that the net electron production is zero. The electrochemical potential at which this occurs is called the mixed potential. Furthermore, reaction kinetics can be studied by measuring the mixed potential at different ion concentrations.

As far as the rate of pyrite oxidation is concerned the surface area of the sample is known to be an important factor. It has been suggested that the great difference in reactivity observed in museum samples is mostly due to the difference in the surface areas of pyrite samples [50]. In nature oxidation can be accelerated by the formation of the less dense melanterite ($(FeSO_4.7H_2O)$ a product of pyrite oxidation) which can crystallise in fractures within the pyrite and force the mineral to fracture further, thereby increasing the mineral's surface area; a problem known as "pyrite disease" [31].

1.4.2 Reaction with hydrogen peroxide

An oxidant that is sometimes used in laboratories to oxidise pyrite is hydrogen peroxide. It is used because the reaction products are few, only water, oxygen, sulfate and ferric ions. Hydrogen peroxide also oxidises pyrite much more rapidly than oxygen or ferric ions. Consequently, it has been considered a proxy for the natural oxidation of pyrite [2]. The overall reaction is known to have the following stoichiometry [4, 43]:

$$2FeS_2 + 15H_2O_2 \rightarrow 2Fe^{3+} + 4SO_4^{2-} + 2H^+ + 14H_2O$$

Equation 1.8 Pyrite oxidation by hydrogen peroxide.

Despite the advantages of using hydrogen peroxide as an oxidant there are some experimental complications. The rate of oxidation is complicated by the fact that hydrogen peroxide is catalytically decomposed by iron ions (known as Fenton's reactions) which are produced as a reaction product, therefore, as the reaction proceeds the oxidant is more rapidly decomposed. However, increasing acidity is known to stabilise hydrogen peroxide from decomposition and hydronium ions are also produced as reaction products, so paradoxically as the reaction proceeds the oxidant is also more stabilised.

A simple but effective way to negate the effects of oxidant concentration is to make the initial oxidant concentration large enough so that the reduction in oxidant concentration over the course of the reaction is negligible, thereby making the reaction kinetics pseudo zero order. This means that the rate of reaction is then equal to the rate constant.

Druschel and Borda [52] note that reaction pathways are often complex involving forward, backward, inhibiting, catalysing and competing steps. This causes the overall reaction to depend on certain variables in very complex relationships. Thus, even slight differences in reaction conditions may cause the reaction to proceed very differently overall. This is important to remember because when comparing studies that investigate the rate of pyrite oxidation any differences that may be found could be due to the differences in reaction conditions, however slight they may be. Thus, the only way to truly compare the reactivities of different pyrite samples *en masse* is to react them all under the same conditions, for example, Liu *et al.* [53] report a difference in initial dissolution stoichiometry simply by using a different sieving method.

1.4.3 Studies examining the variation in rate of pyrite oxidation

There have been relatively few studies comparing the variation in reactivity between pyrite samples (natural and synthetic) [7, 38, 39, 50, 53-56] compared to the immense body of literature available on pyrite reactivity in general. The results from these studies have been mixed, which is not surprising due to the myriad of reaction variables which are controlled or varied differently by each researcher. Different oxidants are used, different reaction products are measured, and variables such as temperature, pH and particle size are inconsistent between studies. The other point to be made

about these studies is the relatively few different mineral samples tested in each case, and considering that pyrite is known to be the most abundant sulfide mineral these small sample sets (eight or less) will not be representative of the variation of pyrite samples across the globe. A number of these studies are evaluated below.

Wiersma and Rimstidt [7] compared the rate of oxidation of seven pyrite and three marcasite samples (3 early diagenetic pyrites, 4 higher temperature, hydrothermal or metamorphic and 3 hydrothermal marcasites) by ferric ion at pH 2. These conditions were chosen to mimic the conditions found in acid mine drainage and also to prevent the precipitation of ferric ions as $Fe(OH)_{3(s)}$ which occurs at pH>3.5. Given that the reaction involves the ferrous-ferric redox couple they chose to monitor the change in redox potential of the reaction solution. They measured the reaction progress over a 250 minute reaction period. Assuming the stoichiometry of Equation 1.3, for every mole of pyrite oxidized, 14 moles of ferric ions is reduced to ferrous ions. They found that the rate law which best fitted their experimental data was one that corrected for the ratio of the surface area of the sample to the mass of reaction solution, and was first order with respect to ferric ions (Equation 1.9).

$$\frac{-dm_{Fe^{3+}}}{dt} = k\left(\frac{A}{M}\right)m_{Fe^{3+}}$$

Equation 1.9 Oxidation rate law.
Rate law for the oxidation of pyrite by ferric ions, deduced by Wiersma and Rimstidt [7].

Where k is the rate constant, $m_{Fe}{}^{3+}$ is the concentration of free iron in moles and A/M is the ratio of the interfacial area between the solid and the aqueous phase (A) and the mass of water in the system (M). They found that the early diagenetic pyrites reacted on average three times faster than the high temperature pyrite and marcasite samples. However, after corrections for the surface-area to mass-of-solution ratio were made the higher temperature pyrite was shown to be 2.72 times more reactive than the early diagenetic pyrite. They concluded that while these different groups showed a difference in reactivity that difference was not significant enough to account for the observed difference in acid production from different mining sites.

In this study, Wiersma and Rimstidt [7] described a dry sieving procedure after the crushing of their run material but fail to mention any washing procedure to remove the nano scale particles which are known to adhere to the larger surfaces. This would lead to an anomalously high initial rate of reaction, as is evident from their electromotive force (EMF) versus time plot which decreases rapidly in the first 50 minutes. It would also mean that their correction for surface area in their rate equation would only be valid for the beginning of the reaction as the surface area would rapidly decrease as the reaction progressed.

Garrels and Thompson [54] studied the reactivity of three pyrite samples from different locations; from their description all were euhedral. Spectroscopic analysis of the samples was undertaken for trace impurities and no elements were reported although limits of detection were not given. They measured the time taken for the reduction of half of the ferric ion oxidant potentiometrically assuming the stoichiometry of Equation 1.3. The time taken for 50% of the ferric ions to be reduced was measured from the reduction potential of the solution. This time was taken as an indicator of reactivity; the three samples gave times of 200, 500 and 1600 minutes, implying an overall 8-fold difference in reaction time. On the basis of this they conclude that the three samples react at markedly different rates. These researchers also studied the effect of adding a small concentration (μM) of; V, Co, Cu, Ni, Ce and Mn salts to the reaction solution, but concluded that there was no effect on the observed rate.

Nicholson *et al.* [39] measured the oxidation of pyrite by water and oxygen in a carbonate buffered system at *circum* neutral pH from six different locales. They measured production of sulfate as a reaction progress variable as iron would precipitate as $Fe(OH)_3$ in the near neutral conditions. They assumed for every mole of pyrite reacted that two moles of sulfate would be formed, they verify that sulfate is by far the major sulfur product produced by analysing their reaction effluent with and without addition of hydrogen peroxide. Results showed that of the six samples, their rates could be grouped into two statistically different groups; four had very similar rates which averaged 6.56×10^{-8} moles pyrite.h^{-1}.g^{-1} while the other two had an average rate of 8.03×10^{-8} moles pyrite.h^{-1}.g^{-1}. Nicholson *et al*. also performed

trace element analysis on their samples and observed that the most reactive sample had the greatest concentrations of Al (442ppm), Cu (1180ppm), Mg (878ppm), Mn (24ppm), and Zn (4040ppm), the least reactive sample also showed comparatively high levels of Al (424ppm), Ba (8ppm) and Cu (576ppm) but also showed the highest levels of Co (613ppm), Ni (275ppm), Pb (965ppm), Si (173ppm), Sr (6ppm), Th (120ppm), Ti (82ppm) and Zr (19ppm). These results are interesting as it appears that samples with increased trace element composition sit on the polar opposite ends of the reactivitites measured, however, the relatively few results presented make it difficult to draw any significant conclusions from this work.

Manaka [38] oxidised five pyrite samples from different locations using dissolved oxygen in solutions at pH 4 which would allow the precipitation of ferric hydroxide. They calculated a different rate law for each sample by assuming that the overall reaction was a competition for oxidant between Equation 1.1 and 1.10 (where Equation 1.10 is a combination of Equation 1.1, 1.2 and 1.4).

$$4FeS_{2(s)} + 15O_{2(g)} + 14H_2O_{(l)} \rightarrow 4Fe(OH)_{3(s)} + 8SO^{2-}_{4(aq)} + 16H^{+}_{(aq)}$$

Equation 1.10 Pyrite oxidation at pH>4.
Oxidation of pyrite by dissolved oxygen at pH>4 resulting in the precipitation of ferric hydroxide.

This resulted in the following reaction:

$$FeS_{2(s)} + aO_{2(g)} + bH_2O_{(l)} \rightarrow xFe^{2+} + yFe(OH)_{3(s)} + 2SO^{2-}_{4(aq)} + zH^{+}_{(aq)}$$
$$x + y = 1$$
$$z = 2b - 3y$$

Equation 1.11 Pyrite oxidation at pH>4 overall equation.

Manaka [38] calculated the ratio of $[Fe^{2+}]/[SO_4^{2-}]$ to gauge the contribution of each reaction. A ratio of 0.5 indicates that Equation 1.1 dominated where a ratio that tends towards 0 meant that Equation 1.10 dominated. They ignore the effect of pH on the reaction rate as its variation during the reaction was negligible. They found that both the reaction order with respect to oxygen and rate constant varied between pyrite samples. As the units for the rate constant varied with the reaction order, it was not possible to use the rate constant as a measure of sample reactivity. Therefore, they used the slope of

the graph of ferrous ion concentration versus sulfate concentration to compare samples. A steeper slope indicates that the oxidation of the pyrite sample (Equation 1.1) is occurring more quickly than the oxidation of ferrous to ferric ions (Equation 1.2), The slope was shown to vary in the order of 0.21 to 0.47. Manaka also measured the concentration of a number of trace element impuirties (As, Bi, Co, Cu, Mn, Ni, Pb, Sb and Zn) in the samples using inductively coupled plasma atomic emission spectroscopy (ICP-AES) (Co and Ni) and inductively coupled mass spectrometry (ICP-MS) (the remainder) and compared them to the slope, they found that as the total concentration of impurities increased (263–3596ppm) the slope decreased, indicating an increase in rate of ferrous ion oxidation with decreasing total impurities. They found the same relationship when comparing slope to As concentration, indicating that as As concentration increases (11–77ppm) the rate of oxidation of ferrous to ferric ions will increase. The implication of this could be that impurities such as As increase the rate at which Equation 1.2 occurs, effectively increasing the oxidant concentration for Equation 1.3. While this is an interesting theory it is something which needs to be investigated in a more direct fashion. While Manaka stated that the aim of his work was to study pyrite oxidation rates it seems as though they actually studied reaction mechanisms, applied to different samples.

Doyle and Mirza [29] presented an electrochemical study of twelve pyrite samples. For each sample, they measured the Fe:S ratio using X-ray probe microanalysis, trace elements (Cu, Ni, Pb, Zn and As) by X-ray fluorescence (XRF) and Co by atomic absorption spectroscopy (AAS). Electrical properties (resistivities, charge carrier density and charge carrier mobilities) were determined from Hall effect measurements. Electrochemical studies were performed using a three compartment electrical cell. Chemical dissolution experiments were also performed using the method published by Sobek and Schuller [58] modified to prevent the thermal decomposition of hydrogen peroxide by using an ice bath to control temperature. Their results showed some evidence of a positive linear correlation between the percent of pyrite dissolved and the log of charge carrier concentration. They also note negative relationships between the log of resistivity and rest potential, this provides evidence toward the hypothesis that trace element impurities affect

the reactivity of different pyrite samples. However no conclusive results can be determined from their graph containing only four points but with further investigation a stronger relationship may be established.

Liu *et al.* [53] investigated the oxidation of pyrite in aerobic conditions at pH values 3 and 6. They compared the dissolution of eight pyrite samples, five sedimentary and three hydrothermal by sampling the reaction solution over the 24h. reaction period and measuring total sulfur using ICP-AES. They found at pH 3 that sedimentary pyrites associated with coals reacted the fastest (average $4.71x10^{-7}mol.L^{-1}.min^{-1}$), followed by other sedimentary pyrites (average $5.74x10^{-8}mol.L^{-1}.min^{-1}$) then hydrothermal pyrites (average $3.97x10^{-8}mol.L^{-1}.min^{-1}$). Similar results were obtained at pH 6, sedimentary pyrites associated with coal were the most reactive (average 7.71 $x10^{-7}mol.L^{-1}.min^{-1}$) while sedimentary and hydrothermal gave similar results (average ($5.37x10^{-8}mol.L^{-1}.min^{-1}$ and $5.78x10^{-8}mol.L^{-1}.min^{-1}$ respectively). They attempt to correlate the difference in reactivity to the specific surface area of the samples, they found at pH 3 two sedimentary pyrites that had very similar rates of reaction differed in surface area by a factor of two, and at pH 6 the sedimentary pyrite with the smallest surface area gave the largest reaction rate, at least twice as large as the next largest rate, suggesting, that there is more to the difference in pyrite reactivity than simply surface area. Trace element analysis was performed by ICP-AES for the elements Co, Tl, Ba, Bi, Hg, Rb and Te. The sedimentary samples generally had greater concentrations of Tl (4-52ppm compared to 0.01–0.03ppm), Ba (2.61–23.4ppm compared to 0.16–0.37ppm), Hg (0.05–10.3ppm compared to 0.04–0.13) and Rb (0.45–3.80ppm compared to 0.15–0.29) while the hydrothermal samples had greater concentrations of Co (45.9–6004ppm compared to 0.34–12.4ppm), Bi (15.7–94.6ppm compared to <0.11) and Te (44.2–101ppm compared to <0.04ppm). Based on observations made by Lenher *et al*. [27] they calculated the ratios of known hole donors to electron donors ([As]+[Sb])/([Co]+[Ni]) they observed that the samples with ratios greater than 1 (i.e potentially p-type semiconductors) displayed greater dissolution rates than those with ratios less than 1 (potential n-type).

Smith and Shumate [50] compare the reactivity one of “museum grade” (most likely euhedral hydrothermal) and three “sulfur ball” pyrites often found

in coal fields (sedimentary). They measure the surface area of the crushed and sieved (60-150 mesh) museum grade sample to be 0.12±0.01$m^2.g^{-1}$ and the sulfur ball samples to be 1.12±0.02 $m^2.g^{-1}$, a 10 fold difference. The rate of oxidation of pyrite of the samples by dissolved oxygen range from 1.0-3.5$\mu M.h^{-1}.g^{-1}$ for the sulfur ball samples while the single museum grade sample had a reactivity of 0.03$\mu M.h^{-1}.g^{-1}$, the difference being a factor of between 33–117. When oxidised in the presence of ferric ion a similar trend was observed. The rate of reaction for the museum grade sample and the most reactive sulfur ball sample was 5.2 and 14$\mu M.h^{-1}.g^{-1}$ respectively, an approximate 3 fold difference. They conclude from both their oxygen and ferric ion oxidant experiments that the rate of pyrite oxidation depends on the amount of oxidant adsorbed to the pyrite surface compared to competing adsorbants (i.e. for ferric ion as the oxidant the rate depends on the relative amounts of ferric and ferrous ion) and that the difference in reactivity between samples was due to their difference in surface area. They did not examine the influence of trace element impurities on their results.

Chirita [59] studied the oxidation of 6 Romanian pyrite samples by potassium dichromate in perchloric acid. The reaction was monitored by periodic analysis of solubilised Fe by AAS. By varying temperature, oxidant concentration, pH and particle size of the reactions they form a rate expression with 0.51 order dependence on surface area, 0.64 order dependence on oxidant concentration and 0.22 order dependence on H^+ concentration. Chirita also measures the concentration of As (0.10-0.17%w/w), Co (0.01-0.04%w/w), Cu (0.00-0.02%w/w), Ni (0.00-0.04%w/w) and Zn (0.00-0.02%w/w) in the samples by electron probe. No correlation between trace element composition of the samples and their reactivity is found. However, because of the lack of information supplied about the origins of the samples and the relatively similar trace element concentrations it may be that the samples are all from very similar locations and are therefore, likely to react similarly.

Cruz *et al.* [56] analysed 5 pyrite samples, 1 from a skarn type deposit and 4 from volcanogenic massive sulfide deposits. Unlike other studies that generally use homogeneous pyrite, their samples were relatively impure and ranged in purity from 80.4–96.9% pyrite. The remaining percentage being

classified as chalcopyrite, galena, sphalerite, arsenopyrite or non-sulfide impurities. They analysed the rate of change in concentration of several reaction products (SO_4^{2-}, Fe, Zn, Pb and Cu) as well as measuring pH throughout the reaction. They also monitored the pyrite surface during reaction using voltammetry. One of the volcanogenic samples showed a much greater rate of Fe and SO_4^{2-} liberation than the other samples. This sample had the lowest level of sulfide impurities of all samples (<0.3ppm), the next most reactive sample also had low levels of sulfide impurities (<0.4ppm) while the most reactive sample had the highest level of sulfide impurities (15.02ppm). They present plots of the change in concentration of reaction products (Fe, SO_4^{2-}, Zn and Pb) with time, which all show an initial, rapid increase followed by a decrease and then plateau. The authors explain this trend as initial oxidation, followed by precipitation of metal oxides on the mineral surface which results in passivation of the surface, inhibiting further reaction. However, given their sample preparation procedure and the lack of any washing step after crushing to remove fine powder adhering to the mineral particles, it is more likely that the initial rapid increase in reaction product is due to the early oxidation of the fine mineral powder. Furthermore, evidence of the fine adhering powder appears in scanning electron microscope (SEM) pictures of their mineral samples taken before their leaching experiments. Once the powder has been reacted the remaining surface area available for reaction is greatly reduced, leading to the reduction in rate.

1.5 Trace analysis

As discussed in section 1.4, there is considerable data in the literature to imply that trace element concentrations in pyrite samples could play an important role in their observed variation in reactivity. It is therefore important to be able to quantify these trace elements in an accurate and meaningful way. The analysis of trace impurities in any mineral must be carefully considered, while the bulk analysis of samples by techniques such as neutron activation analysis (NAA) or solution ICP-MS provides a good overall impression of trace elemental concentrations, the presence of other minerals or large inclusions in the sample are indistinguishable from actual lattice substitutions. On the other hand surface techniques such as laser ablation

ICP-MS (LA-ICP-MS) and electron microprobe offer high spatial resolution, providing data on how trace elements are incorporated into the mineral matrix. These techniques also tend to be more sensitive, offering much lower limits of detection for many elements. The disadvantage of these techniques is that they only analyse a very small proportion of the sample, generally the amount of sample analysed is insignificant compared to the bulk, hindering the ability to be able to draw any statistically significant conclusions about the bulk mineral sample from the analyses. It is best to combine these techniques to gain a greater overall impression of the trace element impurities within the sample, their overall concentration using bulk techniques, and the way in which they are incorporated into the sample using surface analysis techniques.

1.6 Reaction monitoring

To be able to determine the reactivity of pyrite samples we must be able to measure the rate at which a sample is oxidised. The rate of a reaction is defined as the rate of change of a reactant or product with time, therefore, to determine a reaction rate the concentration of at least one reactant or product must be repeatedly determined at known times. For the oxidation of pyrite there are three options for species to be monitored; iron, sulfur and the oxidant. Monitoring of the oxidant can be a complicated process because it is often involved in more than one process. For example oxygen is used to oxidise sulfur to sulfate (as in Equation 1.1) and it is also used in the oxidation of Fe^{2+} to Fe^{3+} (Equation 1.2). Another example is hydrogen peroxide, that as well as acting as an oxidant, also undergoes decomposition catalysed by Fe ions. Factors such as these make reaction rate monitoring unnecessarily complicated. If reaction products are considered it is first obvious that the reaction conditions play an important role, particularly pH. At higher pH's (>4.5) the Fe is predominantly precipitated as $Fe(OH)_3$ (Equation 1.4) and sulfur is present as thiosulfate complexes (Mechanism 1.10). At lower pH's Fe remains in solution as Fe^{2+} and Fe^{3+} and sulfur is predominantly present as sulfate (Mechanism 1.11). Therefore, if a low pH of reaction was maintained the most straightforward method of determining reaction progress would be the determination of total Fe or sulfate concentration. During oxidation of pyrite sulfur may be present as different

surface species such as polysulfides and elemental sulphur, this complex speciation can make utilising sulfaate as a reaction variable inaccurate. While the analysis of anions in solution can be somewhat complex, the determination of cations and the chemistry of iron in solution is well understood and fairly straightforward. Fe is therefore the logical choice for a measure of reaction progress.

The determination of total iron in aqueous solution is commonly undertaken using a number of analytical methods, AAS [60], solution ICP-MS [61] and colorimetry [62]. While AAS and ICP-MS are sensitive, accurate and precise methods they involve the use of relatively expensive instrumentation. Colorimetry on the other hand provides comparable results with low cost ultratviolet – visible (UV-VIS) detectors. Colorimetry offers the flexibility of a number of colorimetric reagents, including 1,10-phenanthroline [62, 63], 5-sulfosalicylic acid (5-SSA) [64, 65], ferrozine [66, 67], and 2,2'-Bipyridyl [68].

The accuracy with which the rate may be determined depends on the precision of the measurement of the reactant/product concentration and the accuracy with which the time of the measurement can be made. Flow injection analysis (FIA) is a technique which is perfectly suited to the kinetic analysis of chemical reactions. FIA is an automated wet chemistry technique that in its most simple form involves the injection of a sample plug into a flowing reagent stream. The sample and reagent mix resulting in a chemical change which is measured by a detector and the magnitude of the change is proportional to the concentration of analyte in the sample. The simplicity of this technique is one of its largest benefits, because the concept is easy to understand it is easily adapted by researchers for their specific needs. FIA is readily adaptable to perform a vast array of on-line sample preparation and analysis procedures. The ease with which FIA can be computer controlled makes it perfect for kinetic analyses; reliable computer controlled timing coupled with high reproducibility means that reaction progress can be tracked reliably. Another advantage of FIA is that it uses smaller volumes of sample and reagents than traditional batch chemistry, making FIA more environmentally friendly and economically viable. FIA has been successfully applied to the analysis of dissolved iron in aqueous samples [66, 67, 69-71] and would be well suited to the monitoring of the oxidation of pyrite.

1.7 Research overview

As demonstrated in the literature review, examinations of pyrite oxidation rates have been varied in their approach and results. Conditions are inconsistent across the systems studied, for example some studies control surface area, whilst others do not. This research will undertake a systematic and controlled study to investigate the proposed natural variation in pyrite reactivity from different geographical locations. Despite the vast body of research into pyrite reactivity there is no evidence of a study which empirically measures the reactivity and other characteristic variables of a large number of geologically diverse pyrite specimens.

Initial investigation into the proposed variation of pyrite reactivity is presented in Chapter 2. Chapter 2 presents the development of a FIA based method for the determination of pyrite reactivity. Chapter 2 also presents the data for the measured reactivity of 40 mineral samples.

Due to the semiconducting properties of pyrite, the oxidation process it undergoes is widely regarded to be electrochemical. As such, the trace element impurities within the pyrite structure may affect its electrical properties and consequently influence reactivity. Chapter 3 presents the trace element concentration data from the analysis of thirty pyrite samples by NAA from two facilities. Each of these facilities performed the analysis using a different method of quantitation (relative comparator and k_0) Chapter 3 provides a statistical comparison of the data acquired by each facility as well as comparison to previously published data.

Chapter 4 then explores the data analysed in Chapter 3 and investigates the relationships between the concentrations of different trace elemental impurities. Chapter 4 also examines the relationships between trace element concentrations, reactivity and semiconducting properties of the samples.

The conditions of formation of mineral samples are often difficult to quantify and fall into broad categories but will undoubtedly contribute to the reactivity of the samples. Chapter 5 aims to correlate what is known about the formation conditions of a subset of the samples with data presented in previous chapters.

Chapter 2

Determination of pyrite oxidation rates

2.1 Introduction

The body of literature researching the reaction mechanisms and pathways of pyrite is vast, however, there are relatively few studies concerning the much debated variation in rate of reactivity of natural pyrites from different locations [7, 38, 39, 50, 53-55], and the reported results have been mixed. Each of these reports describe different kinetic tests whereby a sample of pyrite is placed in oxidising conditions and one or several of the reaction products (such as pH, sulfate or iron concentration) is monitored over time [15]. These tests take a very long time (ranging from days to years) and use very large sample sizes (from tens of grams to thousands of tonnes for larger field tests) [15]. Interpretation and analysis of these results is further complicated by the fact that each study has performed the experiments in a different manner. Inconsistencies in the sample preparation, oxidant used, reaction pH, and progress variable make it difficult to reach any significant conclusions using all available data.

In order to fully understand the natural variation in pyrite reactivity, experiments on a large number of samples from a wide variety of occurrences must be conducted in a controlled manner where the data collected can be accurately compared. This includes controlling reaction conditions, sample preparation, sample analysis and data handling. FIA is an ideal technique for this purpose.

FIA is an automated analytical technique which is performed using a flow injection manifold. A manifold is usually constructed from a combination of narrow-bore connected tubes, pumps, valves and an appropriate detector. A schematic for a simple flow injection manifold is displayed in Figure 2.1. In this instance an aliquot of sample (containing the analyte) of known volume is introduced into a moving carrier stream, which then converges with a second stream containing a reagent. As the sample diffuses in the reagent stream, a chemical, physical or electronic change occurs. This change is measured by a suitable detector and that signal is proportional to the concentration of analyte in the sample.

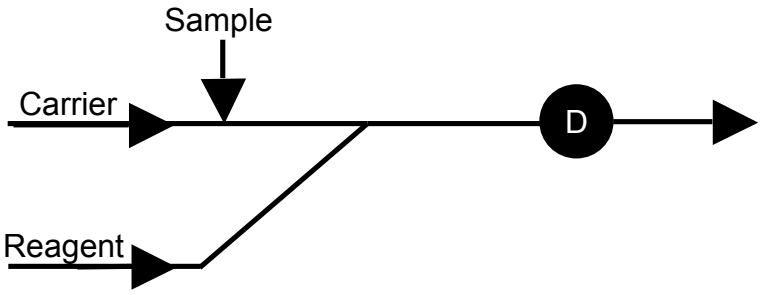

Figure 2.1 A simple flow injection manifold.
A sample, injected into the carrier stream, converges with a reagent stream, eliciting a change which is measured in the detector (D).

There are many advantages to flow injection techniques; they are easily adaptable and can be used to replace almost any analytical technique based on wet chemistry. They are easily automated as computer controllable pumps, valves and detectors are common. This automation means that sample throughput can be as high as 300 samples per hour [72]. Computer control also grants the technique highly reproducible timing of sample injection and detection [73], making FIA ideal for kinetic analyses where measurement of time is of the utmost importance. Moreover, software used to control an FIA manifold, such as LabVIEW^{TM}, is as adaptable as the manifolds it controls and it can be employed for the automated (but also flexible) collection and processing of analytical data [74].

For measuring the dissolution of pyrite in solution, the level of solubilised iron is a good measure of reaction progress. Sulfur, unlike iron, has complex speciation and is known to proceed through several intermediate species during the oxidation of pyrite [40]. Iron's aqueous chemistry is comparatively simple and well understood [75]. Determination of iron in solution can be achieved using a number of well-defined methods including colorimetry [76], atomic absorption spectroscopy [76], potentiometry [77] and ICP-MS [78], to name a few. In 2002, Karamanev and co-workers [64] reported the batch determination of ferric and total iron in mine drainage waters using the colorimetric reagent 5-SSA [64]. Under acidic conditions ferric ion reacts with 5-SSA on a 1:1 ratio to form a deep red complex, FeSSA; whilst under basic conditions (pH>8) the ferrous ion is rapidly oxidised to form the ferric ion, which subsequently complexes with 5-SSA in a 1:3 ratio to form $Fe(SSA)_3$

[79-82]. The result is an orange coloured solution with a maximum molar extinction coefficient of $5600M^{-1}.cm^{-1}$ at 420nm [79].

Importantly, the chemistry is insensitive to interference from oxidising agents and most other metal ions and is relatively unaffected by moderate changes in pH, which is in contrast to the more commonly used 1,10-phenanthroline [76].

This chapter presents an FIA method for the determination of total dissolved iron. The method is applied to the determination of pyrite oxidation rate constants for a series of pyrite samples obtained from diverse geographic locations.

2.2 Materials and methods

2.2.1 X-ray diffraction

To confirm the identity and purity of the samples, powder X-ray diffraction (XRD) patterns were collected for each of the samples. A Huber Guinier Imaging Plate G670 with Co-$K_{\alpha 1}$ radiation (λ=1.78892Å) generated at 35kV and 34mA was used for the analysis. Samples (1-2g) were ground in acetone and spread uniformly on a Mylar film, they were then mounted onto the oscillation unit and exposed for 15 minutes.

2.2.2 Instrumentation

All experiments were undertaken using an FIA manifold constructed in-house, as depicted in Figure 2.2. Control of the pump (Gilson Minipuls 3, John Morris Scientific, Melbourne, Australia), 6-port valve (Valco®, GlobalFIA, Fox Island, WA, USA) and UV-VIS detector (SCINCO S-3100 UV-VIS photo diode array spectrophotometer, DKSH Australia Ltd., Hallam, Australia) was achieved using a desktop computer (Dell Optiplex 755 Intel®Core™2 Duo 2.66GHz, 1.96GB RAM, Windows XP Professional SP3) running instrument control and data acquisition software developed in-house within the LabVIEW™ graphical programming package (LabVIEW™ 8.2.1 professional development system, National Instruments, Melbourne, Australia). The detector was equipped with a flow through cell (quartz windows, nominal volume 0.720mL, 10mm pathlength, Starna Pty. Ltd., NSW, Australia) and

the average absorbance across the region 423-427nm was used as the analytical signal.

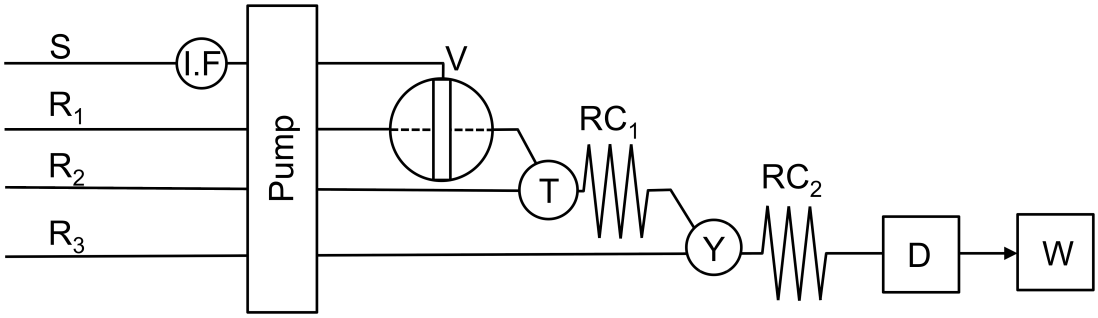

Figure 2.2 FIA manifold for the determination of total iron concentration.
Sample S, 18Ω water R1, 1.5%w/w 5-SSA R2, 2.5%v/v ammonia solution R3, 10µm in-line filter I.F, injection valve V, reaction coil 1 RC1, reaction coil 2 RC2, T-shaped mixer T, Y-shaped mixer Y, detector D, waste W.

Reagents and samples were propelled by the pump, fitted with 1.02mm internal diameter (i.d.) polyvinylchloride (PVC) tubing (DKSH Australia Ltd., Hallam, Australia) at an overall operating flow rate of 5.5mL.min^{-1} (~1.4mL.min^{-1} per line). All other tubing was 0.5mm i.d. polytetrafluoroethylene (PTFE) (GlobalFIA, Fox Island, WA, USA), with the exception of the tubing connecting junctions T and Y (Figure 2.2) and tubing from junction Y to waste, both of which were 0.8mm i.d.. All tubing was connected using standard fittings (GlobalFIA, Fox Island, WA, USA). The reaction coils had nominal volumes of 170µL (RC1 a coiled reactor) and 31µL (RC2 a serpentine reactor). An injection volume of 30µL was used for all experiments. During pyrite analysis a 10µm in-line filter (I.F) was fitted to the sample line S to prevent small particles from blocking the injection valve.

To prevent the precipitation of ferric ions as iron (III) hydroxide (which occurs when pH>3) the carrier (R1) was first merged with the 5-SSA solution (at the T junction on Figure 2.2) to form an Fe-SSA mixture. The resulting stream was merged with an ammonia stream (at junction Y on Figure 2.2) to raise the pH for determination of total iron. Ammonia was chosen in order to reduce the likelihood of precipitation of other metal hydroxides within the flow system.

2.2.3 Optimisation

Simplex optimisation of 5-SSA, ammonia and carrier stream concentration was performed using Multisimplex version 2.1.3 (Grabitech Solutions AB, 2001) with the objective of optimising peak height and minimising relative standard deviations. Maximum, minimum and optimum trialled concentrations are described in Table 2.1. All optimisation was undertaken using a 25mg.L^{-1} total iron solution.

Table 2.1 Concentrations investigated during Multisimplex optimisation.

	[5-SSA] %w/v	[Ammonia] %v/v	[H_2SO_4] (Carrier) (M)
Initial concentration	1.5	2.5	0.010
Minimum tested concentration	0.8	1.5	0.000
Maximum tested concentration	2.8	5.8	0.015
Optimum concentration	1.5	2.5	0.000

2.2.4 Reagents

All solutions were prepared in Barnstead ultrapure water (18MΩ), unless otherwise specified. 5-SSA (Sigma-Aldrich, NSW, Australia) and ammonia (Merck Pty. Ltd., Vic Australia) solutions were obtained.

Stock iron standards (1000mg.L^{-1} total iron) were prepared by dissolving 4.928g of ferrous sulfate heptahydrate (($FeSO_4.7H_2O$), Chem-Supply, South Australia) in 1L of 1M sulfuric acid. Stock solutions (1000mg.L^{-1}, SpectrosoL) of copper(II) and zinc(II) nitrates, and arsenic(V) oxide were obtained from BDH (England). Stock solutions (1000mg.L^{-1}) of nickel(II) nitrate and tin(IV) chloride were obtained from Australian Chemical Reagents (ACR) (Moorooka, Australia). The stock solution (1000mg.L^{-1}) of antimony(III) oxide was obtained from Sharlau (Barcelona, Spain). Stock solutions (1000mg.L^{-1}) of cobalt(II) were prepared by dissolving 0.4938g of cobalt(II)nitrate hexahydrate ($Co(NO_3)_2.6H_2O$), M&B Ltd., Dagenham, U.K.) in 100mL of water.

For oxidation of pyrite samples, 35%w/w hydrogen peroxide (Chem-Supply, South Australia) and 98%w/w sulfuric acid (Ajax Finechem, NSW, Australia) stock solutions were diluted to the required concentration in ultrapure water.

Inductviely coupled plasma (ICP) grade standard solutions of 10mg.L^{-1} iron and indium were obtained from Choice Analytical (NSW, Australia) and were diluted appropriately in 2%m/v sulfuric acid solution for ICP-MS analysis.

2.2.5 Pyrite sample preparation

Pyrite samples were obtained from the mineral collection of the South Australian Museum. The samples were examined for any visible impurities (e.g. quartz), and if present, these were removed by hand, resulting in a visibly homogeneous sample. For analysis of oxidation rate, samples were prepared immediately before analysis to negate any potential effects of storage. The sample preparation procedure is described in the following paragraph.

The sample was crushed in a purpose-built cylindrical tempered steel mortar and pestle. The crushed pyrite was then sieved through stainless steel sieves (Retsch, NSW, Australia) to isolate particles in the size range of: 53μm<x<106μm. This fraction was chosen to provide a sample with a large enough surface area to volume ratio to react rapidly and provide a great enough concentration of reaction product to be accurately measured. This fraction was subsequently mixed with approximately 10mL of acetone and ultrasonicated for 5 minutes to dislodge the fine mineral powder that is known to adhere to the grain surfaces during the crushing process. The supernatant was then discarded. This adhering powder has been identified to cause erroneously high reaction rates due to much larger surface areas available for reaction [57]. The process of adding acetone and ultrasonication was repeated until the supernatant was clear. The samples were subsequently rinsed in 18MΩ water and swirled in 1M nitric acid for 1 minute, re-rinsed in water and finally rinsed with acetone and dried on a hot plate (less than 50°C) to ensure all the acetone had been removed. This careful sample preparation procedure was undertaken to ensure that the pyrite fragments were of a similar size range and had clean surfaces, thereby minimising variation in surface area between samples. By removing surface area

variability between samples, the factor accounting for surface area can be excluded from the rate expression.

2.2.6 Sample analysis

Freshly prepared pyrite (0.10g) was accurately weighed into a clean 150mL polystyrene beaker, to which an acidic peroxide solution (50mL of a solution containing 1.0M sulfuric acid and 2.0M hydrogen peroxide) was added. Immediately at the time of addition, the FIA instrument was started. The pump circulated the pyrite reaction solution through the injection valve, returning the solution to the reaction vessel, and the software triggered the manifold to inject 30µL of the reaction solution every minute for 60 minutes. Sample reactivity was calculated by discarding the first 10 points (i.e. the first 10 minutes); this time was allowed for the reaction rate to stabilise. The peak height of the remaining fifty points were each averaged over the three replicates and fitted against a linear regression. A linear regression was found to be the most appropriate fit with R^2 usually greater than 0.9, indicating that the reaction is zero order with respect to production of iron (most likely due to the initial excess of oxidant). This was chosen because very poor regression statistics were observed for other common reaction orders. R^2 values were typically less than 0.8 for first order and less than 0.5 for second order kinetics. The slope of the regression line was taken as the rate constant (k).

2.2.7 Method validation

A sample of pyrite was reacted as described earlier, however, in addition to the instrument sampling the solution every minute, 30µL samples were also taken manually using an automatic pipette (Thermo Scientific, Australia) after reacting for 15, 30, 45 and 60 minutes. These were diluted to 5mL in 2% H_2SO_4 and analysed for ^{57}Fe using an Agilent 7500cx ICP-MS (Agilent, Victoria, Australia), utilising the octopole reaction system with helium gas (flow rate 5mL.min^{-1}) to correct for the effects of the interfering species ArOH. Instrumental operating conditions were optimised according to the instruments standard operating procedure for maximum sensitivity.

Solutions were measured against a 200μg.L^{-1} indium internal reference standard. A calibration curve for iron was generated from the signals of seven reference standards prepared with concentrations between 0 and 500μg.L^{-1}.

2.3 Results and discussion

2.3.1 Simplex optimisation of reagent concentrations

When one or more variables are dependent on each other, univariate optimisations may give misleading results; in this case it is more appropriate to employ a multivariate technique [83]. It was decided to perform a simplex optimisation in this study as the FeSSA complex formed is dependent on the final pH of the solution, with the optimal final pH being greater than 8 [84]. This is interdependent upon the concentration of the ammonia solution, the sample pH and acidity of the carrier stream. The initial reagent concentrations are described in Table 2.1 and the 5-SSA, ammonia and sulphuric acid were assigned step sizes of 1.5%w/w, 2.0%v/v and 0.01M respectively. After 13 trials only the ammonia concentration was shown to have a discernable effect on the signal. Peak height increased with increasing ammonia concentration up to 1.5%v/v where the signal plateaued, this corresponds to the reagent having an adequate ammonia concentration to elicit the desired change in pH causing full development of the basic 5-SSA colour. Beyond this concentration (1.5%v/v) the peak height and percentage relative standard deviation (%RSD) did not deviate significantly. In all cases the %RSD of peak height was below 1.8%.

2.3.2 Flow rate optimisation

As a result of the data acquisition requirements of our in-house software (slower flow rates resulted in a broader peak that could not be captured in its entirety), flow rate was optimised independently of reagent concentration using a univariate approach. In all cases, the flow of each reagent was maintained at equivalent rates. The optimised reagent conditions used are described in Table 2.1. The effect of total flow rate on peak height was studied over the range 3.5 to 11.5mL.min^{-1}. As can be seen in Figure 2.3, the maximum peak height was observed at 4.5mL.min^{-1}, beyond which the peak

height was observed to decrease with increasing flow rate. The signal at 11.5mL.min^{-1} was approximately 30% less than that of the maximum. Flow rates less than 4.5mL.min^{-1} and greater than 7mL.min^{-1} resulted in increased variability of peak height when compared with flow rates between 4.5 and 7ml.min^{-1}. Furthermore, at flow rates below 4.5mL.min^{-1}, very broad peaks and a smaller throughput were observed. Consequently, a flow rate of 5.5mL.min^{-1} was chosen as a compromise between high reproducibility, narrow peak widths, and throughput.

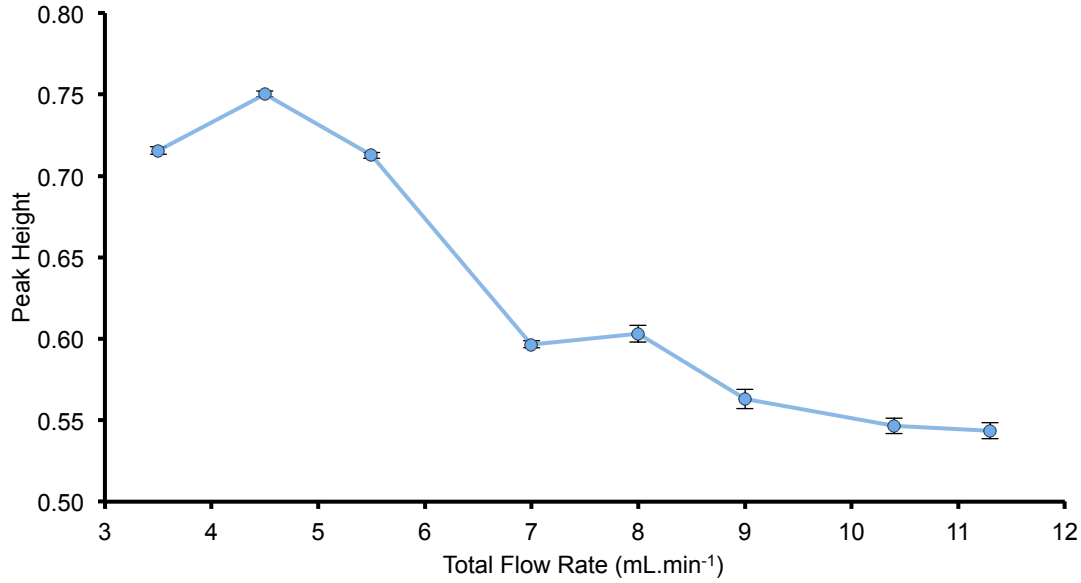

Figure 2.3 Effect of flow rate on measured peak height.
Error bars showing ±1 standard error. Conditions: 150mg.L^{-1} [Fe], 18MΩ water, 1.5%w/v 5-SSA, 1.5v/v ammonia, injection volume 30µL.

2.3.3 Calibration

A series of calibration standards were prepared in the region 5 to 150mg.L^{-1} and analysed using the optimised conditions described earlier. The resulting calibration curve had a linear trendline with the equation y=0.0035x+0.129 where y=peak height (AU) and x=iron concentration (mg.L^{-1}) and an R^2 value of 0.999. The limit of detection (blank+3σ) was 0.5mg.L^{-1}. Typical relative standard deviations were less than 2% with the highest relative standard deviation being 2.4% at the 5mg.L^{-1} level (n=10).

2.3.4 Interference studies

As pyrite is oxidised (either under the conditions described in this study or in the natural environment) sulfuric acid is formed. This decreases the pH of the

surrounding solution. In addition, pyrite can often contain many different elements as mineral inclusions or lattice substitutions which can occur in concentrations of up to several weight percent [3] and these elements would be released into solution. Therefore, it is important to know whether varying the acid concentration and trace element composition of the sample matrix will impact the analysis.

In order to determine the effect of additional acid on the system, known volumes of hydrochloric acid were added to the reaction matrix and the peak height for a 100mg.L^{-1} iron solution was monitored. Hydrochloric acid was chosen as it is a strong monoprotic acid and the additional hydronium concentration could be accurately calculated. As can be seen in Figure 2.4, the peak height is initially unaffected by increasing the acid concentration (from the original 1M) of the sample matrix by up to 0.2M after which there is a steady decrease in signal. The observed decrease in peak height is due to the pH of the analysed solution decreasing to a point where it is too low to evoke the full colour change. For detection of total iron by 5-SSA, a more concentrated ammonia solution would be required.

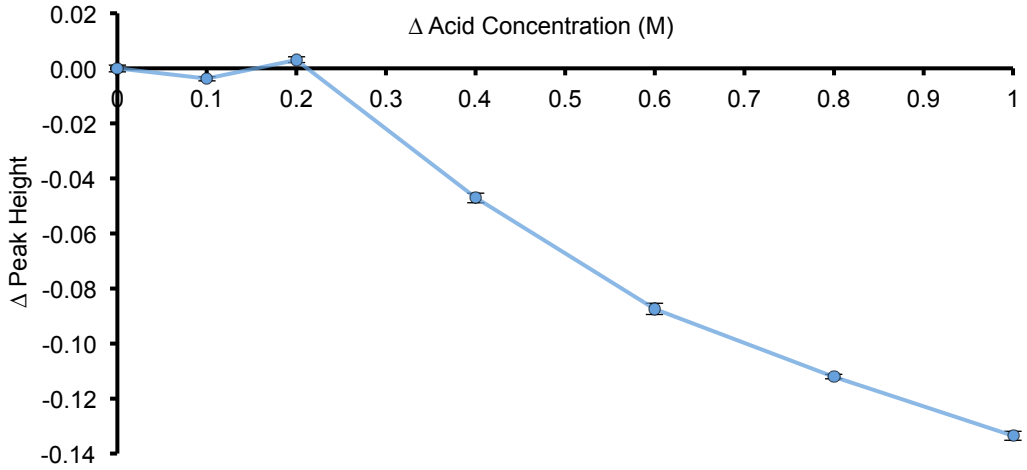

Figure 2.4 Effect of increasing acid concentration of sample matrix on peak height. *Conditions: 100mg.L-1 [Fe], 18MΩ water, 1.5%w/v 5-SSA, 1.5%v/v ammonia, flow rate 5.5mL.min^{-1}, injection volume 30µL.*

The addition of several different ions (As^{5+}, Co^{2+}, Cu^{2+}, Ni^{2+}, Sb^{3+}, Sn^{2+} and Zn^{2+}) commonly found as impurities in pyrite were investigated for their effect

on the signal peak height. Standard solutions of iron (100mg.L^{-1}) were individually spiked with the interfering ions under investigation and peak heights of the resulting solutions were compared with that of an un-spiked iron solution. The results of this study are summarised in Table 2.2. As shown, with the exception of antimony and zinc, which both resulted in a 5% decrease in signal, the method was not significantly affected by the presence of interferents at a 1:1 mole ratio. Whilst the presence of antimony and zinc resulted in a distinct decrease in absorbance at a 1:1 mole ratio, a 2:1 mole ratio (iron:interferent) did not significantly affect the peak height. It is thought that the decrease in peak height for antimony may simply be due to either the acidic nature of the supplied standard solutions (antimony was prepared in 5M hydrochloric acid (HCl) whilst all others were prepared in either 0.5M or 1.0M acid solutions). These concentrations of interferences would not normally be expected in a pyrite sample, as pyrite is not known to deviate significantly from the 1:2 Fe:S stoichiometry [3] and would normally contain only mg.kg^{-1} levels of the cations studied. Therefore, when applied to real samples, the method is essentially free from interferences.

Table 2.2 Effects of selected interferants on peak height.
The change in peak height as a % of the unspiked signal ±1 standard error from a 100mg.L^{-1} Fe solution (average signal 0.46AU) observed upon the addition of various elements.

Molar ratio (Fe:Interferent)	As (% change)	Co (% change)	Cu (% change)	Ni (% change)	Sb (% change)	Sn (% change)	Zn (% change)
1:0.01	0.8 ± 0.2	-1.9 ± 0.1	-2.0 ± 0.2	-0.3 ± 0.1	-3.5 ± 0.5	-1.0 ± 0.2	-0.7 ± 0.2
1:0.1	1.3 ± 0.3	-2.4 ± 0.1	1.3 ± 0.1	-0.5 ± 0.1	0.2 ± 0.2	0.0 ± 0.3	-3.8 ± 0.5
1:0.5	1.1 ± 0.2	-1.6 ± 0.2	0.9 ± 0.2	-0.2 ± 0.2	1.5 ± 0.5	0.9 ± 0.3	-2.1± 0.5
1:1	2.2 ± 0.4	0.2 ± 0.1	1.0 ± 0.3	-1.1 ± 0.2	-5.4 ± 0.4	-3.0 ± 0.4	-5.0± 0.3

2.3.5 Method validation

In order to confirm the results obtained using our colorimetric FIA system, the method for determining total iron was validated against an established ICP-MS method. The concentration of iron was determined for four subsamples of a pyrite oxidation that were taken at the same time as it was sampled for FIA. As can be seen in Figure 2.5 the concentrations of iron determined by the two methods correlated very strongly. Linear regressions of each set of data gave equations y=0.011x–1.60 and y=0.012x–1.54 for ICP-MS and FIA respectively.

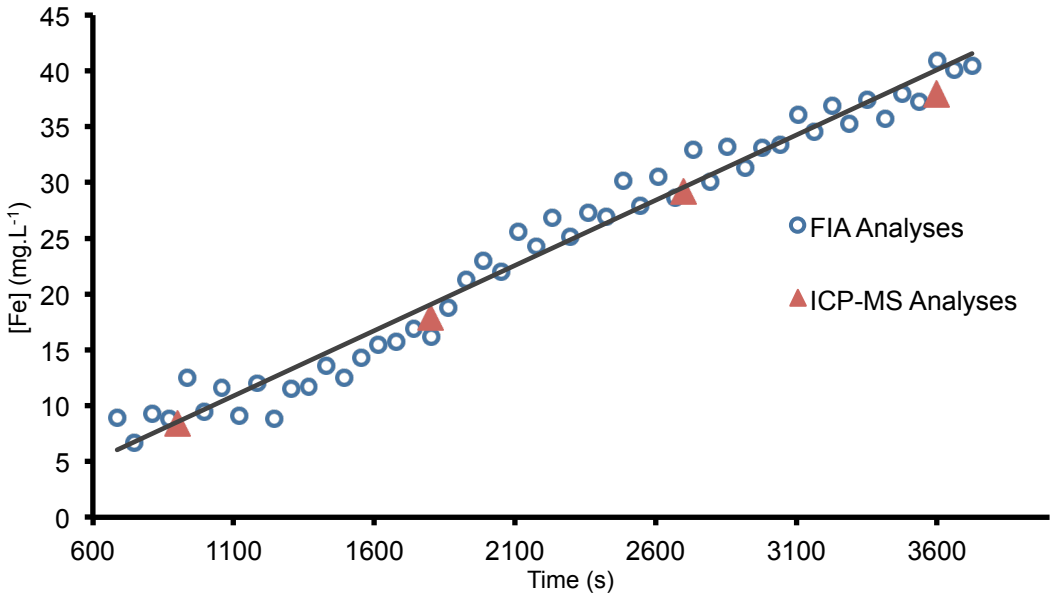

Figure 2.5 Comparison of FIA and ICP-MS methods for determination of total iron. *Error bars (where visible) show ±1 standard error. Solution from the reaction of 0.1g pyrite (Isle of Elba) in 2M H_2O_2 and 1M H_2SO_4 (50mL) sampled per minute for FIA and per 15 minutes for ICP-MS, reactivity=0.012mg.L^{-1}.s^{-1}. FIA Conditions: 1M H_2SO_4 sample matrix, 18MΩ water, 1.5w/v% 5-SSA, 1.5v/v ammonia, flow rate 5.5mL.min^{-1}, injection volume 30µL.*

2.3.6 Application to real samples

Pyrite samples from forty geographical locations were obtained from the South Australian Museum mineral collection (Table 2.3) and prior to reactivity analysis the diffraction spectra of the samples were collected to confirm their composition as pyrite. The unit cell dimension (*a*) for each sample is displayed in Figure 2.6. Sample G30334 (the Pacific Ocean sample) was found to contain a mixture of different minerals and sample G32407 (Buick Mine sample) was found to be marcasite, therefore, their unit cell dimensions are not displayed. Of the remaining samples, the majority did not deviate significantly from the mean value (5.4172Å, standard deviation=0.0007Å). The mean value is also very close to the literature value *a*=5.4179(11)Å [18]. Three samples; G29969 (Paulsens Mine), G32408 (He Chi, Guizhou) and G32706 (Weedon Mine) deviated further than one standard deviation from the mean suggesting that the sample may contain significant inclusions or impurities which cause the unit cell dimension to change. All samples were analysed for reactivity in triplicate using the optimised method as described in section 2.2.6.

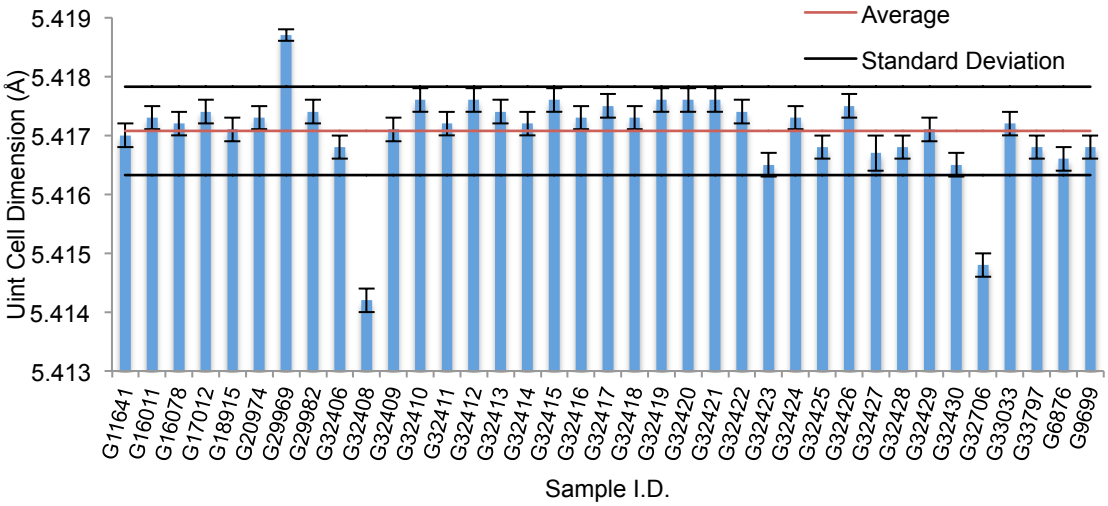

Figure 2.6 Unit cell dimensions for pyrite samples analysed by XRD.

Oxidation rate constants were derived for each sample and are presented in Table 2.3 (rates were converted into $\mu mol.L^{-1}.min^{-1}$ to facilitate further analysis). The samples gave an overall variation in rate constant of $19.3\mu mol.L^{-1}.min^{-1}$, with the highest measured constant being six times the magnitude of the smallest. The rate constant and standard errors of the triplicate analyses for each sample are also presented in Table 2.3. The standard errors are generally small suggesting good reproducibility of analyses. A statistical analysis of the measured reactivities is displayed in Table 2.4. The median value and the interquartile range thresholds are displayed on Figure 2.7. It can be seen that at least a quarter of the samples lie outside of the interquartile range, even after standard error is considered. This large range in reactivity is evidence supporting the hypothesis that pyrite from different locations do have different inherent reactivities. Interestingly, the reactivity of the sample identified as marcasite (G32407) does not deviate from the pyrite samples. Rather, it fits within the interquartile range of the sample population. The Pacific Ocean sample (G30334), identified to be a mixture of minerals, had the greatest reactivity of all samples.

Table 2.3 Geological origin and crystal habit of each of the pyrite samples.

Code	Origin	Rate constant ($\mu mol.L^{-1}.min^{-1}$)	Std error ($\mu mol.L^{-1}.min^{-1}$)
G33797	Huanzala Mine, Huallunca District, Dos de Mayo, Peru	3.7	0.2
G17012	Poona Mine, Moonta, South Australia	3.9	0.3
G32427	Ophir Hill Mine, Ophir, Tooele County, Utah, USA	4.3	0.6
G32422	Siglo XX Mine, Llallagua, Bolivia	4.8	0.4
G32706	Weedon Mine, Weedon, Quebec, Canada	5.3	0.9
G32414	Porthand Quarry, Florence, Fermont County, Colorado, USA	5.5	0.1
G32418	Eagle Mine, Colorado, USA	5.9	0.8
G32429	Midlothian, Ellis County, Texas, USA	6.1	0.7
G32406	Rio Marina Mine, Elba, Livorno Province, Tuscany, Italy	6.1	1.3
G32428	Concepcion del Oro, Zacatecos, Mexico	6.2	0.9
G18915	Gumeracha, South Australia	6.2	1.0
G32416	Four Metals Mine, Dugway Mts, Utah, USA	6.8	0.9
G32415	Showalters Quarry, Blue Ball, Pennsylvania, USA	6.8	1.4
G32412	Joaa Pessoa, Paraiba, Brazil	6.8	0.3
G32425	John Reed Mine, Lake County, Colorado, USA	6.9	1.1
G32420	Daly-Judge Mine, Peak City, Utah, USA	6.9	0.4
G32430	Rico, Delories County, Colorado, USA	7.1	0.8
G32409	Quiruvilca Mine, Peru	7.2	0.6
G32421	Qin Lon Mine, Guizhou Province, China	7.2	0.0
G32413	Liupanshui, Guizhou Province, China	7.4	1.0
G32408	He Chi, Guizhou Province, China	7.8	0.9
G33823	Guangdong, China	7.9	0.3
G16079	Panguna Copper Mine, Bougainville, PNG	8.2	0.4
G32426	Pucarajo Mine, Bolognesi Province, Ancash Dept, Peru	8.4	0.7
G16011	Nairne, Brukunga, South Australia	8.9	0.4
G9699	Young's Shaft, Wallaroo Mine, South Austraila	9.0	1.2
G32424	Nikolaevskiy Mine, Dal'Negorsk, Russia	9.2	0.8
G32411	Schwaberer Quarry, Nehawka, Nebraska, USA	9.5	0.2
G32407	Buick Mine, Vibunum Trend, Missouri, USA	9.7	1.0
G11641	Nairne Pyrite Mine, Brukunga, South Australia	9.8	0.7
G32423	Lomnice, Czech Republic	10.2	1.4
G32417	Chillicuthe, Ross County, Ohio, USA	10.3	0.1
G32410	Sweetwater Mine, Missouri, USA	11.0	0.8
G6876	Isle of Elba, Tuscany, Italy	11.6	1.6
G29982	Wuxian, Guangxi, China	12.5	2.5
G29969	Paulsens Mine, Wyloo, Western Australia	13.1	0.7
G33033	Victoria Mine, Navajun, Spain	13.6	3.2
G32419	Black Cloud Mine, Leadville, Colorado, USA	14.7	0.7
G20974	Sparta, Randolph County, Illinois	22.4	2.9
G30334	Pacific Ocean	22.9	1.4

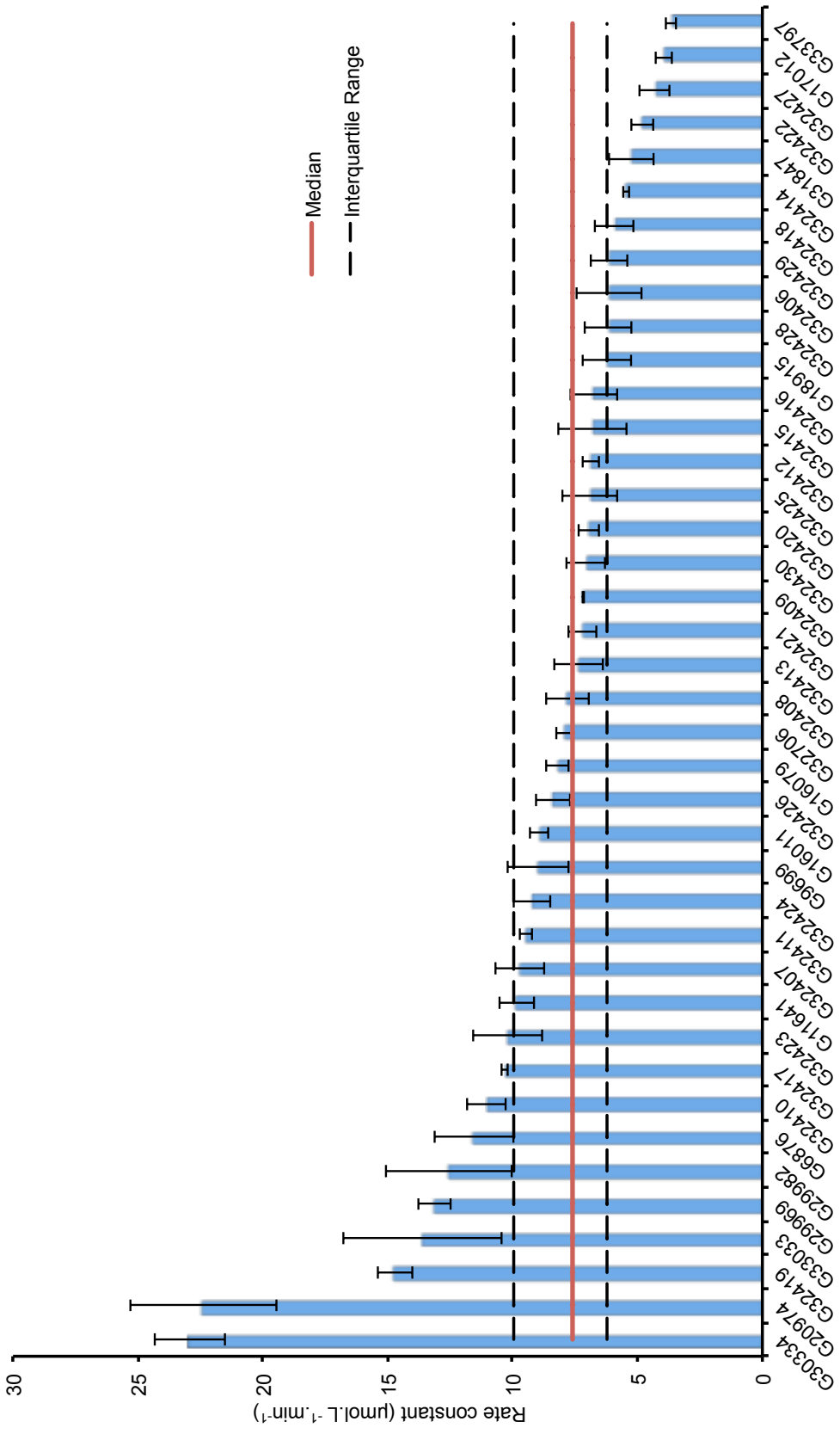

Figure 2.7 Rate constants for 40 pyrite samples. (Error bars ±1 standard error)

Table 2.4 Descriptive statistics for reactivity rates of 40 pyrite samples.

Parameter	Value
n	40
Median Reactivity (μmol.L^{-1}.min^{-1})	7.59
Minimum Reactivity (μmol.L^{-1}.min^{-1})	3.65
Maximum Reactivity (μmol.L^{-1}.min^{-1})	22.94
Range (μmol.L^{-1}.min^{-1})	19.29
25th Percentile (μmol.L^{-1}.min^{-1})	6.22
75th Percentile (μmol.L^{-1}.min^{-1})	9.93
Interquartile Range (μmol.L^{-1}.min^{-1})	3.71

2.4 Conclusion

An accurate, reproducible and rapid method for the analysis of total iron in mine drainage water using the colorimetric reagent 5-SSA in basic conditions has been developed. The method was successfully validated using ICP-MS at several iron concentrations. The method is also suitable for the routine determination of total iron concentration in mine drainage water as well as determination of the reactivity of mineral samples. The method does not suffer from interferences by several metal ions commonly associated with pyrite up to a ratio of 1:1 (molar), though it is sensitive to increases in sample matrix acidity above 0.2M.

The data presented above provides strong evidence to the inherent natural variation in reactivity between pyrite specimens from different geographical locations.

In order to elucidate the reasons behind this observed variation in reactivity, the variations in the composition and structure of the samples themselves should be examined. Chapter 3 describes the analysis of trace element composition of the samples using NAA. Chapter 4 then details the exploration of the trace element concentration data from the NAA as well as LA-ICP-MS analysis in terms of sample reactivity. Chapter 5 describes the characterisation of a subset of the samples presented above. The samples will be analysed in terms of chemical, electronic and physical variation.

Chapter 3.

Trace element analysis comparison.

3.1 Introduction

One of the main factors thought to affect the reactivity of pyrite is the composition of the mineral, particularly the minor and trace element contents [31]. Pyrite is a semiconductor and occurs in both the p-type and n-type forms. Elemental impurities are known to have a significant impact on this semiconductor behaviour. Elements frequently found as impurities in significant quantities (up to a few %w/w) in pyrite include: Ag, As, Au, Co, Cu, Ni, Sb and Sn. Other elements found in smaller quantities can include: Bi, Cd, Hg, Mo, Pb, Pd, Ru, Se, Te, Tl and Zn [3]. These inclusions may occur as lattice substitutions, or as inclusions of other minerals. According to a recent report by Deditius *et al.* [33] these inclusions may be on the nano-scale and, if homogenously distributed, can be mistaken for elements in solid solution during analysis if a high enough resolution is not employed. LA-ICP-MS may provide relatively high resolution, however, spot sizes are on the micron scale. Zhao *et al.* [85] notes that the trace element distribution in pyrite may vary over the same grain, where porous or fractured areas of a grain have elevated trace element concentrations compared to the intact areas.

The high sensitivity of NAA (sub-ppm for many elements) and the wide range of elements (50+) that can be analysed simultaneously make it an ideal method for the bulk analysis of geological samples for minor and trace element detection. Another advantage of NAA over other sensitive methods of trace element analyses, such as XRF or ICP-MS, is the minimal sample preparation that is required [86]. Typically, no lengthy digestion and extraction procedures are required for NAA. Therefore, the errors and uncertainties associated with sample preparation are minimised, which may be particularly significant in trace element analysis. A broad range of geological, biological or archaeological samples can be analysed by NAA with minimal matrix interference.

The more historically conventional method of NAA is based on standardisation using an appropriate reference material (RM) that is co-irradiated with the sample. The RM is matrix-matched as well as compositionally matched to include the elements of interest. This is known as

the relative comparator method. It may be constrained by the availability of RMs with suitable elemental content and concentration that match the sample [87]. There is also some concern regarding the limited quantity and cost of these RMs. Once a particular batch of RM material is exhausted, it becomes difficult to compare data sets from old and new RMs as the uncertainties are compounded.

The k_0-method of standardisation (k_0-NAA) is based on a mathematical parameterisation that uses experimentally determined constants, or k_0 factors, for the determination of each element. A standard, typically 0.01% Au in Al wire or foil, is co-irradiated with the sample as a monitor. As such, k_0-NAA is a single comparator method, with the significant convenience of being able to analyse many (75+) elements simultaneously, without the need for standards containing each element of interest. However, reactor and detector parameters must be well determined. Relative comparator NAA on the other hand has the benefit of being recognised as a primary ratio method [88]. These two methods of analysis have previously been evaluated by Popelka-Filcoff *et al.* [89] who concluded that both methods showed acceptable levels of precision and accuracy when analysing certified reference materials. Furthermore, Popelka-Filcoff *et al.* [89] showed that the analysis of ochres by both methods gave statistically indistinguishable results for the elements studied.

Pyritic samples have previously been analysed using both relative comparator [90] and k_0-NAA. However, there are no examples of studies comparing the analysis of specimens using both methods in the literature. This makes a comparison of the results obtained difficult without further analyses.

This chapter presents a direct comparison of the NAA trace element data obtained using both the relative comparator and k_0-NAA methods for a number of pyrite specimens. Specimens were collected from a range of different geological locations, and chosen so that they represent a wide range of geological environments. The k_0-NAA data was obtained from the Australian Nuclear Science and Technology Organisation (ANSTO) open-pool Australian lightwater (OPAL) facility (Lucas Heights, New South Wales,

Australia) and the relative comparator method data from the University of Missouri research reactor (MURR), (Columbia, Missouri, USA). k_0-NAA is establishing itself as an important and useful tool in geological science and this chapter serves to provide some insight as to how it compares to the more proven comparator method. Pyrite is a highly abundant and variable geological material (with respect to trace element concentration) and as such makes an important and interesting case for comparison. A further aim of analysing the k_0-NAA and comparator methods was to determine whether the results are statistically indistinguishable and whether the methods could, therefore, be used in combination to form a single data set of trace element data for all 40 pyrite samples.

3.2 Materials and methods

3.2.1 Sample selection and preparation

While all 40 pyrite samples were sent to be analysed at MURR we were restricted to comparing the NAA analysis of 30 pyrite samples instead of the total 40 due to the limit of funding for the analyses granted by the Australian Institute of Nuclear Science and Engineering (AINSE).

The 30 pyrite specimens were selected to represent a range of global occurrences. These are listed in Table 3.1. Two discrete sub-samples (approximately 5g each) from each of the 30 specimens were prepared separately by crushing using a steel pestle until the largest particles were less than approximately 2mm in diameter. The steel pestle was fitted with a disposable thick plastic cover, which was replaced between samples to prevent cross contamination. Similarly, the sample was contained in disposable plastic trays to maintain sample integrity. This resulted in two sets of 30 sub-samples. Samples were then stored in glass vials until they were prepared for NAA analyses.

Table 3.1 Pyrite sample ID numbers and geographical origins.

South Australian Museum ID	Geographical Origin
G20974	Sparta, Randolph County, Illinois, USA
G33033	Victoria Mine, Navajun, Spain
G9699	Young's Shaft, Wallaroo Mine, South Australia
G6876	Isle of Elba, Tuscany, Italy
G32429	Midlothian, Ellis County, Texas, USA
G32428	Concepcion del Oro, Zacatecos, Mexico
G32426	Pucarajo Mine, Bolognesi Province, Ancash Dept, Peru
G32425	John Reed Mine, Lake County, Colorado, USA
G32424	Nikolaevskiy Mine, Dal'Negorsk, Russia
G32423	Lomnice, Czech Republic
G32422	Siglo XX Mine, Llallagua, Bolivia
G32421	Quiruvilca Mine, Peru
G32420	Daly-Judge Mine, Peak City, Utah, USA
G32419	Black Cloud Mine, Leadville, Colorado, USA
G32418	Eagle Mine, Colorado, USA
G32417	Chillicuthe, Ross County, Ohio, USA
G32416	Four Metals Mine, Dugway Mts, Utah, USA
G32415	Showalters Quarry, Blue Ball, Pennsylvania, USA
G32414	Porthand Quarry, Florence, Fermont County, Colorado, USA
G32413	Liupanshui, Guizhou Province, China
G32412	Joao Pessoa, Paraiba, Brazil
G32411	Schwaberer Quarry, Nehawka, Nebraska, USA
G32410	Sweetwater Mine, Missouri, USA
G32409	Qin Lon Mine, Guizhou Province, China
G32407	Buick Mine, Vibunum Trend, Missouri, USA
G32406	Rio Marina Mine, Elba, Livorno Province, Tuscany Italy
G29982	Wuxian, Guangxi, China
G18915	Gumeracha, South Australia
G11641	Nairne Pyrite Mine, Brukunga, South Australia
G33797	Huanzala, Huallunca District, Dos de Mayo, Peru

3.2.2 Elemental analysis

Whilst the best approach to compare the performance of the two laboratories would be a careful and exhaustive homogenization of each sample prior to random sub-sampling, this is not the focus of this chapter. In this chapter, we have attempted to simulate a realistic situation where real samples are submitted for preparation and analysis by different laboratories according to each laboratories' standard operating procedure. This takes into account the extra variation that may result from non-homogeneity. For a detailed procedure for the ANSTO k_0-NAA analysis see [91], and for details on the relative comparator method at MURR see [92].

Accordingly, one set of sub-samples was sent to ANSTO for analysis by the k_0-NAA method, the remaining set was submitted to MURR for analysis by the relative comparator method.

At ANSTO two sub-samples were taken from each pyrite sample for subsequent short and long irradiations in the OPAL pneumatic facilities. Around 60mg was weighed into high-purity polyethylene capsules. Short irradiations were carried out for 1 minute at a neutron flux of around $1.5\times10^{13}cm^{-2}.s^{-1}$ and gamma-ray spectra were accumulated for 180s and 720s after decay times of around 4 minutes and 18 minutes respectively. Long irradiations were for 12 hours at around $4\times10^{12}cm^{-2}.s^{-1}$ and gamma-ray spectra were accumulated for 30 minutes and 4 hours after 4 days and 15 days respectively.

At MURR two sub-samples were prepared for each pyrite sample for subsequent short and long irradiations. Around 75mg was weighed into high-purity polyethylene vials used for short irradiations and 100mg was weighed into high-purity quartz vials used for long irradiations. Standard reference materials (SRM) from SRM1633b Coal Fly Ash and SRM278 Obsidian Rock were similarly prepared. Short irradiations were carried out for five seconds at a neutron flux of $8x10^{13}cm^{-2}.s^{-1}$ and gamma-ray spectra were accumulated for 720s after decay times of 25 minutes. Long irradiations were for ten hours at a neutron flux of $5x10^{13}cm^{-2}.s^{-1}$ and gamma-ray spectra were accumulated for 30 minutes after 7 days of decay and again for 2 hours after 28 days of decay.

The data collected from ANSTO and MURR was compared to NAA data from a previously published work by Lodders *et al.* [93], who analysed pyrite from Victoria Mine (G33033).

3.2.3 Data Analysis

As expected, the range of elements reported in the ANSTO and MURR analyses were different. ANSTO reported the trace element concentration of 50 elements and MURR measured 32 elements. The data sets were initially reduced so that only the 32 elemental concentrations that were reported by both institutions were compared. Cs, Nd, Lu, Rb, Sr, Ta, Tb, Yb and Zr were removed from the statistical comparison as they were generally reported at concentrations below the limits of detection (LOD) in one or other of the two data sets. This resulted in an insufficient number of paired data sets between methods (<3) because of the very small concentrations of these elements in pyrite. The final list of elements compared was Al, As, Ba, Ce, Co, Cr, Dy, Eu, Fe, Hf, K, La, Mn, Na, Ni, Sb, Sc, Sm, Th, Ti, U, V and Zn.

Initial comparison of the data was undertaken using a paired t-test at the 0.05 significance level. The paired elemental data sets were also analysed using a least squares linear regression (OriginPro 7.5, OriginLab, Hearne Scientific, Melbourne, Australia). ANSTO data was arbitrarily set to the x-axis and MURR to the y-axis, where an ideal correlation between the two methods would yield a slope, intercept and R^2 value of 1, 0 and 1 respectively. Data sets were first assessed on two factors: (1) the closeness of the slope to 1 and (2) the goodness of fit of the data to that slope as determined by the R^2 value. Data sets where the regressions appeared to be skewed by large outlying data points were subsequently treated using a weighted regression with the weighting factor $W = \frac{1}{c_i^2}$ (c being the data where outlying point is observed).

Elemental data from the ANSTO and MURR analyses of the Navajun, Spain sample was compared with that of a previously reported data set [93]. Lodders *et al.* [93] also analysed the pyrite sample using NAA but do not give any more experimental detail. Again, only elements common to all three analyses were compared. In this case the elements comprised: As, Ce, Co,

Cr, Dy, Eu, Hf, K, La, Mn, Na, Nd, Ni, Sb, Sc, Sm, Ta, Tb, Th, U, Yb and Zn.

3.3 Results and discussion

Unprocessed trace element data, LOD and uncertainties for the 30 samples analysed at ANSTO and 40 samples analysed at MURR are provided in Appendix A.

3.3.1 Quality control data

The quality control (QC) data for ANSTO and MURR are presented in Table 3.2 and Table 3.3 respectively. The QC data for ANSTO shows good agreement (generally less than 5%) between their reference materials and measured values. The largest differences between measured and expected values were As and Ca from SRM-1633b which had differences of around 17%. More accurate values for these two elements were measured in the SMELS-II (synthetic multi-element standard) and SRM-679 standards, where the As difference was around 2% and Ca was around 10%.

The MURR QC data shows most measurements are accurate to around 5%, with some notable exceptions. In SRM-1633b Ba was approximately half of the certified value. In SRM-278 the value measured for Ni is greater than double the certified value. In SRM-688 Dy has a 10% difference from the certified concentration.

Table 3.2 Quality control data for the NAA analysis of pyrite by ANSTO.

Reference material	Element	Certified concentration (ppm)	Measured concentration (ppm)
SMELS-I	Au	82.7	84.9
	Cl	4330	4600
	Cs	897	934
	Cu	3930	4130
	I	152	160
	La	265	266
	Mn	113.9	119
	V	39	40
SMELS-II	As	92.3	90.4
	Au	3.93	3.94
	Br	157	164
	Ce	15600	15520
	Mo	5170	5230
	Pr	1193	1240
	Sb	172	170.5
	Th	3670	3580
	Yb	187	198
	Zn	6570	6490
SMELS-III	Au	0.901	0.904
	Co	24.3	24.61
	Cr	86.7	84.82
	Cs	20.8	19.96
	Fe	8200	8270
	In	462	471.8
	Sb	51.2	50.35
	Sc	1.14	1.15
	Se	131	139.4
	Sr	8150	8120
	Th	26.2	26.4
	Tm	23.3	22.12
	Yb	20.7	20.76
	Zn	618	627.6
	Zr	4580	4710
SRM-1633b	Al	150500	163000
	As	136.2	116
	Ba	709	746
	Ca	15100	12800
	K	19500	19900
	Mg	4820	4610
	Mn	131.8	133
	Na	2010	1940
	Sr	1041	1130
	Ti	7910	7950
	U	8.79	8.88
	V	295.7	327
SRM-679	Al	110100	120000
	Ba	432.2	441
	Ca	1628	1480
	Cr	109.7	105
	Fe	90500	89700
	K	24330	23800
	Mg	7552	8080
	Na	1304	1360
	Ti	5770	5720

Table 3.3 Quality control data for the NAA analysis of pyrite by MURR.

Reference material	Element	Certified concentration (ppm)	Average concentration (ppm)
SRM-278	As	4.7	4.6
	Ce	61.4	62.4
	Co	1.44	1.47
	Cr	6	6.5
	Cs	5.1	5.11
	Eu	0.766	0.762
	Fe	13980	13845
	Hf	8.09	7.92
	La	30.1	30.04
	Lu	0.682	0.653
	Nd	25.4	25.4
	Ni	9	20.6
	Rb	126	124.53
	Sb	1.6	1.4
	Sc	4.96	4.93
	Sm	5.8	5.94
	Sr	64	60
	Ta	1.24	1.30
	Tb	0.951	0.97
	Th	11.65	11.85
	U	4.46	5.28
	Yb	4.5	4.5
	Zn	54	56.7
	Zr	290	205
SRM-688	Al	91880	89258
	Ba	167	178
	Dy	3.3	2.62
	K	1550	ND
	Mn	1290	1387
	Na	15890	14721
	Ti	7000	6511
	V	260	255

3.3.2 Concentration data

Table 3.4 shows the range of concentrations detected for each element along with the number of samples in which that element was found in levels above the LOD. The LOD for each method is also shown. In the case of the ANSTO data a LOD was calculated for each individual determination, so the average LOD of all determinations is displayed; individual LODs for the ANSTO analysis are available in Appendix A.

Table 3.4 Overview of NAA elemental concentration data.
including limit of detection (LOD) and number of samples found to contain each element for ANSTO and MURR's analyses.

	ANSTO			MURR		
	Concentration range (ppm)	Average LOD (ppm)	Number of times detected	Concentration range (ppm)	LOD (ppm)	Number of times detected
Al	2.673 - 6625	1.45	30	<LOD - 10737	500	22
As	0.4426 - 9551	0.706	30	<LOD - 8711	8	26
Ba	4.173 - 37.32	13.6	6	<LOD - 50.93	40	6
Ce	0.7611 - 28.04	0.915	11	0.7443 - 31.78	0.02	10
Co	0.3963 - 2465	0.112	30	0.5277 - 2242	0.02	30
Cr	2.368 - 56.22	1.87	8	1.820 - 30.58	0.45	28
Dy	0.02179 - 2.532	0.0693	15	<LOD - 2.103	0.2	7
Eu	0.009054 - 0.6550	0.0178	12	<LOD - 0.6997	0.01	10
Fe	420200-474500	127.0	30	428000 - 456900	15000	30
Hf	0.1831 - 186.3	4.70	7	<LOD - 5.670	0.2	6
K	42.11 - 903.2	72.8	17	<LOD - 1023	400	8
La	0.02602 - 13.80	0.0488	20	<LOD - 16.13	0.08	18
Mn	0.4928 - 1168	0.118	30	3.138 - 796.3	0.2	30
Na	4.327 - 253.6	0.433	28	22.41 - 288.5	10	30
Ni	260.0 - 2943	695	5	<LOD - 2746	60	11
Sb	0.2111 - 67.29	0.137	23	<LOD - 70.55	0.05	24
Sc	0.05966 - 0.9004	0.0190	16	0.03720 - 1.080	0.01	14
Sm	0.01266 - 2.391	0.0367	16	0.06570 - 2.729	0.05	10
Th	0.2208 - 8.009	0.219	10	0.1165 - 8.397	0.1	11
Ti	8.652 - 2267	27.0	14	967.9 - 3554	600	30
U	0.7317 - 10.13	0.430	5	<LOD - 2.977	0.8	4
V	0.07515 - 47.01	0.0823	28	<LOD - 20.70	2	8
Zn	14.57 - 6253	4307	13	4.210 - 465.2	4	15

As shown in Table 3.4, the range of Fe concentration reported by each method correlates well. The average concentration and standard deviation of Fe across the 30 pyrite samples was 45±1.4%w/w for ANSTO and 44±0.8%w/w for MURR. These results are both consistent with the expected concentration of Fe in pure pyrite (46.5%w/w), and correlate well with each other. There is some variation in the Fe concentration across the 30 samples. This is to be expected as the sample set comprises of specimens from a variety of geological origins. The Fe content of samples may vary as a result of small concentrations of inclusions and/or lattice substitutions. The variation in Fe content across the 30 samples was less than 3%RSD for both methods. This indicates that the samples are of relatively high purity and suitable for use in comparing the trace element data from the two NAA methods.

Preliminary analysis of the trace element data comprised of inspecting each of the samples for paired data, this is where concentration values for an element were reported for a particular sample by both the k_0-NAA (ANSTO) and relative comparator (MURR) analyses. Conversely unpaired data is where only one facility detected a statistically significant concentration for an element in a particular sample. When considering the final 23 elements across the 30 pyrite samples examined, there were 146 examples of unpaired data. Of these, 56 were elemental concentrations detected in the ANSTO analysis at values that fell below the LOD of the MURR analysis. Similarly, 12 elemental concentrations were reported by MURR at a level that fell below the ANSTO LOD. Unpaired data points that result from the difference in sensitivity between the two analyses have obvious practical implications but need to be discounted for this statistical comparison. It can be seen in Table 3.4 that the ANSTO method has a smaller LOD than MURR in regard to Al, As, Dy, K and V, which is reflected in the number of unpaired samples in the top row of Table 3.6. Similarly, the MURR method has a lower LOD for Ni and Zn, as demonstrated by the corresponding unpaired data points displayed in the second row of Table 3.6.

The remaining 78 unpaired data points are more significant as theoretically the elements should be reported by both methods. Of these 78 occurrences, 25 instances exist where there is ANSTO data but no corresponding MURR

data and 53 instances where there is MURR data but no corresponding ANSTO data. This data is broken down on an elemental basis in Table 3.5.

Considering that in any analysis there is a greater probability of false negative results associated with determinations that fall near to the LOD, much of this unpaired data is most likely due to false negatives. Though there is not one standard method for establishing the LOD and limit of quantitation (LOQ), a widely used practice is for the LOD to be set as the average signal noise measurement plus 3 times its standard deviation, and the LOD to be the signal noise measurement plus 10 times its standard deviation [94]. The Kayzero for Windows Vade Mecum [95] describes the procedure for calculation of detection limits used at ANSTO and states that it is done according to Currie [96].

Assuming that the standard deviation is not a great deal larger or smaller than the noise we can assume a quantitation limit approximately 3 times greater than the detection limit. Therefore, unpaired data at a concentration which is within 3 times the detection limit of the other facility has a larger chance of being a false negative result. The ratios of the unpaired elemental concentrations to the limit of detection of the alternate analysis are displayed in Table 3.6 where a ratio of 3 or less indicates that the value falls close to the LOD.

3.3.3 Inconsistencies in the data

Sample G32424 showed a significant discrepancy between the concentration of Zn reported by MURR and the LOD reported by ANSTO. The concentration reported by MURR was 244.8 times greater than the LOD reported by ANSTO, yet ANSTO did not report a concentration for Zn. The origin of this sample (G32424) is Nikolaevskiy Mine, Dal'Negorsk, Russia, a site known to contain a range of sulfide minerals including sphalerite (ZnS). Therefore, this discrepancy is likely to be due to ZnS inclusions within the MURR sample that are not present in the ANSTO sample. Similarly, values of Al (G9699), K (G32421 and G32410) and Na (G32425 and G11641) which also display large ratios of reported concentration to LOD could be due to the inclusion of clays and feldspars within the samples.

It can be seen in Table 3.6 that MURR reported concentration data for Cr for

20 samples; however, ANSTO did not report a Cr concentration for any of these same samples. Comparing the two sets of analyses, 17 of the reported MURR concentrations are quite small (generally below 5ppm) and are very close to the ANSTO detection limits (average 1.9ppm) and as such should be compared with caution. The three remaining unpaired Cr concentrations (MURR) were reported at levels significantly larger than three times the ANSTO LOD (Table 3.5) were not a result of larger than average Cr concentrations, but resulted from a significantly lower than average LOD reported by ANSTO. The average Cr LOD for ANSTO was 1.9ppm, while the LOD reported by ANSTO for the samples in question were 0.08, 0.04 and 0.25ppm. The ANSTO results are further complicated by the low level of Cr (~0.4µg) found in the irradiation capsules. Whilst this blank value has been subtracted by ANSTO, the LOD calculation does not take it into account. As a result, the calculation of the LOD by the ANSTO analysis was underestimated. The 16 unpaired Ti data points reported by MURR are thought to be due to contamination issues as discussed in section 3.3.5.

Table 3.5 Categorisation of unpaired elemental concentration data between the ANSTO and MURR analyses.

Data Point Detected by	ABOVE/BELOW LOD of Alternate Analysis	Al	As	Ba	Ce	Co	Cr	Dy	Eu	Hf	K	La	Mn	Na	Ni	Sb	Sc	Sm	Th	U	V	Zn	TOTAL
ANSTO	BELOW	7	4	3	0	0	0	8	1	1	11	2	0	0	0	0	0	4	0	0	15	0	56
MURR	BELOW	0	0	0	0	0	0	0	1	0	0	0	0	0	5	1	0	0	1	0	0	4	12
ANSTO	ABOVE	1	0	0	2	0	0	0	3	1	1	2	0	0	0	2	2	2	1	1	5	2	25
MURR	ABOVE	0	0	3	1	0	20	0	1	1	3	2	0	2	1	2	0	0	1	0	0	0	37

Table 3.6 Ratio of detected element concentration to the limit of detection of the alternate analysis for unpaired data.

	Al	Ba	Ce	Cr	Eu	Hf	K	La	Na	Ni	Sb	Sc	Sm	Th	U	V	Zn
Ratio [ANSTO]/MURR LOD	1.38		***47.3**, **38.1**	-	**8.71**, 1.12, 1.71	**931.5**	1.16	**7.40, 5.50**	-	-	**731.6, 18.2**	**12.1, 5.97**	3.06, 1.48	**7.54**	1.06	1.22, 1.07, 1.16, 1.35, **12.7**	**3.64**
Ratio [MURR]/ANSTO LOD	-	1.02, **3.78**, 1.14	**8.00**	1.72, 1.31, **86.5,** 1.37, 2.56, 1.92, 1.46, **37.2**, 3.32, 2.61, 2.63, 1.93, 1.52, **7.37**	1.69, 2.73, 1.32, 2.08, 1.83, 1.95, 1.12	1.21	**5.00, 21.3,** 2.63	1.78, **4.40**	N/A, 2.16	1.40	1.91, **3.65**	-	-	1.32	-		**244.8**

*Values in bold highlight samples where the ratio of concentration to LOD was greater than 3 and hence were deemed above the limit of quantitation.

3.3.4 Statistical comparison of data

Table 3.7 shows the results from the paired t-tests. The results show that for all but 5 of the elements (Al, Na, Ni, Sc and Ti) the data was indistinguishable at the 0.05 confidence level. Of those that were different at the 0.05 confidence level, Ni and Sc were indistinguishable at the 0.01 level. The poor correlation between the two Ni data sets may relate back to the QC data (Table 3.3) where the Ni concentration measured by MURR was almost double the certified value of the RM. The QC data for Sc showed a good agreement between the measured and certified values so the reason for the disparity for the Sc may simply relate to sample homogeneity. Al, Na and Ti were still statistically different at the 0.01 significance level and this data is further discussed later in the text.

Table 3.7 Results of paired t-test comparing elemental concentration data.
Data reported by ANSTO and MURR analyses of 30 pyrite samples.

Element	Degrees freedom	t-experimental	t-critical (α=0.05)	Pass/Fail at (α=0.05)	t-critical (α=0.01)	Pass/Fail at (α=0.01)
Al	21	3.06	2.08	F	2.83	F
As	25	0.17	2.06	P		
Ba	2	3.23	4.30	P		
Ce	8	0.30	2.31	P		
Co	29	0.71	2.05	P		
Cr	7	0.59	2.37	P		
Dy	6	0.37	2.45	P		
Eu	7	0.78	2.37	P		
Hf	4	0.65	2.78	P		
K	4	1.88	2.78	P		
La	15	0.11	2.13	P		
Mn	29	1.94	2.05	P		
Na	27	5.53	2.05	F	2.77	F
Ni	4	2.89	2.78	F	4.60	P
Sb	20	0.55	2.09	P		
Sc	13	2.26	2.16	F	3.01	P
Sm	9	0.76	2.26	P		
Th	8	0.52	2.31	P		
Ti	13	10.71	2.16	F	3.01	F
U	3	0.79	3.18	P		
V	7	0.95	2.37	P		
Zn	10	1.35	2.23	P		

Figure 3.1 shows the slope of the linear least squares regression performed for the paired data set of each element, where complete agreement between the data sets has the value of 1. A weighted regression was performed for the sets where large outliers were observed.

The majority of the points lie within +/-0.5 of 1. Ba has a large associated error due to the very small sample size (of 3). Cr, Mn, U, V and Zn all show an improved slope after weighted regression accounts for large outliers. Despite the small t-value obtained from the paired t-test for As, the regression does not show a good correlation between the two analyses. The small t-value is due to large outliers in both the x and y directions, which cancel each other and result in a small average difference between the analyses. The weighted regression was unable to correct for these 3 large outliers, so they were removed from the regression to yield an acceptable slope. This example illustrates why it is necessary to perform more than one statistical analysis on a set of data.

The errors associated with the weighted regressions are generally larger than those of the least squares regressions, this is because the weighted fit draws the regression line away from the outliers, resulting in larger residuals, which in turn cause larger errors.

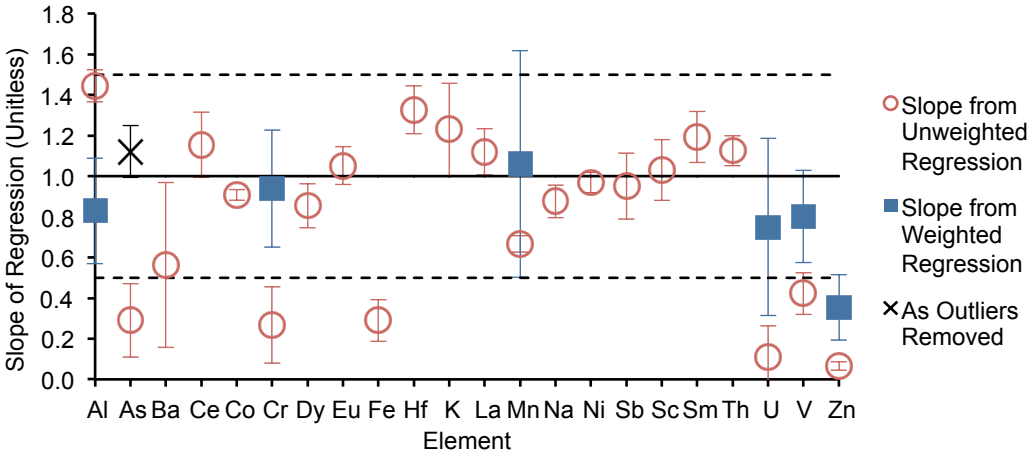

Figure 3.1 Plot displaying the slope from linear regression of each elements paired data set.
Solid line indicates an ideal value of 1, and dashed lines show slope values of 0.5 and 1.5. Error bars show 1± standard error of the slope.

There is always a degree of uncertainty in the undertaking of trace element analysis of geological samples that may not be homogenous. Pyrite is known to contain inclusions of other minerals within its crystals, such as ZnS, CoS_2 FeAsS, and this may explain some of the deviation between the two methods, particularly the large outliers found in the linear regression analysis. Pyrite crystals also commonly show growth zoning, with associated

zoning of trace elements, leading to heterogenous crystals [97, 98]. The most sound way to reduce the potential for error is to either increase the size of the samples or to run multiple samples.

3.3.5 Examination of Al, Na and Ti results

Further examination of the Al, Na and Ti data indicates that there may be some systematic error in the determination of these elements in the MURR analysis. The QC data for all three of these elements showed good agreement with the published values of the RMs (Table 3.2 and Table 3.3) so it is likely that the error is not due to either of the institutions' analyses. It is thought that these errors are due to contamination during sample preparation as discussed below.

Figure 3.2a shows a plot of the concentration of Al as determined by ANSTO (x-axis) versus the concentration of Al as determined by MURR (y-axis). As can be seen, when the concentrations are above 500ppm (the MURR LOD, Figure 3.2a) the Al concentrations reported by both MURR and ANSTO correlate reasonably well with the ideal regression. Around this limit (500ppm) the results reported by MURR are elevated in concentration when compared with ANSTO results. This apparent deviation may be due to the large uncertainties encountered when working at concentrations close to the detection limits. However, a likely explanation is a background Al contamination of the MURR samples (a conservative value of 250ppm is estimated). The data was replotted in Figure 3.2b taking into account this estimate of the background. As can be seen in Figure 3.2b the data exhibits an improved correlation, with the y-intercept of the regression dropping from 225ppm to -25ppm. A paired t-test is used to compare the background corrected data; the results of this are shown in Table 3.8. The results show that the experimental t-statistic is now well below the critical value indicating that the data sets are not significantly different at the 0.05 level. This supports the theory that there is a systematic elevation of the recorded concentrations due to background interferences.

A plot of MURR concentration data against ANSTO concentration data for Na is constructed in Figure 3.3a. In this case the Na results correlate well at concentrations above 40ppm; below this threshold the MURR concentrations

appear to be overestimated when compared with ANSTO. This level (40ppm) is four times the MURR LOD for Na and well above the ANSTO LOD (0.43ppm). As with Al, the Na data was replotted with the background subtracted (using an estimate of approximately 30ppm), which is shown in Figure 3.3b. Once again, an improvement is seen in how the data correlates to the ideal regression; the y-intercept is reduced from 41ppm to 11ppm and the experimental t-statistic is decreased from 5.53 to 0.707 (Table 3.8), well below the critical value of 2.05 at the 0.05 significance level. As with the results of Al, a possible explanation for the observed trends in Na is the presence of a background level of Na.

Figure 3.4a shows the ANSTO and MURR concentrations for Ti plotted against each other. It can be observed that the values reported by MURR are consistently around 1600ppm greater than those of ANSTO. The subtraction of a background estimated conservatively at 1050ppm yields a better fit to the ideal regression (shown in Figure 3.4b) resulting in a reduction of y-intercept of over 50% (1744ppm to 693ppm). However, much of the MURR data is still significantly greater than ANSTO's implying some background effects remain. The t-statistic of the background-subtracted data (Table 3.8) is still larger than the critical values for both the 0.05 and 0.01 significance levels. Once again the QC results for Ti from both facilities (samples prepared by the facilities) were consistent with reported values for RMs (Table 3.2 and Table 3.3) it is thought that this disparity is likely to be due to background contamination from TiO_2 within the plastic used during sample preparation process for the MURR samples.

These background interferences highlight the particular attention to sample preparation that is required for accurate NAA analysis. It is suggested that for future studies a high purity quartz sample be prepared and analysed along with the mineral specimens. This would allow a direct measure of any background contaminants resulting from the sample preparation procedure.

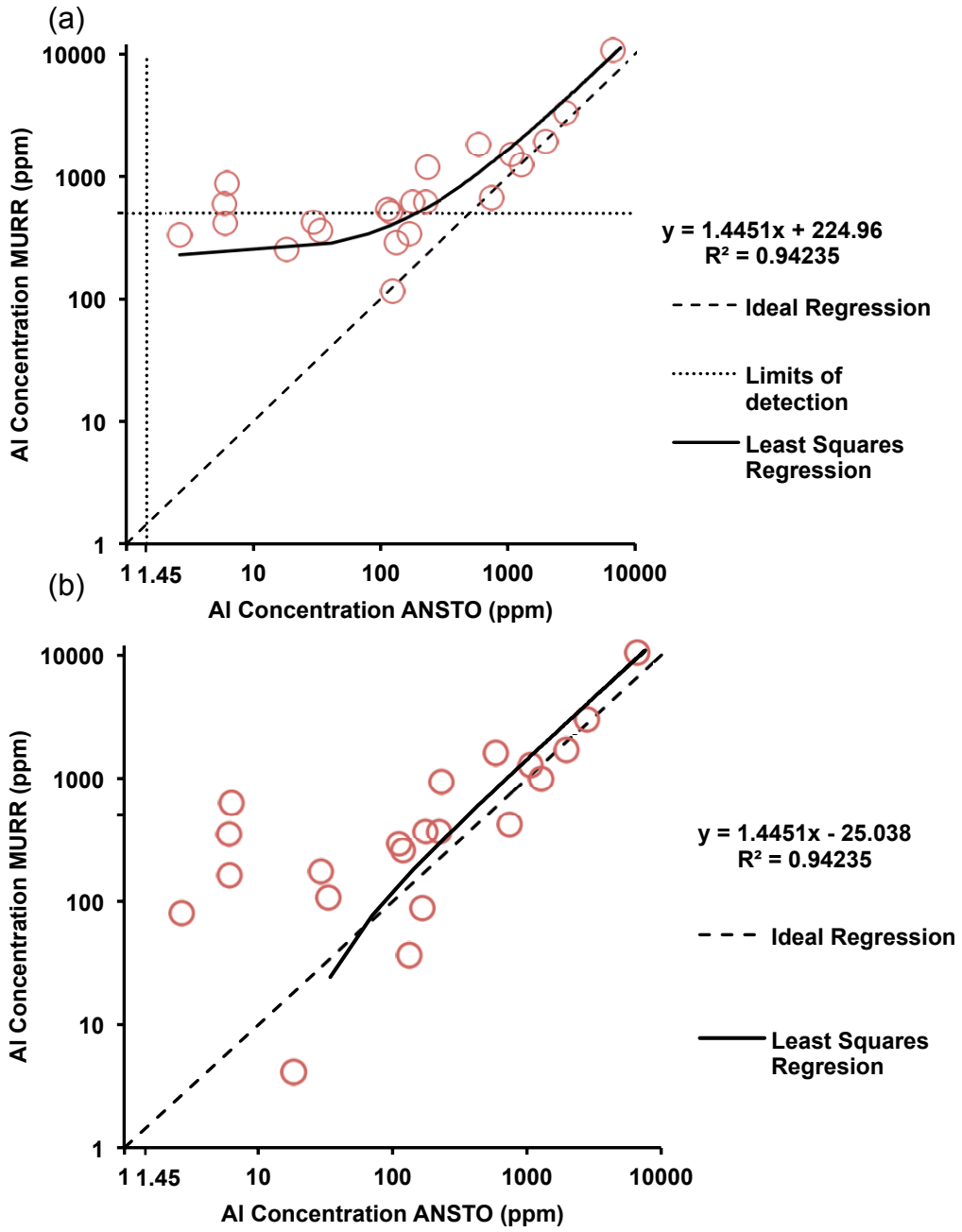

Figure 3.2 Scatter plots comparing Al concentration.
(a) Scatter plot comparing the reported Al concentration from ANSTO and MURR, the solid line depicts the linear regression, dashed line represents an ideal correlation and the dotted lines represent the reported limits of detection (500 ppm by MURR and 1.4 ppm by ANSTO), (b) Data replotted with 250ppm background subtracted from MURR data. Also note log scale.

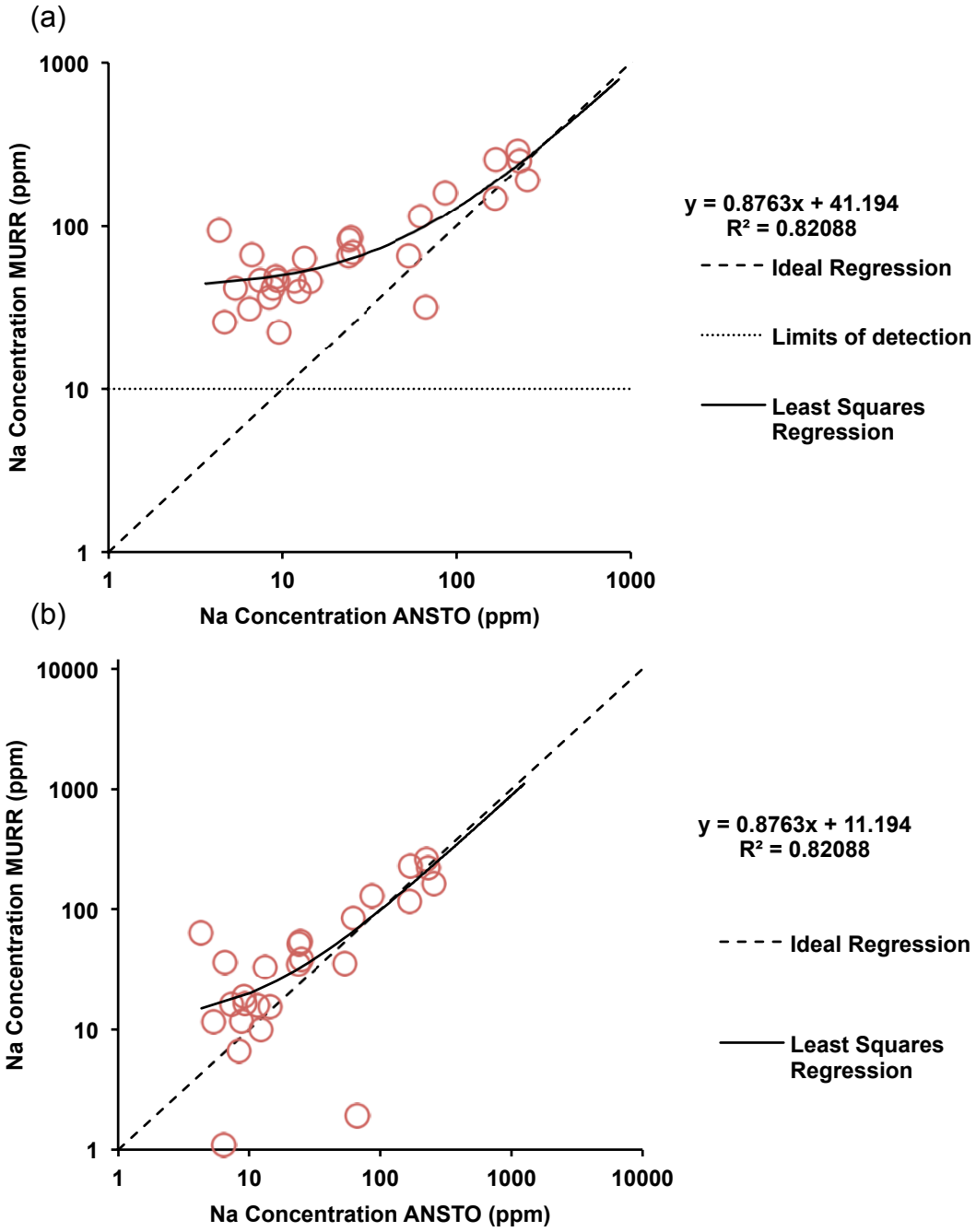

Figure 3.3 Scatter plots comparing Na concentration.
(a) Scatter plot comparing the reported of Na concentration from ANSTO and MURR, solid line depicts the linear regression, dashed line represents an ideal correlation and the dotted line represents the limit of detection reported by MURR (10 ppm). The average ANSTO LOD was 0.43ppm and could not be displayed on the figure. (b) Data replotted with 30ppm background subtracted fom MURR data. Also note log scale.

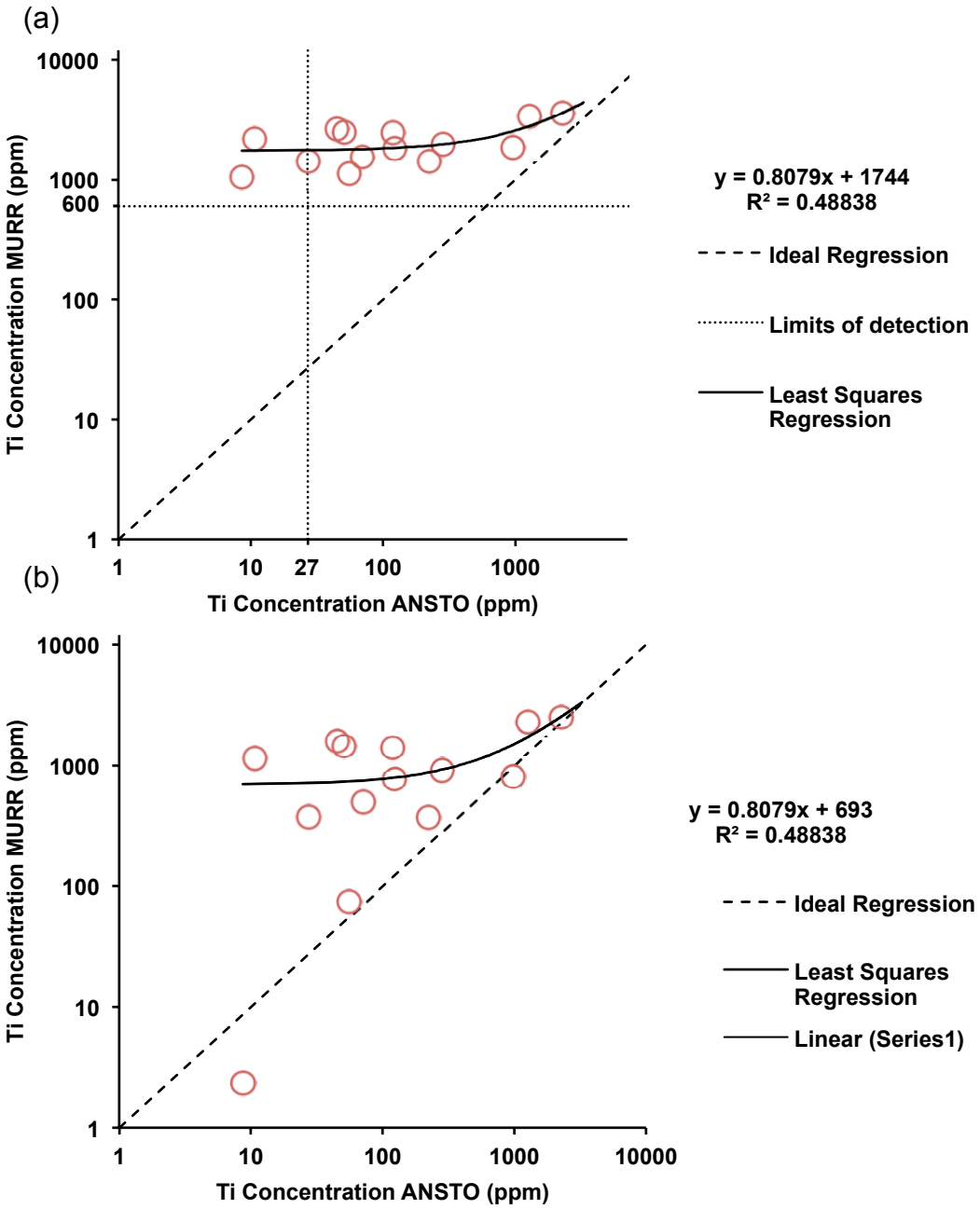

Figure 3.4 Scatter plot comparing Ti concentrations.
(a) Scatter plot comparing the reported Ti concentration from ANSTO and MURR, the solid line depicts the linear regression, dashed line represents an ideal correlation and the dotted lines represent the reported limits of detection (600ppm by MURR and 27ppm by ANSTO), (b) Data replotted with 1050ppm background subtracted from MURR data. Also note log scale.

Table 3.8 Results of paired t-test comparing elemental concentrations of ANSTO with MURR (background subtracted).

Element	Background subtraction (ppm)	Degrees freedom	t-experimental	t-critical (α=0.05)
Al	250	21	1.69	2.08
Na	30	27	0.707	2.05
Ti	1050	13	3.97	2.16

3.3.6 Comparison to previously reported results

A comparison of the analyses of pyrite samples from Victoria Mine (G33033) by ANSTO and MURR in addition to the data presented in Lodders *et al.* [93] is shown in Table 3.9 and Figure 3.5. Visually the three analyses correlate well with each other, this is confirmed by the results of the t-tests shown in Table 3.10. All three of the experimental t-values are well below the critical t-value verifying that the samples are not statistically different from each other.

Individual data points that do not correlate well include Ta, where the ANSTO value is over 5 times greater than both the MURR and Lodders *et al.* [93] values. The Na, Co, K and Zn values reported by Lodders *et al.* [93] are all significantly smaller than those reported by ANSTO and MURR. This variation may simply be due to compositional variation between different locations within the mine, as the ANSTO and MURR data was obtained from a single pyrite cube while Lodders *et al.* [93] analysed a different sample. Na and K are also quite common and their observed variation is almost certainly affected by traces of common layer silicate such as chloritoid. The result implies that the pyrite samples from this site are fairly homogeneous with respect to trace element concentration and that the analyses by all three facilities are comparable.

Table 3.9 Trace element data from the NAA of pyrite from Victoria Mine.

	ANSTO		MURR		LODDERS	
Element	Concentration (ppm)	Uncertainty (ppm)	Concentration (ppm)	Uncertainty (ppm)	Concentration (ppm)	Uncertainty (%)
Tb	0.377	0.02938	0.4019	0.060285	0.41	3
Eu	0.655	0.02662	0.6997	0.013994	0.548	5
Sc	0.9004	0.03386	1.0798	0.010798	1.7	3
Sb	0.9774	0.06412	2.8728	0.14364	1.6	4
Yb	1.303	0.06719	1.2034	0.084238	1.63	5
Hf	2.119	0.1356	1.9157	0.057471	3.2	3
Sm	2.391	0.09631	2.7294	0.054588	2.49	4
Dy	2.532	0.09076	2.1026	0.21026	2.3	3
U	2.587	0.1341	2.9774	0.29774	2.39	3
As	2.781	0.1726	1.9637	0.039274	2.5	4
Ta	5.031	0.3578	0.7945	0.1589	0.9	3
Th	8.009	0.2908	8.3971	0.83971	9.14	3
Nd	13.38	1.163	13.2003	1.32003	10.6	7
La	13.8	0.4874	16.1252	0.322504	14.7	10
Cr	18.74	0.9639	30.5777	3.05777	37	3
Ce	28.04	1.271	31.7841	0.635682	29.7	4
Mn	33.21	1.168	55.869	1.67607	43	5
Zn	33.3	5.144	42.9624	3.007368	18	4
Na	168	6.239	256.2626	12.81313	54	10
Co	255.8	13.97	210.3412	2.103412	73	3
Ni	559.3	90.74	578.4052	115.68104	640	4
K	691.5	51.05	894.5101	178.90202	175	4

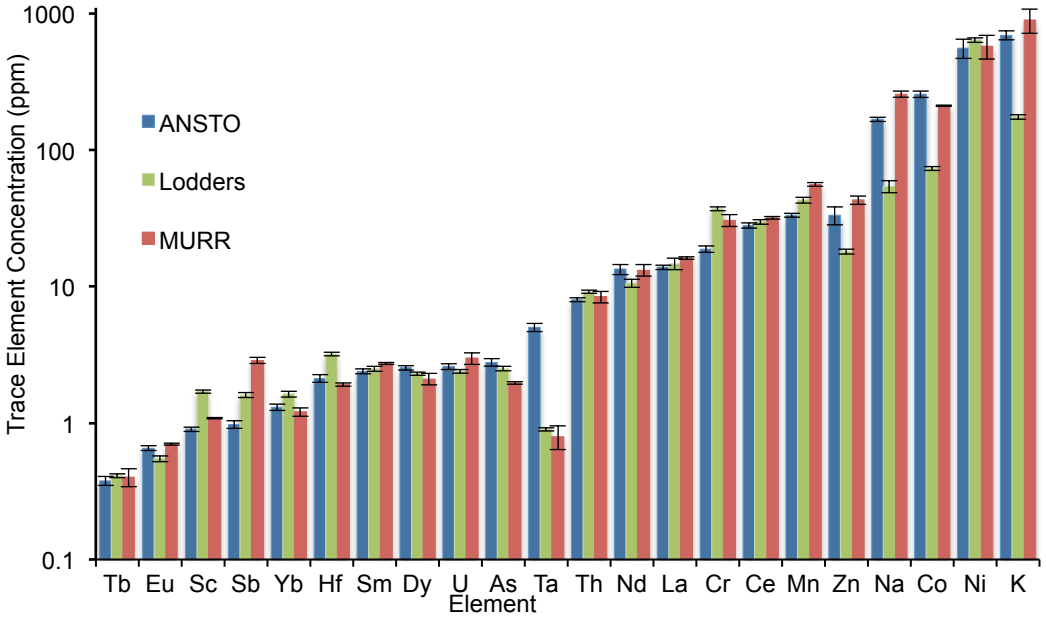

Figure 3.5 Plot comparing NAA trace element analysis of pyrite from Victoria Mine.

Table 3.10 Results of paired t-tests comparing NAA trace element concentration data for pyrite from Victoria Mine (G33033).

	ANSTO x MURR	ANSTO x Lodders	MURR x Lodders
t-experimental	1.40	1.29	1.38
df	21	21	21
t-critical	2.08	2.08	2.08

3.4 Conclusions

Trace element data for 30 different pyrite samples originating from a range of different geological regions was acquired using relative comparator NAA and k_0-NAA. Results from the two methods have been critically compared. Given the good overall correlation between the majority of elemental analyses and the high correlation between the Navajun sample analyses, it is likely that a large part of the variation between the analyses is due to heterogeneity within the samples. There do appear to be systematic differences between the k_0 (ANSTO) and relative comparator (MURR) NAA determinations of Al Na and Ti. It is likely that these inconsistencies are a result of contamination during the sample preparation process. By analysing a large set of different samples systematic errors are more easily identified than in smaller sample sets. It is also suggested that materials such as high purity quartz be prepared for analysis in an identical fashion to the samples in order to provide a background level of elemental concentrations.

Given that the two methods of analysis have been shown to be statistically indistinguishable for the majority of elements, it is not unreasonable to combine the two data sets to yield a single set of trace elemental data for all 40 pyrite samples. Presented in Chapter 4 is the analysis of this data where we will attempt to correlate trace impurity concentrations to reactivity of the samples.

Chapter 4.

Analysis of trace element composition and semiconducting type.

4.1 Introduction

Natural pyrite specimens are never purely FeS_2, they always contain other elements in minor (a few %) or trace (<1%) quantities [3]. Common impurities in pyrite include As, Co, Cu and Ni [99].

The impurities in pyrite are likely to occur as either small inclusions of other minerals or as lattice substitutions. Lattice substitutions are categorised as being either stoichiometric or non-stoichiometric. Stoichiometric substitution describes when the elemental or molecular ions that replace Fe^{2+} or S_2^{2-} have a similar charge and ionic radius. Common examples of stoichiometric substitutions in pyrite include Co^{2+} and Ni^{2+} for Fe^{2+} and Se and Te for S in the S_2^{2-} ion [3, 100]. Non-stoichiometric inclusions are said to occur when ions of differing charge and ionic radii substitute for the native elements. The most prevalent example of nonstoichiometric substitution is the substitution of S with As ion the S_2^{2-} ion producing AsS^{2-} and As_2^{2-} for substitution of 1 and 2 S atoms respectively [3, 100].

The reason for the interest in the trace element composition of pyrite samples is due to pyrite's semiconducting properties. Pyrite, as with other semiconductors can have its electrical properties altered by the introduction of other elements or dopants into the crystal lattice. These dopants effectively alter the concentration of charge carriers in the lattice. The dopants can either donate electrons (negative charge carriers) or they can donate holes (positive charge carriers) into the crystal lattice. Materials with an abundance of positive charge carriers are known as p-type semiconductors and those with an abundance of negative charge carriers are known as n-type. Previous studies have shown that the semiconducting properties of pyrite are linked to its trace elemental composition [3, 28, 29, 101].

Semiconductor type can be assessed in a number of ways, the most straightforward method utilises the Seebeck or thermoelectric effect to determine overall semiconductor type (i.e. p or n). The thermoelectric effect can be explained as such; the heating of an area of a semiconducting material will cause the conduction band energy in that area to increase (the effective density of states increases with increasing temperature), causing

charge carriers in the conduction band of the “hot“ area to move to a cooler, lower energy area. This effectively creates a current that can be measured and will vary in sign depending on the most abundant charge carrier [102]. The advantages of measuring semiconductor type this way is that it is simple, cheap and requires only that the sample in question had clean contact points for the probe. This method can also be used for more detailed measurements of electrical properties of minerals as demonstrated in Laird *et al.* [103].

The importance of the electrical or semiconducting properties of pyrite lie in the fact that pyrite is proposed to oxidise through an electrochemical process. During this process, electrons are transported through the lattice from anodic sites to cathodic sites [31, 35]. If the electron transport was promoted or inhibited by alterations in the electronic structure of the pyrite sample, it is hypothesised that this would alter the reactivity of said sample.

In pyrite, notable electron donating elements are Co and Ni, while the presence of hole donating impurities such as As and Sb are known to form p-type pyrites. Abratis *et al.* [3] summarises the observed trends in pyrites electrical variation from the literature as follows; p-type pyrites often have a large concentration of As, a S/Fe ratio >2 and form in low temperature deposits; n-type pyrites have large concentrations of Co and Ni, have a S/Fe reation <2 and form in high temperature deposits [3]. Work by Savage *et al.* [101] on synthetic pyrites found that increases in the concentration of Co and As had strong correlation with increases in charge carrier concentration, Ni was found to have a less significant impact. Schieck *et al.* [104] propose that Si, Cu and Al are important electron donors and As, P and Sb were important hole donors. They also found that doping pyrite with Zn had little effect on semiconducting properties despite its high concentration in the mineral. Therefore, Co, Cu and Ni were identified as the most important electron donors and As and Sb as the most important hole donors. It should be noted that Al was omitted from this study due to its likely presence as a clay inclusion and Si was not measured in concentrations above the limits of quantitation for NAA, which are particularly high.

Chapter 3 presented the process to acquire and validate the trace element data for the 40 pyrite samples. The data from the ANSTO and MURR analyses and were found to correlate well with each other, the majority of elemental analyses being indistinguishable at the 0.05 confidence level. Many of the inconsistencies reported were attributed to inhomogeneities within the samples themselves and to concentrations reported close to and below the LOD. As a result of these conclusions the data obtained from ANSTO was used for further analysis due to the larger number of elements analysed (67 compared to MURR's 32). Where ANSTO data was not available for certain samples MURR data was used. This chapter analyses this trace element data for any correlation it may have to the measured reactivity of the pyrite samples. The semiconducting type of the pyrite samples are also assessed in light of their trace element composition.

4.2 Materials and methods

4.2.1 Neutron activation analysis

Table 4.1 provides a summary of the elements analysed by each facility.

4.2.2 Semiconductor type

The "hot probe" method for determining semiconductor type was used to determine the overall semiconductor type of the pyrite samples. The positive probe of a digital multimeter set to measure DC voltage (Fluke U.S.A) was heated on a hotplate for 2-3 minutes. The multimeter probes were subsequently contacted on to the sample 1-2cm apart. The sign of the displayed current was noted, with a positive sign indicating n-type and a negative sign indicating p-type. The measurement was repeated at several locations on the sample so that any inhomogeneity of semiconductor type through the sample could be observed. No special preparation of the pyrite samples were performed other than ensuring a clean contact surface for the probes.

Table 4.1 Summary of elements analysed by each NAA facility.

	ANSTO	MURR		ANSTO	MURR
Ag	✓		Mo	✓	
Al	✓	✓	Na	✓	✓
Ar	✓		Nb	✓	
As	✓	✓	Nd	✓	✓
Au	✓		Ni	✓	✓
Ba	✓	✓	Os	✓	
Br	✓		Pd	✓	
Ca	✓		Pr	✓	
Cd	✓		Pt	✓	
Ce	✓	✓	Rb	✓	✓
Cl	✓		Re	✓	
Co	✓	✓	Rh	✓	
Cr	✓	✓	Ru	✓	
Cs	✓	✓	Sb	✓	✓
Cu	✓		Sc	✓	✓
Dy	✓	✓	Se	✓	
Er	✓		Si	✓	
Eu	✓	✓	Sm	✓	✓
F	✓		Sn	✓	
Fe	✓	✓	Sr	✓	✓
Ga	✓		Ta	✓	✓
Gd	✓		Tb	✓	✓
Ge	✓		Te	✓	
Hf	✓	✓	Th	✓	✓
Hg	✓		Ti	✓	✓
Ho	✓		Tm	✓	
I	✓		U	✓	✓
In	✓		V	✓	✓
Ir	✓		W	✓	
K	✓	✓	Y	✓	
La	✓	✓	Yb	✓	✓
Lu	✓	✓	Zn	✓	✓
Mg	✓		Zr	✓	✓
Mn	✓	✓			

4.2.3 Data treatment

For NAA data only, concentration data >3 times the relevant LOD was used. As discussed in the previous chapter, for data derived from the MURR analyses a 250ppm background was subtracted from the Al data, a 40ppm background from the Na data and the Ti data was disregarded altogether. The relative abundance units of ppm were converted to mol.kg^{-1} using the appropriate molecular masses as these units are more relevant when discussing chemical processes and effects.

The resulting data set is presented in Table 4.2. The raw data from both analyses can be found in Appendix A including their respective limits of detection and uncertainties. Uncertainty values were not included in Table 4.2

For assessing correlation between data sets Equation 4.1 was used to generate a correlation coefficient:

$$Correl(X,Y) = \frac{\sum(x-\bar{x})(y-\bar{y})}{\sqrt{\sum(x-\bar{x})^2(y-\bar{y})^2}}$$

Equation 4.1 Formula for calculating the correlation coefficient between two data sets. *(X and Y) where $\bar{x}$=mean of data set X.*

As the strength of the correlation between the sample sets increases the correlation coefficient tends toward 1.

Initial analysis saw the Pacific Ocean sample (G30334) and the Weedon Mine sample (G32706) having a large influence on the analysis due to their large proportion of impurities. They were subsequently removed from the final analyses, this is further explained below.

4.3 Results and discussion

4.3.1 Neutron activation analysis results

The data from the neutron activation analyse from ANSTO and MURR were treated as previously described, the resulting data is presented in Table 4.2.

Table 4.2 Trace elemental data from NAA analysis of 40 pyrite samples.

	[Ag] mmol.kg^{-1}	[Al] mmol.kg^{-1}	[As] mmol.kg^{-1}	[Au] µmol.kg^{-1}	[Ba] mmol.kg^{-1}	[Br] mmol.kg^{-1}	[Ca] mmol.kg^{-1}
G11641	-	15.121	0.075	-	-	-	-
G16011	-	-	8.385	-	-	-	-
G16079	-	-	-	-	-	-	-
G17012	-	-	3.161	-	-	-	-
G18915	-	0.225	0.038	-	-	-	-
G20974	-	104.775	3.369	-	0.112	-	4.943
G29969	-	-	4.334	-	-	-	-
G29982	-	47.477	0.025	-	-	-	11.093
G30334	-	100.764	2.482	-	4.416	-	-
G32406	-	4.585	7.836	-	-	-	-
G32407	0.475	0.324	0.243	-	-	0.052	-
G32408	-	75.886	0.114	-	-	-	-
G32409	-	12.742	0.267	-	-	-	-
G32410	0.599	0.452	0.239	-	-	0.047	-
G32411	-	72.753	2.715	-	0.272	-	142.622
G32412	-	4.173	7.704	-	-	-	7.575
G32413	-	21.830	0.061	-	-	-	3.715
G32414	-	8.613	0.036	0.496	-	-	12.623
G32415	-	6.556	0.302	-	0.045	-	8.678
G32416	-	8.306	2.792	0.212	-	-	-
G32417	-	39.360	0.156	-	-	-	40.346
G32418	-	0.493	3.509	-	-	-	81.017
G32419	0.616	1.097	5.291	-	-	-	-
G32420	-	4.407	-	-	-	-	-
G32421	-	1.242	0.022	0.098	-	-	-
G32422	0.128	0.233	31.246	-	-	-	-
G32423	-	27.474	0.959	-	0.131	-	-
G32424	-	15.210	0.066	-	-	-	23.484
G32425	-	8.624	-	-	-	-	-
G32426	1.175	0.223	43.245	-	-	-	-
G32427	-	-	7.150	-	-	-	-
G32428	1.441	4.918	127.480	-	-	-	7.323
G32429	0.046	0.678	0.714	-	-	-	-
G32430	-	-	-	-	-	-	-
G32706	-	687.904	0.612	-	13.039	-	-
G33033	-	245.538	0.037	-	0.148	-	32.362
G33797	-	6.175	0.115	-	-	-	10.128
G33823	-	-	0.076	-	-	-	-
G6876	-	0.099	1.524	-	-	-	-
G9699	-	25.662	7.180	0.669	-	-	-
n	7	33	36	4	7	2	13
Minimum	0.046	0.099	0.022	0.098	0.045	0.047	3.715
Maximum	1.441	687.904	127.480	0.669	13.039	0.052	142.622
Range	1.394	687.805	127.458	0.570	12.993	0.005	138.907
Median	0.599	8.306	0.837	0.354	0.148	0.050	11.093

	[Cd] mmol.kg^{-1}	[Ce] mmol.kg^{-1}	[Cl] mmol.kg^{-1}	[Co] mmol.kg^{-1}	[Cr] mmol.kg^{-1}	[Cs] mmol.kg^{-1}	[Cu] mmol.kg^{-1}
G11641	-	-	0.455	25.215	1.081	-	6.436
G16011	-	0.025	-	21.773	0.047	-	-
G16079	-	-	-	0.864	0.059	-	-
G17012	-	0.164	-	9.937	0.045	-	-
G18915	-	-	3.427	41.827	-	-	-
G20974	-	0.015	1.919	0.066	0.257	-	1.778
G29969	-	-	-	2.757	0.047	-	-
G29982	-	0.029	-	0.110	-	-	-
G30334	-	-	-	17.116	-	-	-
G32406	-	-	0.286	5.472	-	-	-
G32407	0.825	-	5.732	0.318	-	-	0.466
G32408	-	0.167	-	16.531	0.114	-	-
G32409	-	-	1.170	0.045	-	-	-
G32410	-	-	4.863	0.253	-	-	1.350
G32411	-	0.007	3.131	0.017	-	-	0.251
G32412	-	-	-	0.007	-	-	-
G32413	-	0.005	0.224	0.101	-	-	-
G32414	-	-	-	0.044	-	-	-
G32415	-	0.086	0.138	3.591	-	-	0.365
G32416	-	-	0.409	0.019	-	-	0.116
G32417	-	0.023	-	0.614	-	-	2.052
G32418	-	-	0.609	0.098	-	-	24.533
G32419	-	-	0.376	0.352	-	-	-
G32420	-	-	0.255	0.011	-	-	-
G32421	-	-	0.425	0.182	-	-	1.000
G32422	-	-	-	0.092	-	-	4.743
G32423	-	0.041	-	0.219	-	0.013	0.168
G32424	-	-	0.534	0.053	-	-	0.265
G32425	-	-	-	0.992	-	-	-
G32426	-	-	0.296	0.078	-	-	4.310
G32427	-	0.029	-	0.043	0.060	-	-
G32428	-	-	-	0.095	-	-	6.205
G32429	-	0.083	5.024	0.129	-	-	3.300
G32430	-	-	-	0.377	0.075	-	-
G32706	-	-	-	12.988	0.040	-	-
G33033	-	0.200	-	4.341	0.360	-	-
G33797	-	-	1.600	0.081	-	-	0.278
G33823	-	-	-	0.027	0.054	-	-
G6876	-	-	0.128	1.047	-	-	-
G9699	-	-	10.586	35.769	-	-	1.720
n	1	13	21	40	12	1	18
Minimum	0.825	0.005	0.128	0.007	0.040	0.013	0.116
Maximum	0.825	0.200	10.586	41.827	1.081	0.013	24.533
Range	0.000	0.195	10.458	41.820	1.041	0.000	24.417
Median	0.825	0.029	0.534	0.236	0.059	0.013	1.535

	[Dy] $\mu mol.kg^{-1}$	[Eu] $\mu mol.kg^{-1}$	[Fe] $mol.kg^{-1}$	[Ga] $mmol.kg^{-1}$	[Hf] $mmol.kg^{-1}$	[Hg] $mmol.kg^{-1}$	[In] $\mu mol.kg^{-1}$
G11641	-	-	8.081	-	-	-	-
G16011	-	-	7.771	-	-	-	-
G16079	-	-	7.754	-	-	-	-
G17012	15.234	1.295	7.532	-	-	-	-
G18915	-	-	8.167	-	-	-	-
G20974	0.866	-	8.019	0.034	-	-	-
G29969	-	0.222	7.585	-	-	-	-
G29982	0.782	0.223	7.524	-	-	-	-
G30334	-	-	4.299	-	-	-	-
G32406	0.519	-	7.933	-	-	0.076	-
G32407	-	-	7.788	-	-	-	2.405
G32408	12.847	3.168	7.988	-	0.028	-	-
G32409	-	-	8.080	-	-	-	-
G32410	-	-	7.677	-	-	-	0.562
G32411	-	-	7.772	-	-	-	-
G32412	-	-	8.037	-	-	-	-
G32413	0.361	-	8.142	-	-	-	-
G32414	-	-	7.963	-	-	-	-
G32415	6.646	0.852	8.430	-	0.024	-	-
G32416	0.626	-	8.011	-	-	-	0.215
G32417	-	0.573	8.164	-	-	-	-
G32418	3.743	0.842	7.968	0.184	-	-	0.237
G32419	-	-	8.242	-	-	-	17.053
G32420	-	-	8.208	-	-	-	-
G32421	-	-	7.947	-	-	-	-
G32422	-	-	8.362	-	-	-	17.968
G32423	1.206	0.691	7.963	-	-	0.021	-
G32424	0.744	-	8.384	-	-	-	1.903
G32425	-	-	8.282	-	-	-	182.288
G32426	-	-	8.019	0.209	-	-	0.444
G32427	-	1.545	7.837	-	-	-	-
G32428	-	-	7.881	-	-	-	5.429
G32429	0.907	0.399	8.497	0.191	-	-	0.353
G32430	-	-	8.059	-	-	-	-
G32706	-	0.701	6.908	-	-	-	-
G33033	15.582	4.310	7.793	-	0.012	-	-
G33797	-	-	7.988	-	-	-	0.624
G33823	-	-	7.623	-	-	-	-
G6876	-	-	7.600	-	-	-	-
G9699	-	-	8.173	-	-	-	0.973
n	13	12	40	4	3	2	13
Minimum	0.361	0.222	4.299	0.034	0.012	0.021	0.215
Maximum	15.582	4.310	8.497	0.209	0.028	0.076	182.288
Range	15.220	4.088	4.198	0.175	0.016	0.056	182.073
Median	0.907	0.772	7.978	0.188	0.024	0.048	0.973

	[K] mmol.kg^{-1}	[La] µmol.kg^{-1}	[Lu] µmol.kg^{-1}	[Mg] mmol.kg^{-1}	[Mn] mmol.kg^{-1}	[Mo] mmol.kg^{-1}	[Na] mmol.kg^{-1}
G11641	-	-	-	-	1.603	-	-
G16011	-	16.285	-	-	0.257	-	3.396
G16079	-	-	-	-	1.194	-	2.838
G17012	-	79.369	-	-	0.077	-	4.022
G18915	-	-	-	35.100	0.037	-	7.238
G20974	23.101	10.165	-	6.920	0.140	0.208	9.961
G29969	-	-	0.919	-	2.684	-	3.961
G29982	7.144	13.563	-	5.464	0.084	-	2.315
G30334	-	-	-	-	4.277	-	51.674
G32406	3.079	3.168	-	-	0.013	-	0.578
G32407	-	-	-	-	5.892	-	1.089
G32408	-	93.515	0.843	-	2.193	-	4.817
G32409	-	-	-	-	0.032	0.600	2.690
G32410	-	4.262	-	-	5.628	-	1.064
G32411	13.492	3.053	-	36.137	0.254	5.091	9.709
G32412	1.790	1.367	-	4.604	0.023	1.945	0.188
G32413	5.617	2.540	-	4.337	0.130	-	0.288
G32414	2.386	0.559	-	-	5.590	-	1.041
G32415	5.542	38.767	-	4.575	0.009	0.080	0.324
G32416	-	1.824	-	17.396	0.243	-	0.365
G32417	11.850	7.394	-	-	21.260	-	3.742
G32418	-	-	-	19.272	0.178	0.522	0.626
G32419	-	-	-	19.115	0.360	-	0.414
G32420	-	0.391	-	-	0.068	-	1.032
G32421	-	0.517	-	-	0.025	-	0.202
G32422	-	-	-	-	0.023	-	0.279
G32423	-	24.621	-	-	0.389	-	0.538
G32424	7.358	3.939	-	-	2.707	-	0.397
G32425	3.384	1.213	-	-	13.264	-	-
G32426	-	-	-	-	0.042	-	0.234
G32427	30.876	18.300	-	-	0.752	-	2.083
G32428	-	-	-	-	0.635	-	0.406
G32429	-	44.807	-	24.629	0.070	-	2.896
G32430	-	-	-	-	0.076	-	1.932
G32706	187.538	-	-	-	3.906	-	60.938
G33033	17.686	99.348	-	71.672	0.604	-	7.308
G33797	-	-	-	23.440	0.871	-	0.506
G33823	-	-	-	-	0.255	-	4.384
G6876	-	-	-	-	0.015	-	0.382
G9699	-	-	-	28.072	0.195	-	11.031
n	14	22	2	14	40	6	38
Minimum	1.790	0.391	0.843	4.337	0.009	0.080	0.188
Maximum	187.538	99.348	0.919	71.672	21.260	5.091	60.938
Range	185.748	98.957	0.076	67.336	21.251	5.011	60.749
Median	7.251	5.828	0.881	19.194	0.254	0.561	1.511

	[Nd] mmol.kg^{-1}	[Ni] mmol.kg^{-1}	[Rb] mmol.kg^{-1}	[Ru] mmol.kg^{-1}	[Sb] µmol.kg^{-1}	[Sc] µmol.kg^{-1}	[Se] mmol.kg^{-1}
G11641	-	-	-	-	26.027	-	-
G16011	-	-	-	-	13.277	-	-
G16079	-	-	-	-	2.221	1.762	-
G17012	-	5.314	-	-	-	5.984	-
G18915	-	10.095	-	-	-	-	0.534
G20974	-	-	1.277	-	281.209	12.948	0.522
G29969	-	8.977	-	-	74.442	6.028	-
G29982	-	-	-	-	-	4.914	-
G30334	-	-	-	-	276.444	3.212	-
G32406	-	-	-	-	7.466	-	0.418
G32407	-	-	-	-	-	-	-
G32408	-	3.392	-	-	4.604	20.622	-
G32409	-	-	-	-	38.436	1.327	0.137
G32410	-	-	-	-	13.420	-	-
G32411	-	-	0.784	-	105.700	6.922	0.087
G32412	-	-	-	-	249.754	-	0.097
G32413	-	4.549	0.739	-	-	4.576	0.467
G32414	-	-	-	-	3.649	6.371	0.190
G32415	0.038	4.430	-	2.081	-	2.745	0.077
G32416	-	-	-	-	17.888	2.589	-
G32417	-	-	0.946	-	5.039	11.725	-
G32418	0.355	-	-	-	99.129	3.826	0.577
G32419	-	-	-	-	8.238	-	-
G32420	-	-	-	-	-	2.883	-
G32421	-	-	0.880	-	2.939	-	0.209
G32422	-	-	-	-	237.024	-	0.080
G32423	-	-	-	-	283.262	15.259	-
G32424	-	-	-	-	552.645	2.683	-
G32425	-	-	0.805	-	-	-	-
G32426	-	-	0.838	-	163.847	-	-
G32427	-	-	-	-	40.797	10.094	-
G32428	-	-	-	-	300.427	-	-
G32429	-	-	-	-	-	3.085	0.362
G32430	-	-	-	-	2.750	-	-
G32706	-	-	-	-	8.561	9.734	-
G33033	0.093	-	-	-	8.027	20.029	0.302
G33797	-	-	0.689	-	-	-	0.173
G33823	-	-	-	-	10.215	1.045	-
G6876	-	-	-	-	-	-	-
G9699	-	50.142	-	-	34.001	4.342	0.909
n	3	7	8	1	29	24	16
Minimum	0.038	3.392	0.689	2.081	2.221	1.045	0.077
Maximum	0.355	50.142	1.277	2.081	552.645	20.622	0.909
Range	0.317	46.750	0.588	0.000	550.424	19.577	0.832
Median	0.093	5.314	0.822	2.081	26.027	4.745	0.256

	[Sm] $\mu mol.kg^{-1}$	[Sn] $mmol.kg^{-1}$	[Sr] $mmol.kg^{-1}$	[Ta] $\mu mol.kg^{-1}$	[Tb] $\mu mol.kg^{-1}$	[Th] $\mu mol.kg^{-1}$	[Ti] $mmol.kg^{-1}$
G11641	-	-	-	-	-	-	-
G16011	1.372	-	-	-	-	-	-
G16079	-	-	-	-	-	-	-
G17012	8.292	-	-	-	-	-	-
G18915	-	-	-	-	-	-	-
G20974	1.111	-	-	-	-	2.517	5.896
G29969	-	-	-	-	-	-	-
G29982	1.605	-	-	-	-	3.546	4.671
G30334	-	-	-	-	-	-	-
G32406	-	-	-	-	-	-	1.155
G32407	-	-	-	-	-	-	-
G32408	13.840	-	-	1.997	2.417	26.429	-
G32409	-	-	-	-	-	-	-
G32410	-	-	-	-	-	-	-
G32411	-	-	2.002	-	-	-	2.478
G32412	-	-	-	-	-	-	-
G32413	-	-	-	-	-	-	1.468
G32414	-	-	-	-	-	-	-
G32415	5.932	-	-	-	-	17.183	26.574
G32416	-	-	-	-	-	-	2.580
G32417	2.420	-	-	-	-	-	-
G32418	3.356	-	-	-	-	3.562	-
G32419	-	-	-	-	-	-	-
G32420	-	-	-	-	-	-	-
G32421	-	-	-	-	-	-	-
G32422	-	2.451	-	-	-	-	-
G32423	2.868	-	-	-	-	-	20.202
G32424	1.016	-	-	-	-	3.249	0.944
G32425	-	-	-	-	-	-	-
G32426	-	-	-	-	-	-	-
G32427	3.938	-	-	-	-	1.449	-
G32428	-	-	-	-	-	-	-
G32429	2.485	-	-	-	-	-	0.573
G32430	-	-	-	-	-	-	-
G32706	1.192	-	-	-	-	-	-
G33033	15.902	-	-	27.804	-	34.516	47.360
G33797	-	-	-	-	-	-	-
G33823	-	-	-	-	-	-	-
G6876	-	-	-	-	-	-	-
G9699	-	-	-	-	-	-	-
n	14	1	1	2	1	8	11
Minimum	1.016	2.451	2.002	1.997	2.417	1.449	0.573
Maximum	15.902	2.451	2.002	27.804	2.417	34.516	47.360
Range	14.886	0.000	0.000	25.806	0.000	33.067	46.788
Median	2.677	2.451	2.002	14.900	2.417	3.554	2.580

	[Tm] mmol.kg^{-1}	[U] µmol.kg^{-1}	[V] µmol.kg^{-1}	[W] mmol.kg^{-1}	[Yb] µmol.kg^{-1}	[Zn] mmol.kg-^{1}
G11641	-	-	499.200	-	-	-
G16011	-	-	-	-	-	3.186
G16079	-	-	307.555	-	-	0.441
G17012	-	-	-	-	-	-
G18915	-	-	-	-	-	-
G20974	-	3.074	305.645	-	-	-
G29969	-	-	-	-	-	-
G29982	-	-	53.002	-	-	-
G30334	-	-	1792.395	-	-	3949.583
G32406	-	-	5.734	-	-	-
G32407	-	-	45.405	-	-	95.598
G32408	-	-	-	-	6.160	-
G32409	-	-	9.346	-	-	-
G32410	-	-	41.989	-	-	1.385
G32411	-	3.570	121.532	-	-	-
G32412	-	-	4.052	-	-	-
G32413	-	-	47.937	-	-	0.507
G32414	-	-	14.850	-	-	-
G32415	-	8.293	16.770	-	4.408	-
G32416	-	-	36.571	0.039	-	0.239
G32417	-	-	37.769	-	-	-
G32418	-	42.558	922.823	8.268	-	-
G32419	-	-	8.773	-	-	5.430
G32420	-	-	9.419	-	-	-
G32421	-	-	0.662	-	-	-
G32422	-	-	-	-	-	8.858
G32423	-	-	156.042	0.047	-	0.253
G32424	-	-	5.361	-	-	14.970
G32425	-	-	-	-	-	-
G32426	-	-	32.056	-	-	0.223
G32427	-	-	-	-	-	17.608
G32428	0.253	-	26.874	-	-	17.857
G32429	-	-	10.913	0.021	-	1.566
G32430	-	-	-	-	-	-
G32706	-	-	383.952	-	-	57.454
G33033	-	10.868	164.915	-	7.530	0.509
G33797	-	-	14.579	-	-	4.302
G33823	-	-	-	-	-	-
G6876	-	-	0.580	-	-	-
G9699	-	-	36.336	-	-	-
n	1	5	30	4	3	18
Minimum	0.253	3.074	0.580	0.021	4.408	0.223
Maximum	0.253	42.558	1792.395	8.268	7.530	3949.583
Range	0.000	39.484	1791.815	8.247	3.122	3949.360
Median	0.253	8.293	36.454	0.043	6.160	3.744

4.3.2 Trace element correlations

Table 4.2 summarises the trace element data collected for each pyrite sample, incorporating the analyses done at MURR where required.

Of the 67 elements analysed by NAA, 48 were found in at least one sample, at a concentration greater than or equal to three times the LOD.

By first looking at the Fe concentrations of all the samples and considering that the ideal stoichiometry of pyrite would yield a molal concentration of Fe of 8.335mol.kg^{-1}, it can immediately be seen that the majority of samples lie below this value. This is not unexpected as it is common for substitutions in pyrite to occur up to a few weight percent [3]. However, there are two samples that show a considerably smaller iron concentration; the Pacific Ocean sample (G30334) and the Weedon Mine sample (G32706) have iron concentrations of 4.299 and 6.908mol.kg^{-1} respectively, this translates to a decrease in iron concentration of 48.4%w/w and 17.1%w/w from ideal stoichiometry. It is not surprising that the Pacific Ocean sample (G30334) has such a high level of impurities due to its conditions of formation. Minerals formed at hydrothermal vents often include a mixture of sulfide minerals [105]. By analysing the impurity data for this sample it can be seen that it has a large concentration of Zn (3.95mol.kg^{-1}). The Weedon Mine sample (G32706) has the largest measured Al, Ba and K impurites of all samples (0.69, 0.013 and 0.19mol.kg^{-1} respectively) and it is hypothesised that the sample contained a large proportion of potassium bearing alumino silicates. Due to their large percentage of impurities these samples were excluded from further analysis so that they would not skew results.

Figure 4.1 depicts the sum concentration of all detected impurities in the samples (apart from Pacific Ocean and Weedon Mine for reasons discussed previously). The figure also displays the average concentration of different impurities found in each sample calculated by dividing total concentration of all impurities by the number of different impurities detected. The two data sets correlate well with each other suggesting that as the total concentration of impurities increases, the number of different impurities does not generally increase but their individual concentrations do.

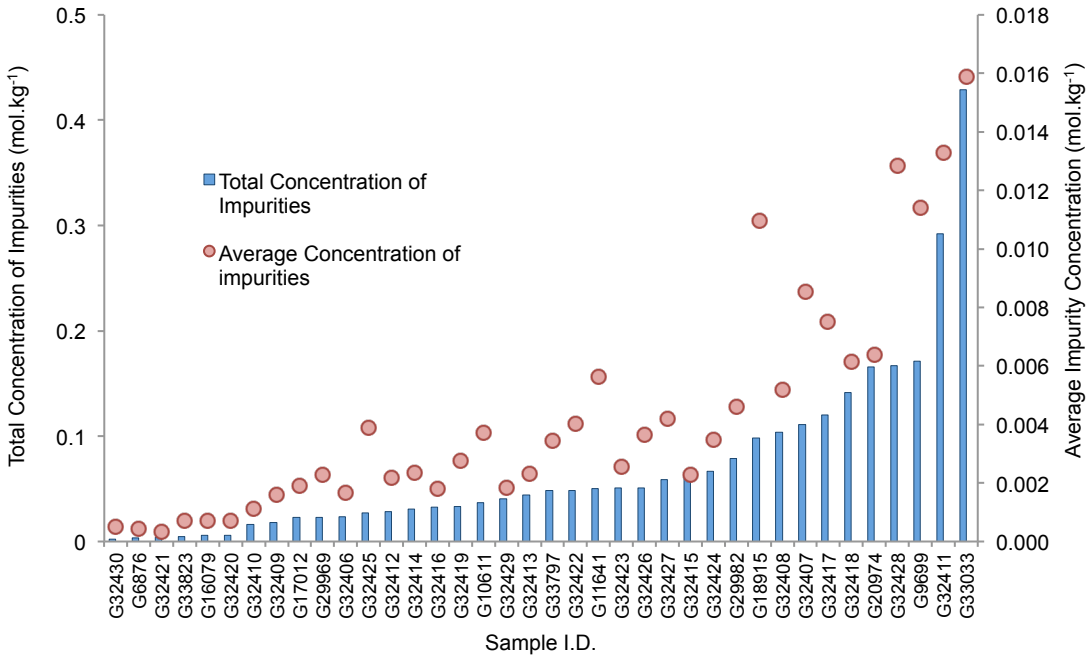

Figure 4.1 Total concentration of impurities measured by NAA.
Compared to the average concentration of different impurities measured for each sample.

The correlation coefficients between each trace element and the rate constants as measured in Chapter 2 (a measure of reactivity) are displayed in Table 4.3. Also shown are the correlation coefficients between reactivity and elemental concentrations aggregated according to several periodic groupings, this is to see if any correlation exists between reactivity and elements which may lattice substitute in similar ways. The correlation coefficients are calculated using both the unaltered data and the $\log_{10}$ of the data sets. The correlation coefficients derived from the unaltered data is considered first; there are several elements which show high correlation coefficients; Ga, Hf, Rb and Yb all have coefficients greater than 0.8, Al, K, Na, Nd, Sc, and U have coefficients between 0.39 and 0.53 indicating a medium to weak correlation. It can also be seen from Table 4.3 that Ga, Hf, Nd and Yb only have 3 or 4 data points, while these elements appear to have a strong correlation to reactivity the small number of points are not sufficient to draw significant conclusions. 1st group metals, poor metals (As and Sb) and total impurities all show medium–weak correlations with reactivity. The remaining elements or groups show poor correlations.

Table 4.3 Correlation coefficients of reactivity and trace element concentration.

Element	n	Correlation coefficient	Correlation coefficient (log vs. log)
Ag	7	0.086	0.449
Al	31	0.527	0.319
As	34	-0.158	-0.101
Au	4	0.336	0.104
Ba	5	-0.057	0.283
Ca	13	-0.048	0.025
Ce	13	-0.193	-0.266
Cl	21	0.049	0.064
Co	38	-0.056	0.105
Cr	11	0.229	0.489
Cu	18	-0.201	-0.067
Dy	13	-0.131	-0.188
Eu	11	0.119	-0.249
Fe	38	-0.184	-0.179
Ga	4	-0.964	-0.951
Hf	3	-0.921	-0.931
In	13	-0.070	0.118
K	13	0.393	0.437
La	22	0.006	0.118
Mg	14	0.028	-0.067
Mn	38	0.060	0.179
Mo	6	-0.138	-0.150
Na	36	0.436	0.332
Nd	3	-0.449	-0.266
Ni	7	0.240	0.322
Rb	8	0.954	0.909
Sb	27	0.125	0.060
Sc	22	0.399	0.317
Se	16	0.273	0.291
Sm	13	-0.112	-0.350
Th	8	-0.006	0.114
Ti	11	0.204	0.441
U	5	-0.535	-0.672
V	28	0.113	0.247
W	4	-0.443	-0.382
Yb	3	0.897	0.888
Zn	16	0.021	-0.225
Σ 1^{st} Group Metals	37	0.429	0.212
Σ 2^{nd} Group Metals	19	0.016	-0.066
Σ 1^{st} and 2^{nd} Group Metals	37	0.182	0.068
Σ 1^{st} Row Transition Metals (excl. Fe)	38	0.073	0.092
Σ 2^{nd} Row Transition Metals	13	-0.122	0.044
Σ 3^{rd} Row Transition Metals	11	-0.248	-0.030
Σ Total Transition Metals (excl. Fe)	38	0.066	0.081
Σ Poor Metals (Al, Ga, In, Sn)	31	0.521	0.272
Σ Halides	21	0.050	0.064
Σ Metalloids (As, Sb)	36	-0.157	-0.069
Σ Lanthanoids	25	-0.090	-0.014
Σ Actanoids	9	-0.168	0.13
Σ Total (excl. Fe)	38	0.327	0.156

Scatter plots of the elements and element groups with the greatest correlation coefficients (Al, K, Na, Rb, Sc, U, 1st group metals and poor metals) can be seen in Figure 4.2. Figure 4.2 shows that most of the correlations are influenced by single point and in many cases it is the high reactivity sample from Sparta (G20974) which appears out on the right hand side of the plots. This feature is also present from other sources, for example, the K plot has a point which is a significant distance from the majority of the other points. While these points are not necessarily outliers, their distance from the majority of points (or mean) give them great weight in correlation and regression calculations and, therefore, have the ability to skew results. To evaluate these points, it is necessary to reduce the weight that they carry in these correlations or regressions. The simplest way to do this without removing data or implementing complex weighting equations is to calculate the $\log_{10}$ of the data and use these values in further calculations [106].

The correlation coefficients resulting from the $\log_{10}$ data can be seen in the last column of Table 4.3. The treatment has affected each data set to a different extent; some correlation coefficients have become stronger such as Ag and K, while some have become weaker such as Na and Al. To visualise these changes, the same 8 elements and elemental groups as displayed in Figure 4.2 are plotted as log/log plots in Figure 4.3. While the correlation coefficient for Al has decreased, Figure 4.3 reveals that the Al data may include two distinct data sets both with positive trends. The strength of the correlation for the K plot is maintained and the outlying point remains in its position, interestingly by removing this point the correlation coefficient almost doubles from 0.437 to 0.864. For the log/log plot of Na we see that the data is quite normally distributed with no apparent correlation. The log/log plot for Rb maintains a strong correlation, however, the relatively small data set (n=8) creates uncertainty regarding the correlation coefficient. Whilst the Sc correlation coefficient remained at a similar value, the plot reveals no strong correlation. The negative correlation observed for U is enhanced in the log/log plot, however, the certainty of the correlation suffers from having relatively few data points (n=5). The correlation coefficient for the sum of 1st group and sum of poor metals both decreased by approximately half. The

sum of 1st group metals appears to be normally distributed while there may be two distinct correlations present for the sum of poor metals, which is similar to the results for Al.

From this analysis it can be seen that there is a correlation between reactivity and the inclusion of 1st group metals. The term inclusion is carefully chosen because 1st group metals are not likely to be present as lattice substitutions due to their difference in charge and ionic radii to Fe. It is hypothesised that these inclusions are from the phyllosilicate group of clay minerals, which commonly include the elements Si, O, Al, K, Mg and Na. Table 4.4 displays the correlation coefficients between the log elemental concentration data for Al, K, Mg and Na (also included is Cl as chloride salts are common for 1st and 2nd group metals). The high LOD for Si for NAA (approximately 10%w/w) means that this elemental data is not available for comparison. The table shows good correlation between the presence of K and all other displayed elements with a particularly strong correlation to Al (0.91, n=12). Cl also shows good correlation with K, Mg and Na (all values >0.7) suggesting the inclusion of 1st and 2nd group chloride salts into the samples.

Table 4.4 Correlation coefficients of inter elemental correlations.
(number of data points shaded grey).

	Al	Cl	K	Mg	Na	Rb
Al	1	0.06	0.91	-0.06	0.45	0.33
Cl	21	1	0.83	0.71	0.76	0.22
K	12	6	1	0.61	0.65	0.73
Mg	14	11	7	1	0.55	-0.37
Na	29	20	12	14	1	-0.07
Rb	8	6	5	4	7	1

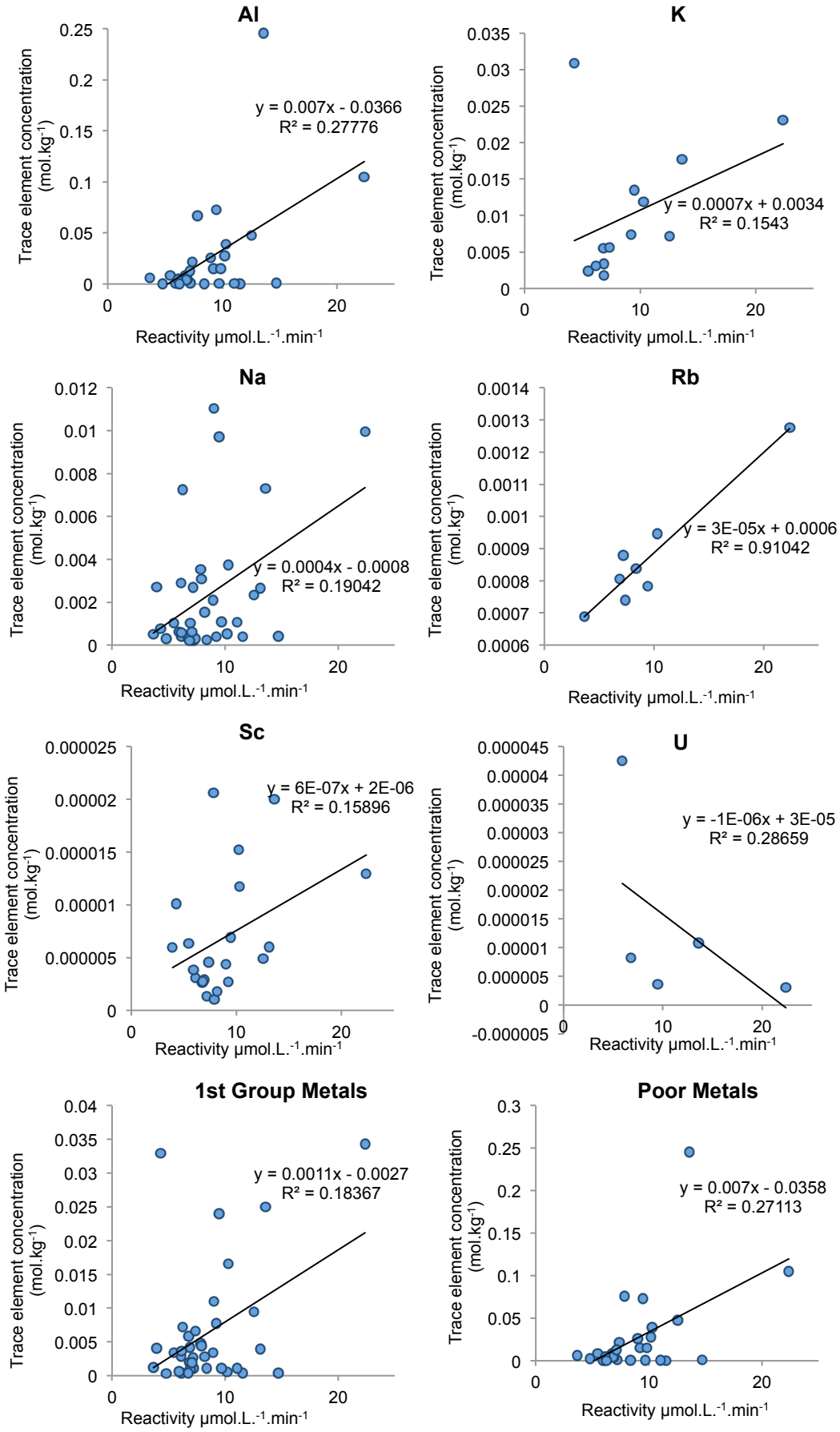

Figure 4.2 Scatter plots comparing reactivity of pyrite samples with elemental concentration.

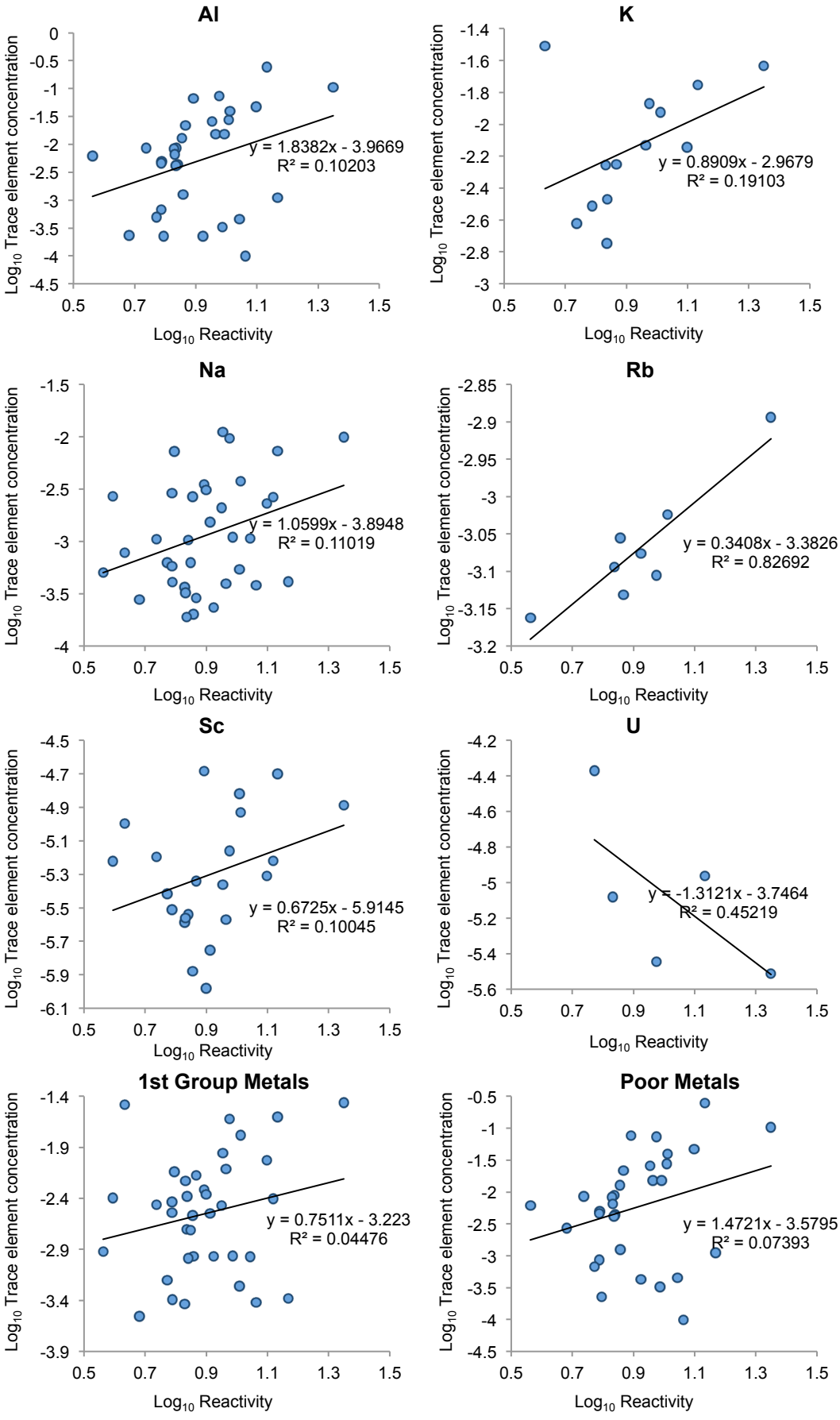

Figure 4.3 Scatter plots comparing log reactivity to log elemental concentration.

4.3.3 Semiconducting properties

The semiconducting types of the pyrite samples are presented in Table 4.5. The samples showed an even distribution of types with 19 n-type and 18 p-type. Only sample G6876 from the Isle of Elba, Italy, showed variable semiconductivity.

Given that the oxidation of pyrite is known to be an electrochemical process and that there is an observed variation in semiconducting properties of the sample, a plot comparing semiconducting type with measured reactivity is presented in Figure 4.4. The figure shows no discernible correlation between semiconductor type and reactivity, as there is a fairly even distribution of both p and n-type samples across the range of reactivities.

Using the NAA data presented in Table 4.2, the ratio of known dopants in pyrite was calculated according to Equation 4.2, the sum of the molal concentrations of As+Sb was divided by the sum of the molal concentrations of Co+Cu+Ni, the $\log_{10}$ of the resulting ratios was taken. Positive values represent an excess of p-type dopants and negative values represent an excess of n-type dopants. The resulting data is displayed in Figure 4.5.

$$dopant\ ratio = log_{10}\left(\frac{[As] + [Sb]}{[Co] + [Cu] + [Ni]}\right)$$

Equation 4.2 Dopant ratio calculation.

A good correlation with previously published work [3, 28, 29] is displayed. Samples which were measured as p-type had greater concentrations of hole donors (As and Sb) and samples which were measured as n-type generally had an excess of electron donors (Co, Cu and Ni). There were several samples where the semiconducting type did not correlate with the dopant ratio; 3 samples measured as p-type and 1 sample measured as n-type. Two possible explanations for these outliers are; there is a significant concentration of a dopant that was not measured in this study (e.g. P or Si) which contributed to the electrical properties of the sample, or the dopants that were measured did not contribute to the electronic structure of the samples and may be present as inclusions.

Table 4.5 Semiconductor type of the pyrite samples.

Sample ID	Semiconductor type
G10611	n
G11641	n
G16079	n
G17012	n
G18915	n
G20974	p
G29969	n
G29982	n
G32406	p
G32407	p
G32408	n
G32409	p
G32410	p
G32411	p
G32412	p
G32413	n
G32414	p
G32415	n
G32416	p
G32417	p
G32418	n
G32419	p
G32420	p
G32421	n
G32422	p
G32423	p
G32424	p
G32425	n
G32426	p
G32427	p
G32428	n
G32429	n
G32430	n
G33033	n
G33797	n
G33823	p
G6876	variable
G9699	n

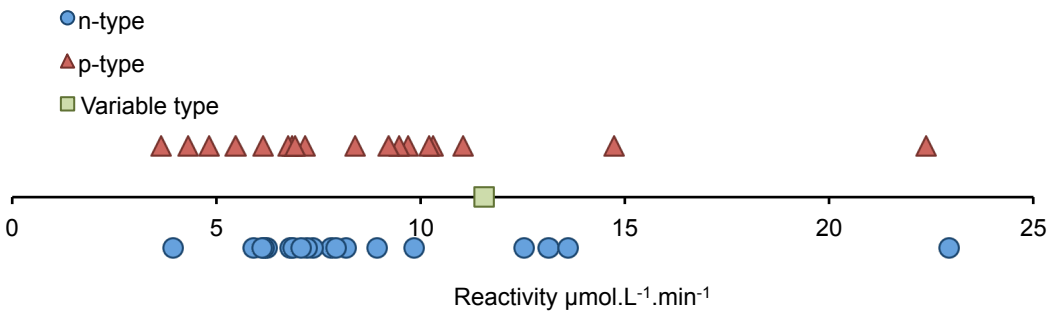

Figure 4.4 Reactivity of the pyrite samples categorised by semiconductivity type.

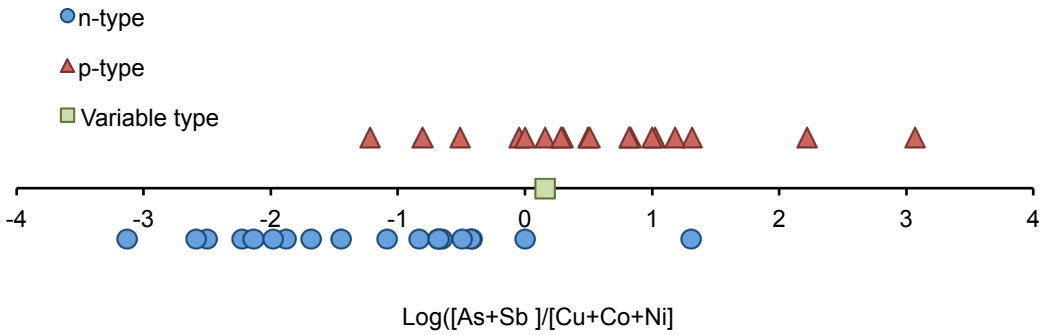

Figure 4.5 The $\log_{10}$ of the ratio of p-type dopants to n-type dopants, categorised by semiconductor type.

4.4 Conclusions

From the data presented above it can be seen that there is a strong correlation between the semiconducting type of pyrite samples and the concentration of elements known to act as dopants. Most of the samples with a greater concentration of As and Sb than Co, Cu and Ni were determined to be p-type and the majority with a greater concentration of Co, Cu and Ni than the former were determined to be n-type. We can also conclude that semiconducting type does not appear to correlate with reactivity. The type of charge carriers in the mineral does not appear to influence the rate at which the samples react.

The data presented here provides evidence that there is a correlation between the inclusion of 1st group metals and the reactivity of the samples. It is possible that the relationship between 1st group metal concentration and

reactivity are not related by cause and effect but rather are both effects of a common cause. We believe this cause to be a factor of the formation conditions of the pyrite samples, where sedimentary samples, commonly associated with clays and feldspars, explain the inclusion of 1st group metals and also produce more reactive samples. Based on this hypothesis, Chapter 5 explores the formation conditions of a subset of the samples in greater detail.

Chapter 5.

Geological origins and links to reactivity

5.1 Introduction

Pyrite is known to form in a wide variety of geological settings, these include sedimentary and metamorphic rocks as well as hydrothermal veins. The conditions of formation in each of these environments are different and could have considerable influence on pyrite's chemical and physical properties.

Pyrite is commonly formed from hydrothermal fluids; fluids at high pressures and temperatures. Hydrothermal fluids have the ability to dissolve, transport and redeposit the elements of hydrothermal ores through a variety of processes including cooling, boiling, depressurisation, oxidation and fluid rock reaction [107]. These conditions vary greatly between deposits, and also within a deposit, both spatially and temporally. Perhaps the best illustration of pyrite formation in action is to consider "black smoker chimneys", which are hydrothermal minerals that form at vents in the sea floor. In this case hydrothermal fluids mix with seawater causing the rapid precipitation of sulfide minerals [108]. After some time, the hydrothermal fluids stop and/or the chimneys collapse and burial begins. Over time pyrites can become buried deep in sediments where diagenic processes occur. Alternatively, the pyrites can be recrystallised by further hydrothermal processes. Sedimentary pyrite forms in reducing sulfur rich environments and is the most abundant sulfide mineral of sediments and sedimentary rocks [1]. A good example is pyrite that forms syngenically with coal shales. Here, acidic swamp water dissolves ferromagnesian minerals and the anoxic environment, coupled with the high sulfur concentration (both a result of decaying organic matter) provides ideal conditions for pyrite formation [109].

A small number of studies have attempted to link these varying conditions of pyrite formation with the trace element content of the resulting pyrite specimen. Loftus-Hills and Solomon [110] proposed that pyrite specimens can be grouped into three categories based on their Co:Ni ratios. They reported that sedimentary pyrites (or pyrites of diagenetic origin formed in shales) have high levels of Co (15-258ppm) and Ni (226-775ppm) and a Co:Ni ratio <1, that is, a greater level of Ni than of Co. Pyrites of probable volcanogenic origin (formed from hydrothermal fluids associated with volcanic features) that were not associated with Pb or Zn minerals had

greater concentrations of Co than Ni (Co/Ni>1). Finally, pyrites of probable volcanic origin that are associated with Pb and Zn minerals have small concentrations of Co (<1-38ppm) and Ni (4-19ppm), with a greater amount of Ni than Co (Co/Ni <1). Price [111] re-evaluated the data from Loftus-Hills and Solomon [110] and incorporated new data from their own studies. Their results reported that sedimentary pyrites had Co/Ni ratios of <1 which supports the work of Loftus-Hills and Solomons. Price also concluded that hydrothermal pyrites “generally” had Co/Ni ratios between 5-50, but do not mention the effect of association of Pb and Zn minerals. Price also notes that during metamorphism, Co is concentrated to produce large Co/Ni ratios in metamorphic pyrite. A study by Bralia *et al*. [112] supports the work of Price [111], which stated that sedimentary samples would have Co/Ni ratios of below 1, hydrothermal pyrites would have a ratio of greater than 1, while very large Co/Ni values (5-50) were likely to have volcanogenic origins.

Huston *et al.* [100] investigated Se/S ratios in pyrite. They observed that the concentration of Se in pyrites decreases with increasing temperature in volcanogenic hydrothermal systems.

Relatively few studies have attempted to correlate reactivity with trace element concentration (also described in section 1.4.3) [39, 59]. Chirita [59] analysed the reactivity of 6 pyrite samples and measured Co, Ni, Cu, Zn and As. They concluded that trace element composition did not influence reactivity in their experiments. Similarly, Nicholson [39] measured the reactivity of 6 pyrite samples and their Al, Ba, Ca, Co, Cu, Fe, Mg, Mn, Ni, Pb, Si, Sr, Th, Ti, V, Zn and Zr concentrations. They noted that two of their samples did have significantly different reaction rates to the rest and that trace element concentrations may play an important role in determining reaction rates, but they were unable to draw any firm conclusions from their limited data. Lenher *et al.* [27] found from their electrochemical experiments that synthetic pyrites doped with As (98–812ppm) produced the greatest current densities (were the most reactive), followed by pyrites doped with Co (452–3057ppm) and Ni (195–2812ppm) and then undoped pyrites (impurities <50ppm). Cruz *et al.* [56] studied 5 pyrite samples, assessing their reactivity and trace element concentration (Ni, Cu, As, Zn, Pb). They conclude that

samples with a greater percentage of other sulfide mineral inclusions (~5-15%w/w other sulfide inclusions), particularly galena and sphalerite, reacted slower than samples with fewer impurities. The sample which contained <0.2%w/w sulfide impurities and fewer than 3.2% impurities overall had a dissolution of Fe approximately twice that of the other samples within the same timeframe. The authors attribute these observations to the galvanic protection of pyrite by minerals with a lower rest potential (much like a sacrificial anode on a ship's hull). By inspecting the kinetics of the oxidation it can be seen that for all pyrite samples there is an initial rapid increase in oxidation products followed by an almost as rapid decrease, this is attributed to the initial oxidation and then passivation of the mineral surface by oxidation products, where galena and sphalerite are preferentially oxidised. This preferential oxidation results in a more rapid passivation of the surface, thus protecting against further oxidation of pyrite. However, it should be noted that Cruz *et al.* failed to remove the fine pyrite particles adhering to their fractioned grains after they dry sieved their samples (as proved by SEM images of their pre-leached samples). This would lead to erroneously large initial rates of reaction (due to a large surface area) followed by a decrease in rate once the finer particles had been dissolved. Therefore, while preferential oxidation of minerals with a lower rest potential may occur and may lead to passivation of the mineral surface, the results presented in Cruz *et al.* are almost certainly influenced by a rapid change in available surface area for reaction.

In one of the more comprehensive studies concerning pyrites variation in reactivity, Liu *et al.* [53] investigate the reactivity of three hydrothermal and five sedimentary pyrites (three of which are associated with coal seams). They found that the sedimentary samples associated with coals exhibited significantly greater rates of dissolution than the other samples, with sedimentary coal pyrite samples having an average dissolution rate of an order of magnitude greater than the hydrothermal samples. They conclude that "the observed difference in dissolution rate amongst pyrites cannot be completely explained by differences in surface area", and they attempt to correlate the observed difference with 40 measured trace elements to no avail. They note that the hydrothermal samples were generally greater than

sedimentary samples in Co (46-6004ppm compared to 0.3–12ppm), Bi (16–95ppm compared to <0.11ppm) and Te (1–01ppm compared to <0.04ppm). While compared to hydrothermal samples, the sedimentary samples contained more Tl (4–53ppm compared to 0.01–0.03), Ba (3–23ppm compared to 0.13–0.22ppm) and Rb (0.45–3.8ppm compared to 0.15–0.29ppm). This agrees with the observation of increased concentration of 1st group metals in sedimentary samples presented in Chapter 4. To address the theory that semiconducting properties of pyrite samples impacts their reactivity, the authors calculate the ratio of As+Co/Co+Ni for their pyrites (note that they do not actually measure the semiconducting properties) and observe that 4 of the 5 sedimentary samples had ratios >1 (potential p-type) and were generally more reactive, while the hydrothermal samples all had ratios <1 (potential n-type).

In the previous chapter, it was observed that the reactivity of many samples correlated with their concentration of 1st group metals. We hypothesised that these 1st group metals were present as phyllosilicate clay and other clay layer silicates inclusions due to the good correlations between the detected concentrations of Al, K, Mg, Na and Rb. Clays and other layer silicates such as these are often a major constituent of the host rocks of sedimentary and early diagenetic pyrites such as shales. Therefore, we hypothesise that the reactivity of the pyrite samples is correlated with their conditions of formation. In this chapter, the conditions of formation of a subset of the samples analysed previously are investigated in more detail in an attempt to further understand any correlations that may exist.

5.2 Materials and methods

5.2.1 Conditions of formation

A subset of 9 of the 40 previously analysed samples was chosen for more detailed analysis. The samples were chosen to represent as wide a range of reactivities as possible. The samples were also selected on their general availability, so that other researchers may be able to replicate these measurements in the future. Formation conditions of the final 9 samples are summarised in **Table 5.2**. A more detailed summary of the geological environment for the each of the samples is presented in Appendix B.

Establishing the formation conditions for a given pyrite sample from a particular deposit can be very difficult. Many deposits are very large, from 100s to 1000s of metres in all dimensions, and none of the specimens used in this study had accurate location information from within the mine sequences. In addition, in many deposits there have been numerous overprinting hydrothermal or deformational events, so, even if the exact locality of the sample is known it is often difficult to determine the exact nature of the formation event and the solution and pressure and temperature (PT) conditions at the time. PT conditions are often estimated from fluid inclusion studies (investigating the chemistry of fluids trapped during the formation of associated minerals such as quartz or feldspar) but these tend to give a wide range of temperatures (typically from 100 to 400°C) for a single deposit. What is perhaps generally clear is whether the Fe and S have been transported considerable distances, as in the case of high temperature hydrothermal veins associated with igneous intrusions, or the pyrite has been deposited within a sedimentary environment and either recrystallised during diagenesis (burial) or by local hydrothermal fluids. In the latter case the Fe and the S may not be transported large distances by the fluid.

5.2.2 Summary of sample information

Table 5.2 provides a summary of the conditions of formation, the reactivity and semiconducting type for the 9 samples, which have either statistically significant small or large reactivity. The samples that were chosen had reactivities which lay outside of the interquartile range of the entire sample

set to provide a subset of samples with large variance. This would help to elucidate any systematic differences between the samples leading to their difference in reactivity. The updated descriptive statistics, including only 38 samples can be seen in Table 5.1.

Table 5.1 Descriptive statistics for the 38 pyrite samples.

Parameter	Value
n	38
Average (µmol.L^{-1}.min^{-1})	8.52
Standard deviation (µmol.L^{-1}.min^{-1})	3.51
Median (µmol.L^{-1}.min^{-1})	7.59
Minimum (µmol.L^{-1}.min^{-1})	3.65
Maximum (µmol.L^{-1}.min^{-1})	22.4
Range (µmol.L^{-1}.min^{-1})	18.7
0.25 percentile (µmol.L^{-1}.min^{-1})	6.37
0.75 percentile (µmol.L^{-1}.min^{-1})	9.80
Inter quartile range (µmol.L^{-1}.min^{-1})	3.43

Table 5.2 Summary of the conditions of formation, semiconductor type and reactivity of the final 9 samples.

Samples Code	Location	Formation Conditions	Physical appearance	Semiconductor type	Reactivity (µmol.L^{-1}.min^{-1})
G33797	Huanzala Mine, Huallanca District, Dos de Mayo, Peru	High temperature hydrothermal	Coarse euhedral crystals to 1 cm	n	3.65
G17012	Poona Mine, Moonta, South Australia	High temperature hydrothermal	Coarse euhedral crystals to 2 cm	n	3.93
G32427	Ophir Hill Mine, Ophir, Tooele County, Utah, USA	High temperature skarn	Coarse cubes to 0.5 cm	p	4.30
G32422	Siglo XX Mine, Llallagua, Bolivia	High temperature hydrothermal	Coarse euhedral crystals to 2 cm	p	4.80
G32414	Portland Limestone Quarry, Florence, Fermont County, Colorado, USA	Sedimentary diagenic. Temperature unknown	Spherical nodules to 1 cm	p	5.47
G29969	Paulsens Mine, Wyloo, Western Australia	Mesothermal vein in sediments. Medium temperature	Massive pyrite	n	13.14
G33033	Ampliación a Victoria Mine, Navajún, La Rioja, Spain	Metamorphism of sediments. High temperature	Coarse cubes to 5 cm	n	13.60
G32419	Black Cloud Mine, Leadville, Colorado, USA	Hydrothermal replacements of sediments. High temperature	Coarse cubes to 3 cm	p	14.72
G20974	Sparta, Randolph County, Illinois, USA	Sedimentary coal shales. Low temperature	Disk concretion to 10 cm	p	22.37

5.2.3 Laser ablation inductively coupled plasma mass spectrometry

Microprobe analysis of the pyrite samples was first undertaken to provide a baseline Fe concentration for the LA-ICP-MS analysis.

The average concentrations of the Fe in the pyrite samples were determined using a Cameca SXFive electron microprobe (Adelaide Microscopy, situated at The University of Adelaide) operating in wavelength dispersive spectroscopy mode (WDS). An accelerating voltage of 20KV and a beam current of 20nA was used for all samples. A LLIF crystal was used for the analysis of Fe. Samples were analysed for a total count time of 20 seconds (10 seconds of peak time and 5 seconds backgrounds on either side of the X-ray peak). Calibration prior to analysis was performed using the Ast30 Marcasite standard (53.46%w/w S and 46.54%w/w Fe), and a (Pouchou and Pichoir) PAP correction procedure was applied in the Cameca software.

LA-ICP-MS analysis was performed using a Resonetics M-50 193 nm Excimer laser attached to an Agilent 7700cs ICP-MS (Adelaide Microscopy, situated at the University of Adelaide). Ablation of the samples was conducted in a He atmosphere with Ar implemented as carrier gas. Spot analyses were conducted with a beam diameter of 75µm, a repetition rate of 5Hz and with energy output at 100mJ, set to produce a fluence at the sample of ~6 $J.cm^{-2}$. Data was collected in counts per second (CPS) using time-resolved data acquisition in fast peak-jumping mode. CPS to ppm concentration conversions were carried out using the data reduction software GLITTER for LA-ICP-MS. Total acquisition time per analysis was 60 seconds, with 30 seconds of background measurement followed by 30 seconds of sample ablation. Calibration was performed against the United States Geological Survey (USGS) pressed pellet sulfide standard MASS-1 (previously known as PS-1) [113]. Two batches of 10–14 spot analyses were collected from each sample. Each batch was bracketed by repeat analyses of MASS-1, allowing monitoring of, and correction for, instrumental drift. ^{56}Fe was used as the internal standard for the pyrite samples, assuming 58.85%w/w to 59.99%w/w FeO depending on the sample (FeO concentration was calculated individually for each sample using the results of the microprobe analysis, assuming homogeneity in each sample).

Concentration data was converted from ppm to mol.kg^{-1} for ease of comparison to the NAA data. The average elemental concentrations were calculated for each sample the ratios of Co/Ni and S/Se were taken, the results are displayed in Table 5.3.

5.2.4 Scanning electron microscopy

A PHILIPS XL30 field emission scanning electron microscope with an energy dispersive X-ray spectrometer (EDS) detector was used to examine the minerals for major inclusions and inhomogeneities, efficacy of mineral grain preparation for reactivity studies and size distribution. The conditions for each of the experiments are detailed in the following sections.

5.2.4.1 Homogeneity

For homogeneity studies fragments of pyrite samples were mounted in epoxy resin blocks and polished. The detector was used in backscattered electron (BSE) mode so that inhomogeneities such as inclusions could be easily identified based on differences in contrast, which are related to average atomic number. The elemental composition of the sample and any inhomogeneities were analysed with the EDS detector.

5.2.4.2 Particle size distribution

For mineral grain analysis samples, were crushed, sieved and cleaned, as per Chapter 2, mounted on SEM stubs using carbon tabs and thin film carbon coated. Mineral grains were examined for surface cleanliness (absence of small adhering particles to larger grains). Grains were also analysed for particle morphology and size distribution using EDAX Genesis particle analysis software [114].

5.3 Results and discussion

5.3.1 Particle size distribution

Sample particle size distribution, resulting from the preparation procedure (Chapter 2) was assessed to ensure that apparent variations in reactivity were not unduly influenced by variations in surface area.

The sample fraction had a surface area that was too small for reliable (or accurate) Brunauer–Emmett–Teller (BET) analysis, so SEM imaging was

used to assess the surface area of a number of particles (n>100) from each sample. The results, presented in Figure 5.1 show that the samples have maximum diameters in a narrow range 44-74µm. While the target fraction was 53-106µm, the real values fall toward the smaller end of this fraction. This may be due to the removal of small adhering particles post-sieving, effectively decreasing the diameter of the fractioned particles. The average area of the particles also shows good correlation to particle length, suggesting a reasonably consistent shape of the particles. It is worth noting here that the overall area of pyrite is not necessarily linked linearly with the sample reactivity. McKibben and Barnes [57] performed SEM studies on pyrite samples and noted that oxidant attack is not uniform across the surfaces, occurring predominantly at high energy sites which include, but are not limited to, defects, solid and liquid inclusions, cleavage and fracture traces inherited from crystal growth and history (including surface preparation) [57] and studies by Lieu *et al.* [53] present data that agrees with these observations.

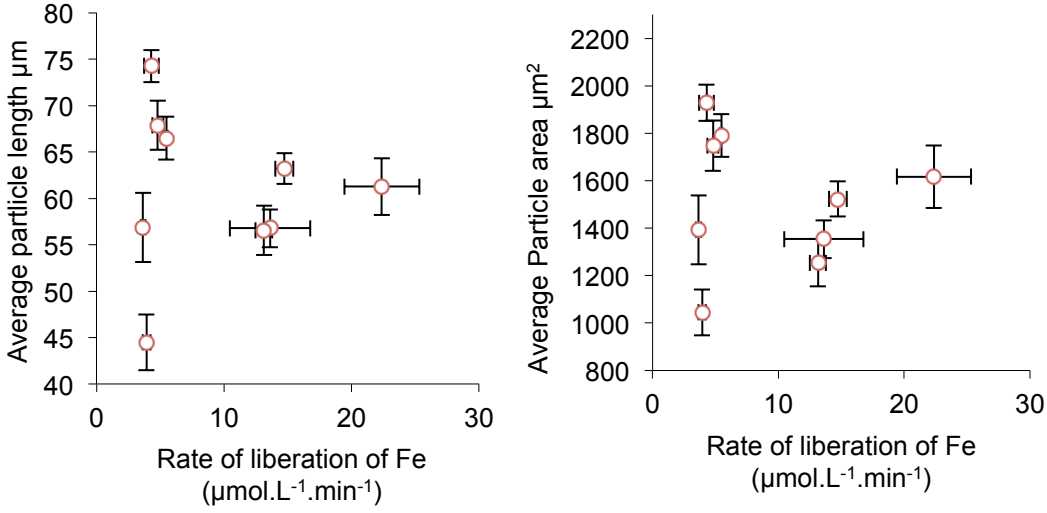

Figure 5.1 Scatter plot showing average particle length and area verses reactivity. *Error bars showing ± 1 standard error.*

5.3.2 Homogeneity

The homogeneity of the samples was investigated by SEM with backscatter (BSE) imaging. The results are presented in **Figure 5.2**. The SEM images show that the samples have a high level of homogeneity with no significant

mineral inclusions, as supported by the NAA data (Chapter 4). The Poona Mine (G17012) and Huanzala Mine samples had minor inclusions, which appeared as light areas and were determined by EDS to contain Cu and S (probably chalcopyrite). The Victoria Mine sample (G33033) contained several small inclusions which gave strong EDS peaks corresponding to Fe, S, Si, and O, consistent with chloritoid inclusions. The Siglo XX Mine sample (G32422) displayed two types of inclusions. The darker inclusion gave peaks for Zn and S (probably sphalerite) while the lighter area gave peaks for Cu, Sn, and Fe (probably stannites). In all cases the level of inclusions found by SEM is <1% which is consistent with the powder diffraction traces which contained only pyrite reflections.

G20974

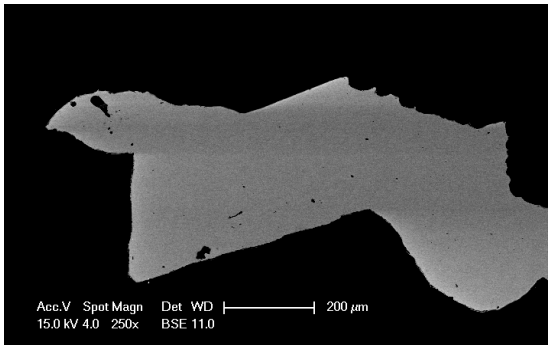

G17012

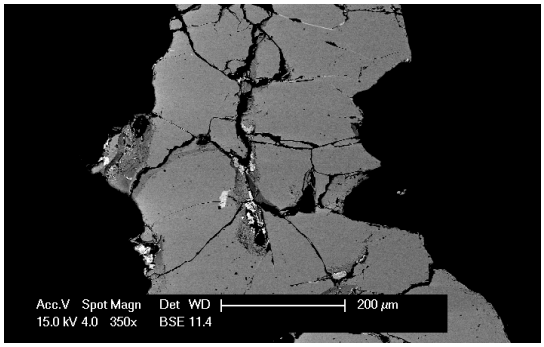

G33797

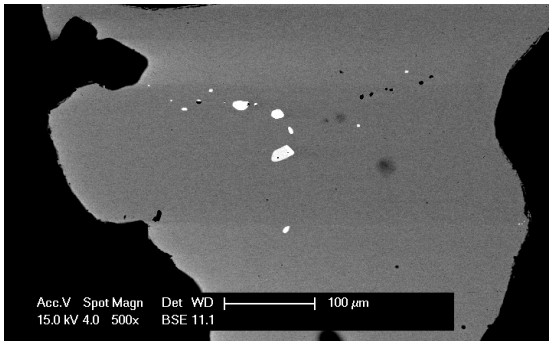

G33033

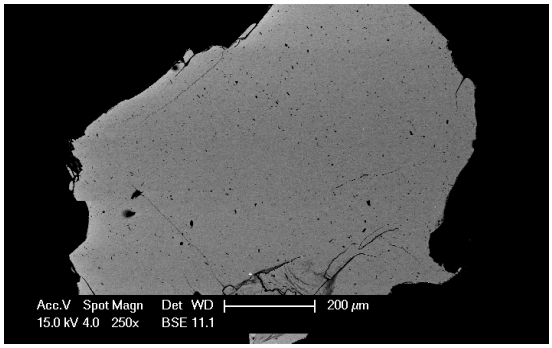

G32422

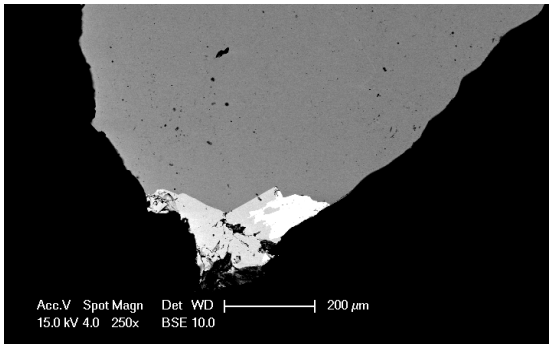

G32419

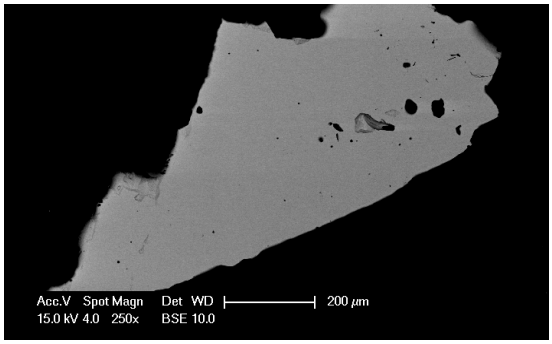

G32417

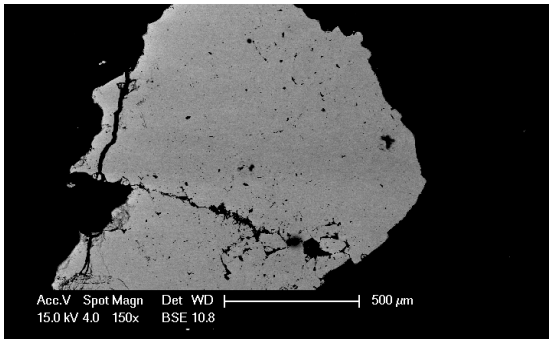

G32414

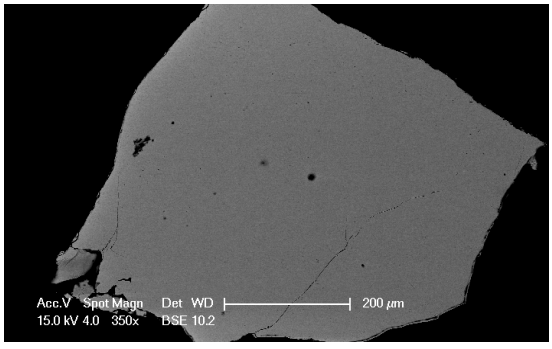

G29969

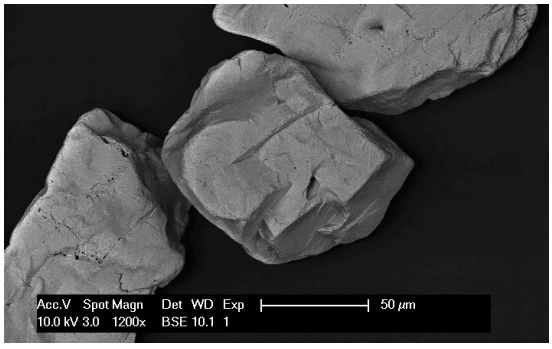

Figure 5.2 SEM pictures of 9 pyrite samples.
SEM picture taken using backscatter detector to show impurities in different shades. All samples are mounted in epoxy blocks except G29969 which is on a stub. Note scale bars at the foot of each image.

5.3.3 Co/Ni and S/Se ratios

While NAA boasts good detection limits for a wide array of elements, there are several elements for which the sensitivity of the analysis is quite poor. For example, Ni is expected to be present as a trace or minor element in relatively high levels in the pyrite samples and has been indicated as an element whose relative concentration is an indicator of formation conditions [110-112]. Despite this, NAA results presented in Chapter 4 reported Ni in concentrations above the limit of quantitation (LOQ) in only 7 of the 38 samples. This is due to the high LOD of Ni using this technique. The average LOD for the ANSTO measurements was 694ppm (LOQ=2082ppm) and 60ppm for MURR (LOQ=180ppm). Consequently, it was decided to supplement the data by performing LA-ICP-MS on the subset of 9 samples. The advantage of this technique is that the LODs are generally sub-ppm for most analysable elements. The limitation of using LA-ICP-MS is that it is a near surface technique that only analyses a very small portion of the pyrite in comparison to NAA, which analyses bulk samples. As a result, we expect to find different elemental concentrations and a greater degree of variability using LA-ICP-MS compared to NAA, nevertheless, the relative concentrations of elements should be maintained.

Table 5.3 summarises the formation conditions and selected LA-ICP-MS elemental concentrations and Co/Ni and S/Se ratios of the 9 pyrite samples. The results presented here displayed some consistency with the previously noted correlations between formation conditions and Co/Ni ratios. All of the low temperature sedimentary samples did have Co/Ni Ratios <1, consistent with the work of Loftus-Hills and Solomon and Price [110, 111]. The sedimentary and mesothermal samples did, on average, have larger concentrations of Co and Ni than the higher temperature samples. Three of the higher temperature hydrothermal samples also had ratios <1, these samples (G32427–Ophir Hill Mine, G33797–Huanzala Mine and G32422–Siglo XX Mine) are also associated with Pb/Zn deposits, a trend that was also suggested by Loftus-Hills and Solomon. However, the Black Cloud Mine (G32419) sample is a high temperature deposit, associated with Pb and Zn sulfides, but has the largest Co/Ni ratio of all the samples, which does not agree with the previously published work. Paulsens Mine (G29969) and

Poona Mine (G17012) are mesothermal and high temperature respectively, they both have Co/Ni ratios ~2 and relatively large Co and Ni concentrations, these mines are not associated with Pb or Zn minerals, which agrees with the findings of Loftus-Hills and Solomon.

Work by Huston *et al.* [100] suggested that for volcanogenic samples the S/Se ratios would increase with increasing temperature, due to the decrease in Se concentrations, however, there does not appear to be any such correlation in the data presented here.

Table 5.3 Sample conditions of formation and selected elemental concentrations and ratios.

Sample codes	Formation conditions	[Co] ($\mu mol.kg^{-1}$)	[Ni] ($\mu mol.kg^{-1}$)	[S]* ($mol.kg^{-1}$)	[Se] ($\mu mol.kg^{-1}$)	[Co]/[Ni] Ratio	[S]/[Se] Ratio
G32422	High temperature hydrothermal	23.07	947.2	16.63	79.98	0.024	200,586
G33797	High temperature hydrothermal	0.074	0.456	16.63	711.9	0.1630	23,359
G32419	Hydrothermal replacements of sediments. High temperature	73.05	5.497	16.58	10.88	13.29	1,523,225
G32427	High temperature skarn	1.71	230.4	16.54	10.69	0.0074	1,624,972
G29969	Mesothermal vein in sediments. Medium temperature	10,372	4221	16.53	235.5	2.458	72,330
G17012	High temperature hydrothermal	1947	740.2	16.70	1150	2.631	14,526
G33033	Metamorphism of sediments. High temperature	1993	9199	16.63	289.1	0.2168	57,535
G32414	Sedimentary diagenic. Temperature unknown	26.69	1046	16.71	149.9	0.0255	111,447
G20974	Sedimentary coal shales. Low temperature	45.98	651.8	16.49	317.1	0.0705	56,091

*S determination taken from electron microprobe analysis due to increased reliability of determinations

With regard to elemental ratios as indicators of formation conditions; because pyrite is formed over a wide variety of geological conditions and undergoes transformation, diagenesis and recrystallisation in so many different manners, it seems unlikely that one element or ratio thereof will effectively indicate formation conditions. Co/Ni ratios may be effective in identifying samples from one specific locality that have undergone transformations

differently or to a different extent, but these ratios are unlikely to have any bearing when compared to samples from other sites.

5.3.4 Reactivity and formation conditions

In Chapter 4, a correlation was observed between the content of 1st group metals and the reactivity of the samples. We hypothesised that the concentration of 1st group metals was present as clay and other layer silicate mineral inclusions due to their correlation with Al. These clays are common in sedimentary settings, such as shales, which host sedimentary and low temperature pyrites. From this we hypothesise that the lower temperature, sedimentary pyrites are more reactive than higher temperature pyrites. From Table 5.2 it can be seen that there is a correlation between reactivity and formation conditions, where the low temperature sedimentary samples and those associated with sediments tended to be more reactive than the high temperature hydrothermal samples. The Huanzala Mine (G33797), Poona Mine (G17012) and Siglo XX Mine (G32422), all classified as high temperature hydrothermal, have reactivities below 5µmol.L^{-1}.min^{-1}. The three most reactive samples, being the Victoria Mine (G33033), Black Cloud (G32419) and Sparta (G20974) samples were all sedimentary or associated with sediments and had reactivities greater than 3 times the aforementioned high temperature hydrothermal samples. It is interesting that even sedimentary pyrite, such as the Black Cloud sample (G34219) and the Victoria Mine sample (G33033), that have gone through some moderate to high temperature transformation (metamorphism and hydrothermal replacement) retain this elevated reactivity. These findings could be explained by the work of Pitcairn *et al.* [115] who showed that the trace element composition of pyrite is reasonably consistent through metamorphism up to a temperature of approximately 350°C. This demonstrates that the chemistry of these pyrites may be a reasonably closed system during transformational events. In the case of the Black Cloud sample where replacement of sediments has occurred, work by Thomas *et al.* [116] may explain the increased reactivity. They noted that diagenetic and early hydrothermal pyrites scavenge trace elements from their host rocks, often organic rich shales. The key difference may be in how far the

hydrothermal fluids transport the Fe and S. In the case where hydrothermal fluids are transported large distances from their sedimentary origin, the chemistry of the mineral is likely to be altered to a greater extent, with preferential deposition and or uptake of certain elements. When hydrothermal fluid is not transported the composition and therefore chemistry of the mineral is likely to remain relatively consistent. For sedimentary samples this means retaining the clay layer silicate inclusions. Further work is required to confirm these hypotheses and this will be discussed further in Chapter 6.

5.4 Conclusions

In conclusion the relationship between the Co/Ni and formation temperature showed some agreement with previously published work, however, care should be taken when attempting to determine formation temperature from these ratios as the trends are rather imprecise and would probably only be valid for comparing mineral samples from the same geological setting. S/Se ratios did not appear to correlate with pyrite formation conditions for the samples presented here. There is a correlation between conditions of formation and reactivity. We observed that samples of sedimentary origin are more reactive while those of higher temperature hydrothermal origin are less reactive. While the reason for this is currently unclear it is likely due either to an increase in reactive surface area caused by defects in the crystal structure or a more fundamental change in the pyrite chemistry, caused by the substitution of elements commonly found in sedimentary geology.

Chapter 6.

Conclusions and future work

6.1 Conclusions

A method for the rapid determination of total solubilised iron using flow injection analysis with 5-SSA was successfully developed. The method is capable of a determining total iron concentration at a rate of 60min^{-1} and has a LOD of 0.5ppm with typical %RSD <2%. The method was found to be free from interference from metals commonly associated with pyrite. The method was used to monitor the oxidation of pyrite samples by hydrogen peroxide, yielding a measure of sample reactivity. Analysis of the reactivity of 40 mineral samples from around the globe gave a 6-fold variation in reaction rate, providing evidence that there is an inherent variation in pyrite reactivity from different locations.

Since trace element composition is hypothesised to influence the reactivity of pyrite and has been previously linked to conditions of formation, NAA of the pyrite samples was performed. As a point of interest the analysis was undertaken at two different facilities, using two different calibration methods; the relative comparator and the k_0 methods. Statistical analysis of both of the resulting data sets showed that the analyses were statistically indistinguishable. Trace element data of previously published pyrite NAA data was also found to be indistinguishable from the analyses presented here.

As with other semiconducting materials, the trace element composition of pyrite is known to affect its electrical properties. The semiconductor type of the pyrite samples was shown to be influenced by the concentration of known hole donors compared to the concentration of electron donors, the majority of samples with a larger molar concentration of hole donors were found to be p-type and those with a larger molar concentration of electron donors were found to be n-type. The reactivity of the samples, however, did not show any correlation with semiconductor type.

The concentration of some 1st group metals as well as Al were shown to correlate positively with the reactivity of the samples. These elements are constituents of common clay and layer silicate minerals and their concentrations were also found to correlate with each other, suggesting a greater concentration of inclusions of clay minerals in the more reactive

samples. Clay and layer silicate minerals are common in predominantly sedimentary systems. Therefore, formation conditions of a subset of the samples were researched and it was found that samples of sedimentary origin were significantly more reactive than those of higher temperature hydrothermal origin. Furthermore, samples of sedimentary origins that had undergone higher temperature transformations maintained the elevated reactivity. This suggests that it is the chemical composition of these sedimentary pyrites (which remain relatively unchanged after local hydrothermal transformations) that bestows the elevated reactivity to the samples.

6.2 Future directions

6.2.1 Samples from well documented origins

Drawing conclusions about how the conditions of mineral formation influences their properties is often impeded by the lack of detailed information available about the geology of the site and the exact location where the samples were collected. It would therefore be advantageous to be able to collect mineral samples of well know origin, with well constrailed geology.

6.2.2 Method development

The method for determination of total iron presented here could easily be adopted for the colorimetric determination ferric ions by 5-SSA in acidic conditions and indeed the subsequent determination of total iron to provide information on the speciation of iron in solution. This would be particularly useful if measuring the oxidation of pyrite via a “natural” mechanism, it would allow observation of the change in dependence on oxidant, from initial reaction with dissolved oxygen through to an increase in concentration of ferric ions which then take on the role of primary oxidising agent. Flow injection methodology has also been implemented in the determination of anions in solution, therefore, there may be scope to implement the simultaneous colorimentric determination iron and of sulfate (by methymol blue or barium chloranilate). This would give further insight into the reaction kinetics of the oxidation of pyrite.

6.2.3 Total organic content

We have shown that there is a correlation between the formation conditions of pyrite samples and their reactivity. Samples of sedimentary origin have been shown to be more reactive than their high temperature hydrothermal counterparts, these sedimentary samples often have much larger content of organic matter (pyrite from the Sparta Illinois are known to contain enough organic matter to be flammable). It would be interesting to measure the organic content of pyrite samples from a variety of sources and compare them to their measured reactivities.

6.2.4 Synthetic pyrite samples

There has been prior research into the reactivity of synthesised pyrite samples with different levels of electron and hole donating dopants. However, it would be worth investigating the reactivity of samples synthesised to mimic different geological conditions and temperatures. Being able to control factors such as impurity concentration while varying formation temperature and measuring the reactivity of these samples may provide valuable insight into the mechanism of pyrite reactivity and the influence of formation conditions.

Appendices

Appendix A

Unedited elemental concentration data for the analysis of pyrite samples from neutron activation analysis. Presented below is the data from both the MURR and ANSTO analyses. Samples are presented in alpha numeric order. All values are in ppm unless otherwise stated, ND denotes that the element was not detected in the sample.

MURR Analysis:

	LOD	% Unc.	G11641	G16011	G16079	G17012	G18915	G20974
As	1.8	2	92.7546	628.2407	ND	236.8578	ND	238.8164
La	0.08	2	ND	2.2621	0.1097	11.0248	ND	1.4658
Lu	0.03	5	ND	ND	ND	ND	ND	0.0231
Nd	6	10	ND	ND	ND	8.366	ND	ND
Sm	0.05	2	ND	0.2063	ND	1.2468	ND	0.2157
U	0.8	10	ND	ND	ND	0.7465	ND	0.7549
Yb	0.18	7	ND	ND	ND	ND	ND	ND
Ce	0.7	2	ND	3.5177	ND	23.002	ND	2.1263
Co	0.02	1	1220.0544	1283.1383	50.9146	585.6279	2051.2996	3.4401
Cr	0.45	10	14.8073	2.4668	3.056	2.3629	ND	14.7527
Cs	0.18	15	ND	ND	ND	ND	ND	0.2436
Eu	0.01	2	ND	ND	0.0254	0.1968	ND	0.0263
Fe	1500	0.2	435479.3125	433956.437	432994.375	420608.2188	437753.75	430571.0313
Hf	0.2	3	ND	ND	ND	ND	ND	0.1999
Ni	60	20	ND	ND	ND	311.9214	329.6629	35.8615
Rb	7	10	ND	ND	ND	ND	ND	ND
Sb	0.05	5	2.2619	1.6166	0.2704	ND	ND	36.2316
Sc	0.01	1	ND	ND	0.0792	0.269	ND	0.5421
Sr	52	15	ND	ND	ND	ND	ND	ND
Ta	0.06	20	ND	ND	ND	ND	ND	ND
Tb	0.12	15	ND	ND	ND	ND	ND	ND
Th	0.1	10	ND	ND	ND	ND	ND	0.6039
Zn	4	7	ND	208.3799	28.8132	ND	ND	ND
Zr	42	20	ND	ND	ND	ND	ND	ND
Al	500	25	ND	545.4836	ND	1388.24	413.4859	3315.0464
Ba	40	30	ND	ND	ND	ND	ND	ND
Dy	0.2	10	ND	0.1928	0.1628	2.4756	ND	0.0864
K	400	20	194.8772	ND	ND	ND	ND	1022.9149
Mn	0.2	3	9.3701	14.1126	65.59	4.2036	3.8371	9.8523
Na	10	5	51.4694	78.0648	65.2427	92.456	146.8708	250.6168
V	2	10	ND	ND	15.6673	ND	ND	15.4633

	LOD	% Unc.	G29969	G29982	G30334	G32406	G32407	G32408
As	1.8	2	324.7442	ND	185.9447	414.5193	88.8648	8.5322
La	0.08	2	ND	1.3617	ND	ND	ND	12.9897
Lu	0.03	5	0.1608	ND	ND	ND	ND	0.1475
Nd	6	10	ND	ND	ND	ND	ND	ND
Sm	0.05	2	0.0746	0.1916	ND	ND	ND	2.081
U	0.8	10	ND	ND	ND	ND	ND	1.4031
Yb	0.18	7	ND	ND	ND	ND	ND	1.066
Ce	0.7	2	ND	2.1235	ND	ND	ND	23.412
Co	0.02	1	162.4554	8.7534	1008.6866	462.3172	12.4179	974.2182
Cr	0.45	10	2.4289	3.4451	ND	2.4775	2.8353	5.9362
Cs	0.18	15	ND	ND	ND	ND	ND	ND
Eu	0.01	2	0.0338	0.0368	ND	ND	ND	0.4814
Fe	1500	0.2	423605.625	431650.312	240053.5625	443523.4688	435459.9063	446098.5313
Hf	0.2	3	ND	0.1391	ND	ND	ND	5.0451
Ni	60	20	526.8878	96.6876	ND	ND	ND	199.0669
Rb	7	10	ND	ND	ND	ND	ND	ND
Sb	0.05	5	9.064	0.2119	33.6598	ND	0.6483	0.5606
Sc	0.01	1	0.271	0.1317	0.1444	ND	ND	0.9271
Sr	52	15	ND	ND	ND	ND	ND	ND
Ta	0.06	20	ND	ND	ND	ND	ND	0.3614
Tb	0.12	15	ND	ND	ND	ND	ND	0.3842
Th	0.1	10	ND	0.5327	ND	ND	ND	6.1326
Zn	4	7	ND	ND	258338.2813	ND	465.2123	ND
Zr	42	20	ND	ND	ND	ND	ND	121.5054
Al	500	25	ND	1245.6847	2718.7573	115.3431	ND	2047.5089
Ba	40	30	ND	ND	606.2731	ND	ND	19.8367
Dy	0.2	10	ND	ND	ND	ND	ND	2.0876
K	400	20	ND	176.9645	ND	ND	ND	437.7487
Mn	0.2	3	147.4755	6.3973	234.949	3.5095	33.0152	120.4693
Na	10	5	91.0673	65.3789	1187.9799	63.121	68.694	110.7503
V	2	10	ND	ND	91.3073	ND	ND	ND

	LOD	% Unc.	G32409	G32410	G32411	G32412	G32413	G32414
As	1.8	2	15.701	13.6355	204.0257	944.0173	1.9621	7.8006
La	0.08	2	0.0418	ND	0.3378	0.0702	0.2145	0.3136
Lu	0.03	5	ND	ND	ND	ND	ND	ND
Nd	6	10	ND	ND	ND	ND	ND	ND
Sm	0.05	2	ND	ND	0.0744	ND	ND	ND
U	0.8	10	ND	ND	ND	ND	ND	ND
Yb	0.18	7	ND	ND	ND	ND	ND	ND
Ce	0.7	2	ND	ND	0.7443	ND	ND	ND
Co	0.02	1	1.3778	14.5408	0.8692	1.8138	3.8058	3.7463
Cr	0.45	10	2.3343	2.4453	3.9848	2.5387	2.9899	3.3704
Cs	0.18	15	ND	ND	ND	ND	ND	ND
Eu	0.01	2	ND	ND	ND	ND	ND	0.0101
Fe	1500	0.2	430678.4375	431791.125	427974.125	443488.875	436929.9688	438210.9688
Hf	0.2	3	ND	ND	ND	ND	ND	ND
Ni	60	20	ND	ND	ND	ND	126.7497	48.7932
Rb	7	10	ND	ND	16.2281	ND	ND	ND
Sb	0.05	5	4.0777	0.2724	15.5377	70.5512	0.2193	0.6381
Sc	0.01	1	ND	ND	0.1509	ND	0.1186	0.0731
Sr	52	15	ND	ND	ND	ND	ND	ND
Ta	0.06	20	ND	ND	ND	ND	ND	ND
Tb	0.12	15	ND	ND	ND	ND	ND	ND
Th	0.1	10	ND	ND	0.1366	ND	0.1829	ND
Zn	4	7	ND	70.1082	ND	ND	4.4997	7.6388
Zr	42	20	ND	ND	ND	ND	ND	ND
Al	500	25	ND	ND	1938.0081	542.5175	1838.6997	1193.1771
Ba	40	30	ND	ND	50.9302	ND	ND	ND
Dy	0.2	10	ND	ND	ND	ND	0.1307	ND
K	400	20	ND	789.1752	757.0983	ND	ND	ND
Mn	0.2	3	4.1955	318.4663	8.6333	3.4994	101.2134	334.4066
Na	10	5	114.5331	84.0231	288.4953	93.2686	66.3269	81.2969
V	2	10	ND	ND	4.5781	ND	ND	ND

	LOD	% Unc.	G32415	G32416	G32417	G32418	G32419	G32420
As	1.8	2	15.4782	151.5713	12.9968	638.9791	386.7446	ND
La	0.08	2	9.3738	0.593	0.4302	0.2951	0.0837	0.0985
Lu	0.03	5	0.1666	0.0435	ND	ND	ND	ND
Nd	6	10	7.3841	ND	ND	ND	ND	ND
Sm	0.05	2	1.561	0.2787	0.0657	0.4502	ND	ND
U	0.8	10	2.755	ND	ND	2.7334	ND	ND
Yb	0.18	7	1.105	0.1646	ND	ND	ND	ND
Ce	0.7	2	18.268	0.9114	0.8623	1.2663	ND	ND
Co	0.02	1	109.5446	0.5277	30.3568	3.2385	6.1079	0.7588
Cr	0.45	10	4.2832	4.1673	2.7933	2.6592	3.576	3.2939
Cs	0.18	15	ND	ND	ND	ND	ND	ND
Eu	0.01	2	0.2071	0.1033	ND	0.0689	0.0076	ND
Fe	1500	0.2	444130.0625	451014.718	440144.3125	443816.875	449858.8438	451354.25
Hf	0.2	3	5.6701	0.1823	ND	ND	ND	ND
Ni	60	20	156.7636	ND	144.453	ND	ND	ND
Rb	7	10	ND	9.4967	ND	ND	ND	ND
Sb	0.05	5	0.1323	1.5712	0.4904	30.7582	0.2776	ND
Sc	0.01	1	0.1741	0.23	0.2275	0.0733	ND	0.0372
Sr	52	15	ND	ND	ND	ND	ND	ND
Ta	0.06	20	0.4899	ND	ND	ND	ND	ND
Tb	0.12	15	ND	ND	ND	ND	ND	ND
Th	0.1	10	5.581	0.3214	0.1319	0.2337	ND	ND
Zn	4	7	ND	7.587	9.4091	6.3327	40.0544	ND
Zr	42	20	112.1028	ND	ND	ND	ND	ND
Al	500	25	620.1352	621.4316	1529.9946	ND	423.7297	507.8
Ba	40	30	34.115	ND	47.25	ND	ND	14.59
Dy	0.2	10	1.4221	0.2412	ND	0.3466	ND	ND
K	400	20	316.2916	ND	ND	ND	ND	ND
Mn	0.2	3	3.8392	5.8862	796.2525	13.5125	4.4211	10.23
Na	10	5	46.2948	36.6665	159.5727	45.5524	22.4118	65.22
V	2	10	2.0191	ND	ND	20.6997	ND	0.98

	LOD	% Unc.	G32421	G32422	G32423	G32424	G32425	G32426
As	1.8	2	1.7663	3841.7019	59.4456	3.4415	ND	8710.8105
La	0.08	2	ND	ND	3.199	0.0517	0.183	ND
Lu	0.03	5	ND	ND	ND	ND	ND	ND
Nd	6	10	ND	ND	ND	ND	ND	ND
Sm	0.05	2	ND	ND	0.4069	ND	ND	ND
U	0.8	10	ND	ND	ND	ND	ND	ND
Yb	0.18	7	ND	ND	ND	ND	ND	ND
Ce	0.7	2	ND	ND	4.7178	ND	ND	ND
Co	0.02	1	11.0572	4.0562	12.1795	2.6289	46.1029	18.8537
Cr	0.45	10	2.7229	2.4512	5.1254	2.4415	2.405	3.3543
Cs	0.18	15	ND	ND	0.4125	ND	ND	ND
Eu	0.01	2	ND	ND	0.1103	ND	ND	ND
Fe	1500	0.2	453223.4063	444872.625	440740.625	451248.4688	451273.7188	443272.9063
Hf	0.2	3	ND	ND	0.2474	ND	ND	ND
Ni	60	20	ND	236.1233	ND	ND	ND	ND
Rb	7	10	ND	ND	ND	ND	ND	ND
Sb	0.05	5	0.4036	35.5695	9.6455	60.6252	ND	2.5277
Sc	0.01	1	ND	ND	0.5086	ND	ND	ND
Sr	52	15	ND	ND	ND	ND	ND	ND
Ta	0.06	20	ND	ND	0.2709	ND	ND	ND
Tb	0.12	15	ND	ND	ND	ND	ND	ND
Th	0.1	10	ND	ND	0.3333	ND	ND	ND
Zn	4	7	ND	404.6434	8.8492	ND	6.2751	ND
Zr	42	20	ND	ND	ND	ND	ND	ND
Al	500	25	357.2249	883.6827	675.2311	ND	ND	600.8253
Ba	40	30	ND	ND	ND	ND	ND	ND
Dy	0.2	10	ND	ND	ND	ND	ND	ND
K	400	20	163.5054	ND	ND	ND	ND	ND
Mn	0.2	3	3.1521	3.1479	4.4833	6.9167	469.7507	4.6345
Na	10	5	25.9379	31.0876	39.9655	48.8181	27.8143	41.6593
V	2	10	ND	ND	3.0854	ND	ND	1.9371

	LOD	% Unc.	G32427	G32428	G32429	G32430	G32706	G33033
As	1.8	2	535.705	77.1348	15.1584	2.2908	45.819	1.9637
La	0.08	2	2.542	ND	2.1314	0.0781	0.1396	16.1252
Lu	0.03	5	ND	ND	ND	ND	ND	0.2099
Nd	6	10	ND	ND	ND	ND	ND	13.2003
Sm	0.05	2	0.5921	ND	0.185	ND	0.1793	2.7294
U	0.8	10	1.0621	ND	ND	ND	ND	2.9774
Yb	0.18	7	ND	ND	ND	ND	ND	1.2034
Ce	0.7	2	4.1075	ND	3.839	ND	ND	31.7841
Co	0.02	1	2.5483	183.4949	10.2546	22.2028	765.4335	210.3412
Cr	0.45	10	3.1075	2.6157	3.0642	3.9106	2.0807	30.5777
Cs	0.18	15	0.48	ND	ND	ND	ND	0.2392
Eu	0.01	2	0.2348	ND	0.0279	ND	0.1066	0.6997
Fe	1500	0.2	437679.1875	447303.937	448015.4063	450078.4688	385787.4063	428774.5
Hf	0.2	3	ND	ND	ND	ND	ND	1.9157
Ni	60	20	ND	117.517	ND	ND	ND	578.4052
Rb	7	10	ND	ND	ND	ND	ND	ND
Sb	0.05	5	4.9675	ND	0.0278	0.3349	1.0424	2.8728
Sc	0.01	1	0.4538	ND	0.1081	ND	0.4376	1.0798
Sr	52	15	ND	ND	ND	ND	ND	ND
Ta	0.06	20	ND	ND	ND	0.0632	ND	0.7945
Tb	0.12	15	ND	ND	ND	ND	ND	0.4019
Th	0.1	10	0.3362	ND	0.1165	ND	ND	8.3971
Zn	4	7	1151.7219	4.2095	11.0146	ND	3758.0381	42.9624
Zr	42	20	ND	ND	ND	ND	ND	64.679
Al	500	25	1277.0546	286.5821	254.1241	544.7517	18560.7012	10731.6797
Ba	40	30	35.3135	ND	ND	ND	1790.2263	30.7355
Dy	0.2	10	0.2404	ND	0.0898	ND	0.2367	2.1026
K	400	20	1207.1993	ND	ND	ND	7332.4346	894.5101
Mn	0.2	3	41.3311	16.3174	3.7481	4.1559	214.5963	55.869
Na	10	5	47.8767	46.4161	31.9128	44.4205	1400.9414	256.2626
V	2	10	ND	ND	ND	ND	19.5591	13.3293

	LOD	% Unc.	G33797	G33823	G6876	G9699
As	1.8	2	48.631	5.7306	110.1857	557.328
La	0.08	2	ND	0.121	ND	ND
Lu	0.03	5	ND	ND	ND	ND
Nd	6	10	ND	ND	ND	ND
Sm	0.05	2	ND	ND	ND	ND
U	0.8	10	ND	ND	ND	ND
Yb	0.18	7	0.1086	ND	ND	ND
Ce	0.7	2	ND	ND	ND	ND
Co	0.02	1	0.9538	1.6152	59.4238	2242.0747
Cr	0.45	10	1.8198	2.783	2.4992	ND
Cs	0.18	15	ND	ND	ND	ND
Eu	0.01	2	ND	ND	ND	ND
Fe	1500	0.2	433588.0938	425699.531	448737.5625	456925.8125
Hf	0.2	3	ND	ND	ND	ND
Ni	60	20	ND	ND	ND	2746.4165
Rb	7	10	ND	ND	ND	ND
Sb	0.05	5	12.6253	1.2438	ND	3.8741
Sc	0.01	1	ND	0.047	ND	0.0637
Sr	52	15	ND	ND	ND	ND
Ta	0.06	20	ND	ND	ND	ND
Tb	0.12	15	ND	ND	ND	ND
Th	0.1	10	ND	ND	ND	ND
Zn	4	7	180.485	ND	ND	ND
Zr	42	20	ND	ND	ND	ND
Al	500	25	338.3399	406.8911	330.3231	ND
Ba	40	30	ND	ND	ND	14.0753
Dy	0.2	10	ND	ND	ND	ND
K	400	20	ND	ND	ND	ND
Mn	0.2	3	4.3147	14.0038	3.1381	7.1074
Na	10	5	45.9249	100.7771	41.6884	191.9895
V	2	10	ND	1.2475	ND	ND

ANSTO Analysis:

Element	G11641			G18915			G20974		
	Conc.	Unc.	LOD	Conc.	Unc.	LOD	Conc.	Unc.	LOD
Ag	ND	ND	4.728	ND	ND	4.2	3.489	0.347	1.866
Al	408	14.41	1.318	6.067	0.4444	0.856	2827	99.43	3.181
Ar	ND	ND	1.739	ND	ND	0.9132	ND	ND	0.6312
As	5.64	0.2988	0.4715	2.871	0.19	0.7605	252.4	8.984	0.5302
Au	0.01269	0.002311	0.008987	ND	ND	0.01408	ND	ND	0.004834
Ba	ND	ND	23.05	ND	ND	9.538	15.31	1.343	0.1188
Br	ND	ND	0.6877	ND	ND	1.073	ND	ND	0.5284
Ca	186.7	33.62	85.68	ND	ND	9.408	198.1	18.74	41.16
Cd	ND	ND	8.979	ND	ND	13.69	ND	ND	11.12
Ce	ND	ND	2.214	ND	ND	3.741	2.094	0.2368	0.05281
Cl	16.13	1.774	5.014	121.5	5.573	4.194	68.03	2.686	3.214
Co	1486	52.11	0.2548	2465	101.9	0.4285	3.888	0.2308	0.08802
Cr	56.22	2.331	4.566	ND	ND	5.999	13.35	0.6763	1.866
Cs	ND	ND	0.874	ND	ND	1.055	ND	ND	0.3559
Cu	409	15.84	3.046	ND	ND	0.6429	113	5.207	2.561
Dy	ND	ND	0.1167	ND	ND	0.02144	0.1408	0.008178	0.02308
Er	ND	ND	3.657	ND	ND	1.038	ND	ND	3.825
Eu	ND	ND	0.01636	ND	ND	0.005599	0.03349	0.001498	0.02822
F	ND	ND	ND	ND	ND	ND	ND	ND	ND
Fe	451300	15800	253.3	456100	15970	442.4	447800	15700	99.88
Ga	ND	ND	9.802	ND	ND	5.061	2.344	0.5425	ND
Gd	ND	ND	3.05	ND	ND	4.107	ND	ND	1.991
Ge	ND	ND	446.5	ND	ND	171.6	ND	ND	99.24
Hf	ND	ND	0.4205	ND	ND	0.7022	0.2467	0.03526	0.1431
Hg	ND	ND	1.278	ND	ND	4.108	ND	ND	0.5698
Ho	ND	ND	0.2505	ND	ND	0.4199	ND	ND	0.3816
I	ND	ND	1.883	ND	ND	0.7571	ND	ND	0.3992
In	ND	ND	0.029	ND	ND	0.01142	ND	ND	0.008511
Ir	ND	ND	0.1446	ND	ND	0.2077	ND	ND	1.002
K	ND	ND	74.18	56.31	9.508	23.59	903.2	82.18	76.52
La	ND	ND	0.03355	ND	ND	0.07053	1.412	0.05695	0.01778
Lu	ND	ND	1.67	ND	ND	0.4113	ND	ND	0.7956
Mg	ND	ND	124.2	853.1	34.32	57.76	168.2	22.11	27.45
Mn	88.05	3.129	0.1662	2.047	0.07867	0.05584	7.671	0.2753	0.04358
Mo	ND	ND	6.848	ND	ND	11.08	20	3.079	0.5804
Na	ND	ND	ND	166.4	7.209	ND	229	9.241	ND
Nb	ND	ND	388.7	ND	ND	216.7	ND	ND	118.4
Nd	ND	ND	6.853	ND	ND	11.75	ND	ND	2.934
Ni	ND	ND	847.7	592.5	41.99	91.56	ND	ND	283.8
Os	ND	ND	0.5754	ND	ND	0.9792	ND	ND	0.2369
Pd	ND	ND	21.46	ND	ND	7.816	ND	ND	4050
Pr	ND	ND	2.359	ND	ND	4.988	ND	ND	4.775
Pt	ND	ND	4.332	ND	ND	6.958	ND	ND	4.872
Rb	ND	ND	39.7	ND	ND	75.96	109.1	5.922	9.32
Re	ND	ND	0.1009	ND	ND	0.1498	ND	ND	0.1124
Rh	ND	ND	4.47	ND	ND	2.166	ND	ND	3.613
Ru	ND	ND	3.348	ND	ND	5.339	ND	ND	1.345
Sb	3.169	0.1312	0.1442	ND	ND	0.2525	34.24	1.202	0.06218
Sc	ND	ND	0.06525	ND	ND	0.1213	0.5821	0.02281	0.006126
Se	8.606	0.7773	3.505	42.17	1.868	5.828	41.18	1.471	1.436
Si	ND	ND	ND	ND	ND	171700	ND	ND	208200
Sm	ND	ND	0.02216	ND	ND	0.03694	0.1671	0.03092	0.02835
Sn	ND	ND	139.2	ND	ND	58.32	ND	ND	31.96
Sr	ND	ND	37.22	ND	ND	7.179	ND	ND	4.078
Ta	ND	ND	0.5344	ND	ND	0.8894	ND	ND	0.2249
Tb	ND	ND	0.1506	ND	ND	0.3002	ND	ND	0.1163
Te	ND	ND	11.95	ND	ND	18.59	ND	ND	5.294
Th	ND	ND	0.4591	ND	ND	0.7409	0.5841	0.08403	0.1874
Ti	ND	ND	52.24	ND	ND	26.35	282.2	11.75	20.63
Tm	ND	ND	0.5683	ND	ND	1.46	ND	ND	0.4076
U	ND	ND	0.7029	ND	ND	1.156	0.7317	0.0679	0.2378
V	25.43	0.963	0.1167	0.07515	0.01414	0.04839	15.57	0.56	0.127
W	ND	ND	0.8669	ND	ND	1.255	ND	ND	1.053
Y	ND	ND	1640	ND	ND	327.4	ND	ND	562.2
Yb	ND	ND	0.2907	ND	ND	0.4603	ND	ND	0.2516
Zn	ND	ND	43.06	ND	ND	7407	ND	ND	26560
Zr	ND	ND	519.9	ND	ND	36.35	ND	ND	211.2

Element	G29982			G32406			G32407		
	Conc.	Unc.	LOD	Conc.	Unc.	LOD	Conc.	Unc.	LOD
Ag	ND	ND	1.243	ND	ND	1.427	51.29	1.88	1.296
Al	1281	45.15	1.623	123.7	4.471	0.4451	8.746	0.592	1.691
Ar	ND	ND	0.4868	ND	ND	0.387	ND	ND	2.256
As	1.847	0.09201	0.2174	587.1	20.77	0.6443	18.19	0.6519	0.3142
Au	ND	ND	0.003774	ND	ND	0.008675	ND	ND	0.006208
Ba	4.173	0.9204	3.512	ND	ND	2.975	ND	ND	39.78
Br	ND	ND	0.3412	ND	ND	0.5941	4.187	0.1672	0.4277
Ca	444.6	28.4	42.85	89.55	18.8	59.84	ND	ND	135.2
Cd	ND	ND	3.935	ND	ND	19.81	92.75	3.707	6.207
Ce	4.048	0.2516	0.87	ND	ND	0.6742	ND	ND	0.8983
Cl	4.523	0.6835	2.758	10.14	0.7443	2.291	203.2	7.862	10.19
Co	6.473	0.2417	0.06678	322.5	11.29	0.127	18.76	0.7805	0.08825
Cr	3.612	0.482	1.787	ND	ND	1.693	ND	ND	1.451
Cs	ND	ND	0.3802	ND	ND	0.4638	ND	ND	0.4006
Cu	ND	ND	0.7302	ND	ND	0.9093	29.6	2.145	3.387
Dy	0.127	0.006432	0.01824	0.08438	0.009793	0.02007	ND	ND	0.1772
Er	ND	ND	1.041	ND	ND	2.445	ND	ND	5.425
Eu	0.03389	0.001714	0.006454	0.01709	0.001688	0.009068	ND	ND	0.02209
F	ND	ND	ND	ND	ND	ND	ND	ND	ND
Fe	420200	14710	99.63	443000	15510	123.4	434900	15220	105.6
Ga	ND	ND	1.787	ND	ND	1.872	ND	ND	12.75
Gd	ND	ND	3.446	ND	ND	0.9985	ND	ND	3.599
Ge	ND	ND	70.9	ND	ND	91.39	ND	ND	811.7
Hf	0.2567	0.04466	0.1406	ND	ND	0.1643	ND	ND	0.1784
Hg	ND	ND	0.5692	15.3	0.5686	0.7023	ND	ND	0.6052
Ho	ND	ND	0.0358	ND	ND	0.5856	ND	ND	0.1814
I	ND	ND	0.2999	ND	ND	0.339	4.247	1.576	2.089
In	ND	ND	0.00541	ND	ND	0.00786	0.2761	0.01125	0.01944
Ir	ND	ND	0.2071	ND	ND	0.4963	ND	ND	0.1922
K	279.3	14.39	24.35	120.4	10.4	28.45	ND	ND	38.04
La	1.884	0.06811	0.02138	0.4401	0.02928	0.06702	ND	ND	0.01863
Lu	ND	ND	0.4694	ND	ND	0.968	ND	ND	2.645
Mg	132.8	8.067	21.67	ND	ND	23.6	ND	ND	99.51
Mn	4.638	0.1656	0.03476	0.6962	0.03274	0.0213	323.7	11.34	0.2473
Mo	ND	ND	3.033	ND	ND	8.087	ND	ND	5.019
Na	53.23	2.145	0.03507	13.28	0.7697	ND	25.04	2.126	ND
Nb	ND	ND	98.33	ND	ND	78.67	ND	ND	217
Nd	ND	ND	2.433	ND	ND	3.034	ND	ND	2.488
Ni	ND	ND	137.6	ND	ND	126.5	ND	ND	1356
Os	ND	ND	0.2124	ND	ND	0.2621	ND	ND	0.2187
Pd	ND	ND	8.517	ND	ND	5.755	ND	ND	25.51
Pr	ND	ND	0.7458	ND	ND	4.346	ND	ND	1.275
Pt	ND	ND	1.887	ND	ND	7.929	ND	ND	3.158
Rb	ND	ND	14.8	ND	ND	20.43	ND	ND	15.12
Re	ND	ND	0.04471	ND	ND	0.1272	ND	ND	0.07417
Rh	ND	ND	2.624	ND	ND	0.6592	ND	ND	4.684
Ru	ND	ND	1.347	ND	ND	1.668	ND	ND	1.429
Sb	0.2111	0.03137	0.1198	0.9091	0.08861	0.07677	ND	ND	0.1778
Sc	0.2209	0.01244	0.006178	ND	ND	0.0283	ND	ND	0.02619
Se	1.729	0.3159	1.47	33.02	1.184	1.8	ND	ND	1.503
Si	ND	ND	161700	ND	ND	113600	ND	ND	ND
Sm	0.2413	0.009063	0.01009	0.07399	0.04824	0.05033	ND	ND	0.01639
Sn	ND	ND	23.07	ND	ND	28.45	ND	ND	162.5
Sr	ND	ND	7.948	ND	ND	10.28	ND	ND	58.97
Ta	ND	ND	0.2283	ND	ND	0.2824	ND	ND	0.2397
Tb	ND	ND	0.1179	ND	ND	0.1459	ND	ND	0.1255
Te	ND	ND	4.104	ND	ND	5.163	ND	ND	4.209
Th	0.8228	0.05406	0.1788	ND	ND	0.2223	ND	ND	0.1891
Ti	223.6	9.288	15.13	55.31	3.065	8.287	ND	ND	50.15
Tm	ND	ND	0.4149	ND	ND	0.2158	ND	ND	0.4341
U	ND	ND	0.1011	ND	ND	0.4774	ND	ND	0.5201
V	2.7	0.1296	0.07624	0.2921	0.02223	0.02349	2.313	0.09	0.1025
W	ND	ND	0.4134	ND	ND	1.066	ND	ND	0.5743
Y	ND	ND	387.6	ND	ND	511.5	ND	ND	2432
Yb	ND	ND	0.09562	ND	ND	0.3017	ND	ND	0.2041
Zn	ND	ND	13010	ND	ND	3474	6253	219.8	3.924
Zr	ND	ND	90.17	ND	ND	266.7	ND	ND	229.9

Element	G32409			G32410			G32411		
	Conc.	Unc.	LOD	Conc.	Unc.	LOD	Conc.	Unc.	LOD
Ag	ND	ND	1.357	64.65	2.449	1.23	ND	ND	1.752
Al	343.8	12.15	0.5689	12.2	0.6504	1.503	1963	68.83	1.334
Ar	ND	ND	0.4789	ND	ND	2.73	ND	ND	0.6414
As	19.97	0.7455	0.235	17.89	0.6384	0.2782	203.4	7.223	0.4259
Au	ND	ND	0.00473	ND	ND	0.002061	ND	ND	0.009812
Ba	ND	ND	3.315	ND	ND	38.85	37.32	1.954	0.1217
Br	ND	ND	0.3828	3.766	0.1489	0.3776	1.841	0.1127	0.6184
Ca	ND	ND	49.41	ND	ND	113	5716	245.6	65.59
Cd	ND	ND	4.637	ND	ND	5.355	ND	ND	10.96
Ce	ND	ND	0.9639	ND	ND	0.7518	0.9857	0.186	0.05412
Cl	41.49	1.81	2.311	172.4	6.731	8.056	111	4.937	3.853
Co	2.656	0.1137	0.07383	14.9	0.5251	0.07888	0.9943	0.0696	0.06345
Cr	ND	ND	1.535	ND	ND	1.271	3.679	0.4137	1.519
Cs	ND	ND	0.4263	ND	ND	0.3281	ND	ND	0.3158
Cu	ND	ND	0.7086	85.77	4.892	3.335	15.98	2.877	1.023
Dy	0.02179	0.004339	0.0163	ND	ND	0.13	0.04723	0.005971	0.02349
Er	ND	ND	1.179	ND	ND	5.554	ND	ND	1.899
Eu	ND	ND	0.006909	ND	ND	0.02034	0.01166	0.00216	0.009769
F	ND	ND	ND	ND	ND	ND	ND	ND	ND
Fe	451200	15800	111.2	428700	15010	87.03	434000	15190	83.9
Ga	ND	ND	1.656	ND	ND	11.39	ND	ND	2.508
Gd	ND	ND	1.806	ND	ND	2.975	ND	ND	0.7336
Ge	ND	ND	59.53	ND	ND	734.8	ND	ND	108.6
Hf	ND	ND	0.1916	ND	ND	0.1488	ND	ND	0.1108
Hg	1.022	0.08069	0.6331	ND	ND	0.4982	ND	ND	0.8693
Ho	ND	ND	0.1109	ND	ND	0.1556	ND	ND	0.3407
I	ND	ND	0.2439	3.843	0.4229	2.046	ND	ND	0.469
In	ND	ND	0.005829	0.06453	0.005537	0.0186	ND	ND	0.002619
Ir	ND	ND	0.1416	ND	ND	0.1717	ND	ND	0.3613
K	42.11	11.17	24.15	ND	ND	37.1	527.5	33.99	37.47
La	0.06426	0.007423	0.02174	0.592	0.07468	0.01767	0.4241	0.025	0.02065
Lu	ND	ND	0.5239	ND	ND	2.279	ND	ND	0.8307
Mg	ND	ND	21.07	ND	ND	94.32	878.3	36.32	29.79
Mn	1.747	0.08232	0.0367	309.2	10.85	0.2062	13.93	0.4964	0.04668
Mo	57.52	3.586	3.506	ND	ND	4.086	488.4	17.36	0.5955
Na	61.85	2.559	0.02513	24.46	1.994	ND	223.2	8.033	ND
Nb	ND	ND	89.72	ND	ND	207.2	ND	ND	131.3
Nd	ND	ND	2.655	ND	ND	2.162	ND	ND	2.129
Ni	ND	ND	177.9	ND	ND	1054	ND	ND	292.6
Os	ND	ND	0.2338	ND	ND	0.1868	ND	ND	0.1818
Pd	ND	ND	5.678	ND	ND	24.82	ND	ND	13.53
Pr	ND	ND	1.522	ND	ND	1.241	ND	ND	3.966
Pt	ND	ND	2.198	ND	ND	2.571	ND	ND	5.328
Rb	ND	ND	16.34	ND	ND	13.19	67	4.35	7.445
Re	ND	ND	0.05164	ND	ND	0.06005	ND	ND	0.09234
Rh	ND	ND	0.8672	ND	ND	4.769	ND	ND	2.357
Ru	ND	ND	1.497	ND	ND	0.378	ND	ND	0.4583
Sb	4.68	0.1692	0.08342	1.634	0.06703	0.05116	12.87	0.457	0.1511
Sc	0.05966	0.02112	0.00694	ND	ND	0.02241	0.3112	0.0624	0.005215
Se	10.82	0.4834	1.647	ND	ND	1.243	6.87	0.3441	1.221
Si	ND	ND	130900	ND	ND	ND	ND	ND	220400
Sm	0.01796	0.002931	0.0113	ND	ND	0.01355	0.06635	0.007866	0.02948
Sn	ND	ND	20.25	ND	ND	138.9	ND	ND	35.21
Sr	ND	ND	6.811	ND	ND	47.45	175.4	6.82	10.82
Ta	ND	ND	0.2584	ND	ND	0.1989	ND	ND	0.1936
Tb	ND	ND	0.1336	ND	ND	0.1032	ND	ND	0.1002
Te	ND	ND	4.399	ND	ND	3.69	ND	ND	3.6
Th	ND	ND	0.2005	ND	ND	0.1574	0.2208	0.03879	0.1522
Ti	ND	ND	12.19	ND	ND	47.54	118.6	6.862	21.99
Tm	ND	ND	0.4677	ND	ND	0.3418	ND	ND	0.05228
U	ND	ND	0.162	ND	ND	0.4273	0.8498	0.07099	0.2427
V	0.4761	0.02905	0.02853	2.139	0.08381	0.1008	6.191	0.3258	0.1164
W	ND	ND	0.4402	ND	ND	0.51	ND	ND	0.7999
Y	ND	ND	337.2	ND	ND	4034	ND	ND	611
Yb	ND	ND	0.1557	ND	ND	0.1724	ND	ND	0.1599
Zn	ND	ND	4277	90.61	4.262	3.245	ND	ND	12.01
Zr									

Element	G32412			G32413			G32414		
	Conc.	Unc.	LOD	Conc.	Unc.	LOD	Conc.	Unc.	LOD
Ag	ND	ND	0.6654	ND	ND	1.193	ND	ND	1.115
Al	112.6	3.992	0.2366	589	20.73	0.4116	232.4	8.246	0.9599
Ar	ND	ND	0.2967	ND	ND	0.3954	ND	ND	0.1088
As	577.2	20.37	0.6718	4.595	0.1812	0.273	2.711	0.111	0.188
Au	ND	ND	0.01537	0.007553	0.001253	0.004818	0.0977	0.003624	0.003662
Ba	ND	ND	3.795	ND	ND	3.106	ND	ND	38.37
Br	ND	ND	0.4092	ND	ND	0.3331	ND	ND	0.2876
Ca	303.6	27.57	29.39	148.9	18.34	45.6	505.9	33.2	78.63
Cd	ND	ND	18.56	ND	ND	4.785	ND	ND	3.523
Ce	ND	ND	0.8499	0.7611	0.1902	0.03096	ND	ND	0.8269
Cl	4.288	0.4916	1.7	7.927	0.6867	2.227	ND	ND	7.948
Co	0.3963	0.03521	0.08328	5.971	0.263	0.05559	2.607	0.1045	0.05618
Cr	ND	ND	1.391	ND	ND	1.55	ND	ND	1.315
Cs	ND	ND	0.3658	ND	ND	0.3203	ND	ND	0.3658
Cu	ND	ND	0.7472	ND	ND	0.6364	ND	ND	1.801
Dy	0.03338	0.003551	0.01752	0.05868	0.005179	0.01498	ND	ND	0.1817
Er	ND	ND	2.178	ND	ND	0.9962	ND	ND	28.21
Eu	ND	ND	0.007592	0.009054	0.002154	0.00528	ND	ND	0.0177
F	ND	ND	ND	ND	ND	ND	ND	ND	ND
Fe	448800	15720	99.16	454700	15920	85.5	444700	15570	95.76
Ga	ND	ND	1.191	ND	ND	1.488	ND	ND	11.22
Gd	ND	ND	1.045	ND	ND	0.7733	ND	ND	3.317
Ge	ND	ND	22.53	ND	ND	31.51	ND	ND	317
Hf	ND	ND	0.1682	ND	ND	0.1469	ND	ND	0.1643
Hg	ND	ND	0.8996	ND	ND	4.346	ND	ND	2.015
Ho	ND	ND	0.5465	ND	ND	0.148	ND	ND	0.04917
I	ND	ND	0.2643	ND	ND	0.2833	ND	ND	3.41
In	ND	ND	0.004138	ND	ND	0.004793	ND	ND	0.04085
Ir	ND	ND	0.4187	ND	ND	0.1795	ND	ND	0.1029
K	69.99	7.127	19.81	219.6	12.04	21.19	93.27	9.093	24.07
La	0.1899	0.02091	0.06303	0.3528	0.01668	0.003558	0.07764	0.006062	0.01335
Lu	ND	ND	0.1815	ND	ND	0.4648	ND	ND	5.742
Mg	111.9	5.558	15.96	105.4	6.176	18.34	ND	ND	90.88
Mn	1.258	0.049	0.02562	7.115	0.2514	0.02979	307.1	10.79	0.231
Mo	186.6	6.785	6.062	ND	ND	3.746	ND	ND	2.692
Na	4.327	0.4721	ND	6.631	0.5939	ND	23.93	2.098	0.01572
Nb	ND	ND	54.6	ND	ND	76.56	ND	ND	192.4
Nd	ND	ND	2.491	ND	ND	2.195	ND	ND	2.321
Ni	ND	ND	108.1	267	29.59	70.88	ND	ND	1547
Os	ND	ND	0.2132	ND	ND	0.1871	ND	ND	0.2025
Pd	ND	ND	3.713	ND	ND	7.024	ND	ND	15.98
Pr	ND	ND	4.13	ND	ND	1.001	ND	ND	0.7694
Pt	ND	ND	7.045	ND	ND	2.335	ND	ND	1.694
Rb	ND	ND	15.56	63.16	4.396	7.654	ND	ND	14.29
Re	ND	ND	0.111	ND	ND	0.05485	ND	ND	0.04009
Rh	ND	ND	0.3031	ND	ND	0.5581	ND	ND	3.733
Ru	ND	ND	1.335	ND	ND	1.152	ND	ND	1.301
Sb	30.41	1.069	0.2213	0.2779	0.03857	0.1457	0.4443	0.05248	0.1102
Sc	ND	ND	0.005393	0.2057	0.01159	0.005288	0.2864	0.01342	0.005949
Se	7.661	0.3964	1.447	36.89	1.319	1.268	15.04	0.5952	1.42
Si	ND	ND	85790	ND	ND	130900	ND	ND	ND
Sm	ND	ND	0.04694	0.03714	0.003549	0.0127	0.01266	0.002245	0.008718
Sn	ND	ND	22.81	ND	ND	18.66	ND	ND	150.2
Sr	ND	ND	8.065	ND	ND	6.724	ND	ND	88.51
Ta	ND	ND	0.2248	ND	ND	0.1961	ND	ND	0.2218
Tb	ND	ND	0.1171	ND	ND	0.101	ND	ND	0.1142
Te	ND	ND	4.32	ND	ND	3.66	ND	ND	3.885
Th	ND	ND	0.06725	0.2432	0.03972	0.1552	ND	ND	0.1725
Ti	8.652	1.683	6.393	70.26	3.445	10.68	ND	ND	41.41
Tm	ND	ND	0.4066	ND	ND	0.1189	ND	ND	0.4009
U	ND	ND	0.1635	ND	ND	0.1446	ND	ND	0.2885
V	0.2064	0.01368	0.0147	2.442	0.09015	0.03828	0.7565	0.04185	0.09448
W	ND	ND	0.9312	ND	ND	0.4968	ND	ND	0.3404
Y	ND	ND	427	ND	ND	349.6	ND	ND	3954
Yb	ND	ND	0.2427	ND	ND	0.06181	ND	ND	0.1197
Zn	ND	ND	2023	33.14	3.085	3.196	ND	ND	8.102
Zr	ND	ND	211.6	ND	ND	187.2	ND	ND	211.4

Element	G32415			G32416			G32417		
	Conc.	Unc.	LOD	Conc.	Unc.	LOD	Conc.	Unc.	LOD
Ag	ND	ND	1.022	1.309	0.1924	0.9408	ND	ND	1.524
Al	176.9	6.432	0.3784	224.1	7.912	0.3818	1062	37.56	3.122
Ar	ND	ND	0.3712	ND	ND	0.474	ND	ND	9.477
As	22.59	0.8063	0.3322	209.2	7.362	0.37	11.71	0.4214	0.2352
Au	ND	ND	0.006284	0.04181	0.00237	0.007394	ND	ND	0.004576
Ba	6.236	1.048	0.1046	ND	ND	4.756	ND	ND	41.6
Br	ND	ND	0.4932	ND	ND	0.5076	ND	ND	0.3431
Ca	347.8	23.52	52.19	95.11	17.19	45.37	1617	180.9	183.4
Cd	ND	ND	6.761	ND	ND	8.458	ND	ND	4.605
Ce	11.98	0.725	0.04649	1.073	0.1977	0.7776	3.28	0.2622	0.9894
Cl	4.89	0.5677	1.517	14.5	0.9163	2.252	ND	ND	32.08
Co	211.6	11.92	0.1197	1.146	0.04634	0.05391	36.16	1.28	0.102
Cr	ND	ND	2.06	ND	ND	1.583	ND	ND	2.046
Cs	ND	ND	0.4339	ND	ND	0.3277	ND	ND	0.4344
Cu	23.2	1.39	1.562	7.376	1.287	1.058	130.4	8.993	2.638
Dy	1.08	0.03858	0.02067	0.1017	0.01171	0.0212	ND	ND	0.5666
Er	ND	ND	2.323	ND	ND	2.183	ND	ND	135.9
Eu	0.1294	0.005488	0.0147	0.02571	0.001767	0.01044	0.0871	0.006136	0.0251
F	ND	ND	ND	ND	ND	ND	ND	ND	ND
Fe	470800	16510	115.4	447400	15660	87.09	455900	15990	113.5
Ga	ND	ND	1.788	ND	ND	1.653	ND	ND	48.99
Gd	ND	ND	1.421	ND	ND	1.71	ND	ND	3.901
Ge	ND	ND	64.24	ND	ND	32.08	ND	ND	614
Hf	4.259	0.1926	0.1619	ND	ND	0.1508	ND	ND	0.1943
Hg	ND	ND	0.8766	ND	ND	0.5006	ND	ND	0.6555
Ho	0.3694	0.05371	0.2051	ND	ND	0.247	ND	ND	0.1303
I	ND	ND	0.2625	ND	ND	0.4416	ND	ND	15.12
In	ND	ND	0.005837	0.02472	0.001654	0.002421	ND	ND	0.074
Ir	ND	ND	0.1951	ND	ND	0.2288	ND	ND	0.6992
K	216.7	16.43	46.97	ND	ND	45.25	463.3	26.16	50.59
La	5.385	0.1921	0.03652	0.2533	0.02994	0.03028	1.027	0.03894	0.02592
Lu	ND	ND	0.3086	ND	ND	0.6777	ND	ND	31.16
Mg	111.2	6.142	19.19	422.8	36.47	34.05	ND	ND	388.6
Mn	0.4928	0.02135	0.03158	13.36	0.4704	0.03588	1168	40.96	0.8173
Mo	7.636	1.457	0.526	ND	ND	6.175	ND	ND	3.508
Na	7.445	0.5918	ND	8.397	0.6105	ND	86.02	8.352	0.03348
Nb	ND	ND	90.95	ND	ND	91.63	ND	ND	788.1
Nd	5.411	1.59	0.0416	ND	ND	2.257	ND	ND	2.786
Ni	260	34.23	82.74	ND	ND	191.2	ND	ND	6482
Os	ND	ND	0.2469	ND	ND	0.1929	ND	ND	0.2418
Pd	ND	ND	6.353	ND	ND	5.784	ND	ND	22.24
Pr	ND	ND	1.389	ND	ND	1.917	ND	ND	1.663
Pt	ND	ND	3.447	ND	ND	3.844	ND	ND	2.188
Rb	ND	ND	17.6	ND	ND	12.73	80.84	5.87	10.03
Re	0.1221	0.02934	0.08324	ND	ND	0.09033	ND	ND	0.05221
Rh	ND	ND	0.5552	ND	ND	0.5533	ND	ND	9.408
Ru	210.3	14.64	19.58	ND	ND	22.1	ND	ND	0.7857
Sb	ND	ND	0.06929	2.178	0.08829	0.05148	0.6135	0.04214	0.1365
Sc	0.1234	0.01538	0.007326	0.1164	0.01377	0.005383	0.5271	0.02096	0.007007
Se	6.064	0.3005	1.694	ND	ND	0.7609	ND	ND	1.628
Si	ND	ND	104900	ND	ND	132000	ND	ND	ND
Sm	0.8919	0.0328	0.0189	0.05814	0.005705	0.02083	0.3638	0.03086	0.01156
Sn	ND	ND	22.73	ND	ND	30.1	ND	ND	179.6
Sr	ND	ND	6.383	ND	ND	10.2	ND	ND	177.5
Ta	ND	ND	0.1992	ND	ND	0.199	ND	ND	0.2612
Tb	0.1896	0.03477	0.1366	ND	ND	0.1037	ND	ND	0.1359
Te	ND	ND	4.591	ND	ND	3.859	ND	ND	4.721
Th	3.987	0.1565	0.2069	0.2804	0.04093	0.1587	ND	ND	0.1367
Ti	1272	44.97	9.214	123.5	5.391	9.765	ND	ND	101.1
Tm	ND	ND	0.2183	ND	ND	0.3609	ND	ND	0.4719
U	1.974	0.1185	0.2121	ND	ND	0.2254	ND	ND	0.3848
V	0.8543	0.0362	0.02139	1.863	0.07128	0.02487	1.924	0.1397	0.3506
W	ND	ND	0.2386	7.098	0.2761	0.652	ND	ND	0.4352
Y	ND	ND	393	ND	ND	516.1	ND	ND	22200
Yb	0.7628	0.05031	0.2047	ND	ND	0.2147	ND	ND	0.09077
Zn	ND	ND	2929	15.61	2.817	3.256	ND	ND	38130
Zr									

Element	G32418			G32419			G32420		
	Conc.	Unc.	LOD	Conc.	Unc.	LOD	Conc.	Unc.	LOD
Ag	3.097	0.3059	1.507	66.41	2.346	0.7281	ND	ND	0.8028
Al	13.29	0.5232	0.3687	29.61	1.072	0.2303	118.9	4.229	0.2655
Ar	ND	ND	0.9215	ND	ND	0.7187	ND	ND	0.4681
As	262.9	9.242	1.267	396.4	14.32	0.5965	0.8488	0.08834	0.3072
Au	ND	ND	0.03669	0.03985	0.003014	0.01332	0.01317	0.001517	0.005568
Ba	ND	ND	17.92	ND	ND	8.322	ND	ND	3.856
Br	ND	ND	1.192	ND	ND	0.8154	ND	ND	0.3767
Ca	3247	135.6	86	ND	ND	25.38	ND	ND	42.82
Cd	ND	ND	40.33	ND	ND	15.71	ND	ND	5.273
Ce	ND	ND	0.1581	ND	ND	0.8569	ND	ND	0.8189
Cl	21.58	1.388	4.627	13.34	0.8902	2.864	9.04	1.021	2.539
Co	5.77	0.2168	0.08018	20.73	1.493	0.09342	0.6221	0.02958	0.05571
Cr	ND	ND	2.022	ND	ND	1.368	ND	ND	0.03809
Cs	ND	ND	0.386	ND	ND	0.3833	ND	ND	0.3669
Cu	1559	54.96	7.898	ND	ND	2.982	ND	ND	1.656
Dy	0.6083	0.02985	0.04936	0.03431	0.004	0.0169	ND	ND	0.01138
Er	ND	ND	13.62	ND	ND	6.104	ND	ND	2.695
Eu	0.1279	0.009025	0.02713	ND	ND	0.006813	ND	ND	0.0122
F	ND	ND	ND	ND	ND	37710	ND	ND	178200
Fe	445000	15580	108.9	460300	16120	100.6	458400	16060	95.35
Ga	12.84	21.38	ND	ND	ND	4.119	ND	ND	1.936
Gd	ND	ND	5.396	ND	ND	1.676	ND	ND	1.115
Ge	ND	ND	124.6	ND	ND	16.22	ND	ND	11.31
Hf	186.3	39.14	135.3	ND	ND	0.1705	ND	ND	0.1628
Hg	ND	ND	114.4	ND	ND	0.5752	ND	ND	0.652
Ho	ND	ND	1.498	ND	ND	0.4653	ND	ND	0.1658
I	ND	ND	1.227	ND	ND	0.6693	ND	ND	0.2962
In	0.02721	0.003678	0.00787	1.958	0.06884	0.003351	ND	ND	0.00712
Ir	ND	ND	1.302	ND	ND	0.499	ND	ND	0.1731
K	ND	ND	148.7	ND	ND	108.6	54.47	11.63	36.56
La	ND	ND	0.06703	ND	ND	0.04699	0.05427	0.006652	0.01511
Lu	ND	ND	2.918	ND	ND	1.25	ND	ND	0.5638
Mg	468.4	25.2	57.4	464.6	20.88	29.83	ND	ND	24.06
Mn	9.764	0.3634	0.08957	19.76	0.6942	0.07647	3.712	0.1353	0.04535
Mo	50.12	7.808	1.859	ND	ND	11.55	ND	ND	4.342
Na	14.4	2.68	ND	9.518	0.6882	ND	23.72	1.487	ND
Nb	ND	ND	261.4	ND	ND	85.49	ND	ND	78.01
Nd	51.14	12.77	0.1488	ND	ND	2.347	ND	ND	2.258
Ni	ND	ND	323.7	ND	ND	266	ND	ND	150.5
Os	ND	ND	0.2612	ND	ND	0.207	ND	ND	0.1987
Pd	ND	ND	19.72	ND	ND	6.908	ND	ND	3.795
Pr	ND	ND	4.566	ND	ND	3.426	ND	ND	1.271
Pt	ND	ND	14.41	ND	ND	5.29	ND	ND	2.713
Rb	ND	ND	17.26	ND	ND	14.62	ND	ND	14.11
Re	ND	ND	0.2061	ND	ND	0.0876	ND	ND	0.06368
Rh	ND	ND	1.06	ND	ND	0.2582	ND	ND	0.2096
Ru	ND	ND	1.461	ND	ND	1.356	ND	ND	1.29
Sb	12.07	0.7466	0.1909	1.003	0.08796	0.06268	ND	ND	0.06106
Sc	0.172	0.0309	0.006709	ND	ND	0.003926	0.1296	0.009816	0.0059
Se	45.59	1.782	1.577	ND	ND	1.038	2.015	0.36	1.413
Si	ND	ND	ND	ND	ND	232700	ND	ND	135500
Sm	0.5046	0.07581	0.1149	ND	ND	0.04069	ND	ND	0.01439
Sn	148.2	19.74	66.55	ND	ND	50.22	ND	ND	23.36
Sr	ND	ND	34.25	ND	ND	18.06	ND	ND	7.984
Ta	ND	ND	0.2471	ND	ND	0.2313	ND	ND	0.2197
Tb	ND	ND	0.0562	ND	ND	0.1197	ND	ND	0.1143
Te	ND	ND	0.9611	ND	ND	2.451	ND	ND	3.754
Th	0.8265	0.05927	0.2029	ND	ND	0.1793	ND	ND	0.1714
Ti	50.99	4.751	17.06	ND	ND	13.83	10.73	2.067	7.757
Tm	ND	ND	0.4469	ND	ND	0.1656	ND	ND	0.3976
U	10.13	0.6282	0.8242	ND	ND	0.3985	ND	ND	0.1743
V	47.01	1.648	0.03109	0.4469	0.02624	0.02494	0.4798	0.02766	0.01555
W	1520	54.1	2.006	1.171	0.2522	0.9821	ND	ND	0.5622
Y	ND	ND	1847	ND	ND	920.3	ND	ND	411.5
Yb	ND	ND	0.1929	ND	ND	0.2157	ND	ND	0.177
Zn	ND	ND	14.49	355.2	13.24	3.773	ND	ND	2243
Zr	ND	ND	130.2	ND	ND	217.8	ND	ND	210.6

Element	G32421			G32422			G32423		
	Conc.	Unc.	LOD	Conc.	Unc.	LOD	Conc.	Unc.	LOD
Ag	ND	ND	0.5771	13.78	0.9113	1.741	ND	ND	1.989
Al	33.52	1.237	0.2132	6.289	0.4199	0.9029	741.3	28.39	13.81
Ar	ND	ND	0.3373	ND	ND	0.6998	ND	ND	0.5825
As	1.619	0.1063	0.3173	2341	82.45	1.561	71.87	2.528	0.3563
Au	0.01935	0.001664	0.005733	0.06733	0.005629	0.03312	ND	ND	0.007463
Ba	ND	ND	3.038	ND	ND	5.669	18.02	1.52	5.122
Br	ND	ND	0.341	ND	ND	1.269	ND	ND	0.5257
Ca	ND	ND	37.87	ND	ND	52.58	ND	ND	37
Cd	ND	ND	5.539	ND	ND	44.25	ND	ND	8.265
Ce	ND	ND	0.8576	ND	ND	0.8947	5.748	0.3146	0.8711
Cl	15.05	0.8329	1.678	7.987	0.7996	3.036	6.709	0.731	2.504
Co	10.72	0.6996	0.06451	5.45	0.2214	0.08312	12.93	0.7903	0.09233
Cr	ND	ND	0.9992	ND	ND	0.7382	3.379	0.4855	1.833
Cs	ND	ND	0.3627	ND	ND	0.372	1.708	0.09763	0.3537
Cu	63.53	2.953	1.576	301.4	11.11	4.305	10.65	2.435	2.409
Dy	ND	ND	0.01388	ND	ND	0.04713	0.1959	0.009977	0.02497
Er	ND	ND	1.799	ND	ND	7.658	ND	ND	4.084
Eu	ND	ND	0.01791	ND	ND	0.03048	0.105	0.005228	0.0201
F	ND	ND	ND	ND	ND	ND	ND	ND	ND
Fe	443800	15700	98.23	467000	16350	103	444700	15580	98.87
Ga	ND	ND	1.307	ND	ND	4.605	ND	ND	2.068
Gd	ND	ND	3.282	ND	ND	3.178	ND	ND	3.303
Ge	ND	ND	19.42	ND	ND	197.9	ND	ND	107.7
Hf	ND	ND	0.1682	ND	ND	0.1756	0.2974	0.0414	0.1386
Hg	ND	ND	2.156	ND	ND	0.6338	4.141	0.2034	0.5615
Ho	ND	ND	0.1747	ND	ND	1.373	ND	ND	0.1723
I	ND	ND	0.1862	ND	ND	0.7525	ND	ND	0.4468
In	ND	ND	4.883	2.063	0.07241	0.005102	ND	ND	0.005297
Ir	ND	ND	0.1842	ND	ND	1.46	ND	ND	0.651
K	ND	ND	32.71	ND	ND	143.4	83.56	21.03	76.71
La	0.07176	0.00756	0.01532	ND	ND	0.1348	3.42	0.1232	0.02904
Lu	ND	ND	0.4519	ND	ND	1.5	ND	ND	0.8335
Mg	ND	ND	16.81	ND	ND	50.99	ND	ND	25.5
Mn	1.392	0.0518	0.02525	1.282	0.05055	0.08331	21.39	0.7549	0.04169
Mo	ND	ND	4.143	ND	ND	17.51	ND	ND	6.13
Na	4.633	0.4479	ND	6.42	0.6674	ND	12.36	0.7965	ND
Nb	ND	ND	42.4	ND	ND	122.3	ND	ND	102.1
Nd	ND	ND	2.656	ND	ND	2.803	ND	ND	2.648
Ni	ND	ND	94.8	ND	ND	168.1	ND	ND	242.6
Os	ND	ND	0.2222	ND	ND	0.2332	ND	ND	0.2252
Pd	ND	ND	2.664	ND	ND	10.09	ND	ND	17.79
Pr	ND	ND	1.007	ND	ND	10.32	ND	ND	2.229
Pt	ND	ND	2.815	ND	ND	10.09	ND	ND	3.811
Rb	75.21	5.217	9.054	ND	ND	16.36	ND	ND	15.39
Re	ND	ND	0.06591	ND	ND	0.1526	ND	ND	0.08963
Rh	ND	ND	0.2812	ND	ND	1.374	ND	ND	4.361
Ru	ND	ND	1.327	ND	ND	1.383	ND	ND	1.319
Sb	0.3578	0.05073	0.06499	28.86	1.049	0.2293	34.49	1.212	0.1841
Sc	ND	ND	0.02496	ND	ND	0.02635	0.686	0.04272	0.005998
Se	16.54	0.6449	1.42	6.308	0.4727	1.474	ND	ND	1.47
Si	ND	ND	94390	ND	ND	231600	ND	ND	188800
Sm	ND	ND	0.01497	ND	ND	0.1173	0.4312	0.02041	0.02066
Sn	ND	ND	18.04	290.9	12.86	48.96	ND	ND	33.94
Sr	ND	ND	5.27	ND	ND	22.78	ND	ND	9.62
Ta	ND	ND	0.2211	ND	ND	0.2303	ND	ND	0.2213
Tb	ND	ND	0.1148	ND	ND	0.1208	ND	ND	0.051
Te	ND	ND	4.706	ND	ND	5.042	ND	ND	4.899
Th	ND	ND	0.1804	ND	ND	0.1906	0.3826	0.04775	0.1826
Ti	ND	ND	5.277	ND	ND	18.83	967	35.33	21.32
Tm	ND	ND	0.3991	ND	ND	0.4167	ND	ND	0.4006
U	ND	ND	0.1489	ND	ND	0.475	ND	ND	0.2654
V	0.03374	0.007691	0.01064	ND	ND	0.05071	7.949	0.3033	0.1329
W	ND	ND	0.5768	ND	ND	1.664	8.713	0.3366	0.6951
Y	ND	ND	290.2	ND	ND	1117	ND	ND	610.8
Yb	ND	ND	0.1903	ND	ND	0.2546	ND	ND	0.2445
Zn	ND	ND	13.78	579.4	20.68	3.717	16.58	3.057	3.6
Zr	ND	ND	213.7	ND	ND	218.3	ND	ND	208.1

Element	G32424			G32425			G32426		
	Conc.	Unc.	LOD	Conc.	Unc.	LOD	Conc.	Unc.	LOD
Ag	3.274	1.266	2.016	ND	ND	1.437	126.7	4.454	0.7021
Al	410.4	14.42	0.4487	232.7	8.434	1.744	6.015	0.2742	0.2807
Ar	ND	ND	1.804	ND	ND	5.493	ND	ND	0.3862
As	4.949	0.2033	0.3379	0.4426	0.08676	0.325	3240	114	1.95
Au	ND	ND	0.006732	0.008406	0.001469	0.005657	0.07184	0.006136	0.03548
Ba	ND	ND	22.3	ND	ND	60.99	ND	ND	8.611
Br	ND	ND	0.4936	ND	ND	0.4034	ND	ND	0.7394
Ca	941.2	46.83	85.4	ND	ND	191	ND	ND	35.28
Cd	ND	ND	7.57	ND	ND	5.609	ND	ND	47.49
Ce	0.9458	0.223	0.885	ND	ND	0.8717	ND	ND	0.8296
Cl	18.94	1.776	6.278	ND	ND	26.57	10.5	0.698	2.156
Co	3.142	0.1163	0.09957	58.49	2.118	0.09922	4.583	0.2269	0.08953
Cr	ND	ND	1.87	ND	ND	1.423	3.774	0.474	1.767
Cs	ND	ND	0.3588	ND	ND	0.3644	ND	ND	0.3397
Cu	16.84	1.542	4.158	ND	ND	3.934	273.9	81.38	2.758
Dy	0.1209	0.008316	0.02716	ND	ND	0.2071	ND	ND	0.04102
Er	ND	ND	16.65	ND	ND	65.79	ND	ND	6.813
Eu	ND	ND	0.02777	ND	ND	0.02178	ND	ND	0.02516
F	ND	ND	ND	ND	ND	ND	ND	ND	ND
Fe	468200	16410	100.8	462500	16190	100.2	447800	15680	94.88
Ga	ND	ND	7.603	ND	ND	25.71	14.54	2.067	ND
Gd	ND	ND	3.335	ND	ND	3.299	ND	ND	2.273
Ge	ND	ND	47.45	ND	ND	189.6	ND	ND	43.03
Hf	0.1831	0.044	0.1404	ND	ND	0.1705	ND	ND	0.1621
Hg	ND	ND	0.5804	ND	ND	0.5715	ND	ND	0.4657
Ho	ND	ND	0.2144	ND	ND	0.1736	ND	ND	1.535
I	ND	ND	1.97	ND	ND	8.066	ND	ND	0.5685
In	0.2185	0.008857	0.0109	20.93	1.443	4.901	0.051	0.003807	0.003391
Ir	ND	ND	0.5229	ND	ND	0.1472	ND	ND	1.702
K	287.7	25.44	62.61	132.3	15.78	35.16	ND	ND	86.76
La	0.5471	0.02445	0.01999	0.1685	0.01112	0.01494	ND	ND	0.1436
Lu	ND	ND	3.146	ND	ND	14.63	ND	ND	1.301
Mg	ND	ND	90.64	ND	ND	213.4	ND	ND	27.48
Mn	148.7	5.222	0.1626	728.7	25.58	0.467	2.32	0.09058	0.03969
Mo	ND	ND	5.499	ND	ND	4.39	ND	ND	15.63
Na	9.117	1.875	ND	ND	ND	12.89	5.373	0.4802	ND
Nb	ND	ND	187.9	ND	ND	421.6	ND	ND	65.5
Nd	ND	ND	2.777	ND	ND	2.777	ND	ND	2.682
Ni	ND	ND	887	ND	ND	3808	ND	ND	140.1
Os	ND	ND	0.2292	ND	ND	0.2293	ND	ND	0.2203
Pd	ND	ND	12.49	ND	ND	35.29	ND	ND	8.639
Pr	ND	ND	1.693	ND	ND	1.289	ND	ND	11.39
Pt	ND	ND	3.439	ND	ND	2.748	ND	ND	11.18
Rb	ND	ND	15.47	68.83	5.273	9.337	71.64	4.976	8.823
Re	ND	ND	0.08032	ND	ND	0.06397	ND	ND	0.1619
Rh	ND	ND	0.9712	ND	ND	3.464	ND	ND	0.4161
Ru	ND	ND	1.336	ND	ND	1.37	ND	ND	1.294
Sb	67.29	2.369	0.1723	ND	ND	0.06197	19.95	1.681	0.05468
Sc	0.1206	0.009326	0.006056	ND	ND	0.02636	ND	ND	0.02325
Se	ND	ND	1.493	ND	ND	1.387	2.487	0.2878	1.35
Si	ND	ND	ND	ND	ND	ND	ND	ND	137000
Sm	0.1528	0.007376	0.01828	0.0254	0.003847	0.01465	ND	ND	0.128
Sn	ND	ND	112.3	ND	ND	173.4	ND	ND	51.87
Sr	ND	ND	50.14	ND	ND	154.2	ND	ND	19.26
Ta	ND	ND	0.2246	ND	ND	0.2233	ND	ND	0.2101
Tb	ND	ND	0.1198	ND	ND	0.1168	ND	ND	0.1113
Te	ND	ND	5.053	ND	ND	5.034	ND	ND	4.938
Th	0.7539	0.0542	0.1867	ND	ND	0.1854	ND	ND	0.1775
Ti	45.18	3.943	13.81	ND	ND	100.5	ND	ND	16.95
Tm	ND	ND	0.4056	ND	ND	0.4022	ND	ND	0.2245
U	ND	ND	0.1734	ND	ND	0.4586	ND	ND	0.4062
V	0.2731	0.02327	0.04906	ND	ND	0.3591	1.633	0.06026	0.02271
W	ND	ND	0.3273	ND	ND	0.5932	ND	ND	1.831
Y	ND	ND	2505	ND	ND	11050	ND	ND	960.1
Yb	ND	ND	0.06753	ND	ND	0.1811	ND	ND	0.2389
Zn	979.2	34.54	3.636	ND	ND	21630	14.57	2.899	3.408
Zr	ND	ND	207.9	ND	ND	216.6	ND	ND	198.5

Element	G32428			G32429			G33033		
	Conc.	Unc.	LOD	Conc.	Unc.	LOD	Conc.	Unc.	LOD
Ag	155.4	5.469	1.232	5.004	0.2402	0.7304	ND	ND	2.365
Al	132.7	4.849	0.3821	18.3	0.7075	0.3143	6625	232.3	4.833
Ar	ND	ND	1.31	ND	ND	0.5839	ND	ND	0.9658
As	9551	336.6	5.886	53.49	1.885	0.331	2.781	0.1726	0.5011
Au	0.1231	0.01008	0.04473	ND	ND	0.003674	0.02604	0.002498	0.00887
Ba	ND	ND	29.41	ND	ND	4.834	20.27	2.18	0.1869
Br	ND	ND	2.74	ND	ND	0.4942	ND	ND	0.6252
Ca	293.5	26.12	83.55	61.67	20.41	43.41	1297	66.81	69.2
Cd	ND	ND	91.64	ND	ND	7.438	ND	ND	9.104
Ce	ND	ND	0.8515	11.69	0.4752	0.9027	28.04	1.271	0.0831
Cl	15.8	1.623	5.471	178.1	6.585	3.065	ND	ND	4.271
Co	5.571	0.2077	0.09592	7.586	0.6006	0.07233	255.8	13.97	0.158
Cr	2.368	0.4764	1.834	ND	ND	0.0823	18.74	0.9639	2.757
Cs	ND	ND	0.3426	ND	ND	0.3884	ND	ND	0.5216
Cu	394.3	14.12	4.803	209.7	7.87	2.073	ND	ND	3.804
Dy	ND	ND	0.06849	0.1474	0.009725	0.01824	2.532	0.09076	0.04194
Er	ND	ND	22.47	ND	ND	3.701	ND	ND	6.822
Eu	ND	ND	0.02663	0.06069	0.002773	0.01905	0.655	0.02662	0.03185
F	ND	ND	ND	ND	ND	ND	ND	ND	ND
Fe	440100	15420	98.53	474500	16620	102.8	435200	15240	153.5
Ga	ND	ND	0.002469	13.31	2.348	ND	ND	ND	4.182
Gd	ND	ND	3.192	ND	ND	1.084	ND	ND	5.394
Ge	ND	ND	49.18	ND	ND	18.51	ND	ND	187.9
Hf	ND	ND	0.081	ND	ND	0.1188	2.119	0.1356	0.224
Hg	ND	ND	0.5609	ND	ND	2.93	ND	ND	2.597
Ho	ND	ND	3.448	ND	ND	0.2152	0.6282	0.09071	0.346
I	ND	ND	2.062	ND	ND	0.3522	ND	ND	0.8081
In	0.6233	0.02267	0.01118	0.0405	0.002111	0.002444	ND	ND	0.004655
Ir	ND	ND	4.13	ND	ND	0.6347	ND	ND	0.3246
K	ND	ND	389	ND	ND	86.65	691.5	51.05	163.8
La	ND	ND	0.2858	6.224	0.2263	0.04047	13.8	0.4874	0.06289
Lu	ND	ND	4.22	ND	ND	0.8258	ND	ND	1.736
Mg	ND	ND	79.49	598.6	24.42	26.12	1742	67.26	46.9
Mn	34.86	1.259	0.1526	3.844	0.1381	0.04301	33.21	1.168	0.07621
Mo	ND	ND	29.46	ND	ND	5.81	16.45	3.444	13.4
Na	9.34	1.388	ND	66.57	2.704	ND	168	6.239	ND
Nb	ND	ND	159	ND	ND	59.46	ND	ND	204.8
Nd	ND	ND	2.767	3.8	0.6576	2.577	13.38	1.163	0.07289
Ni	ND	ND	643	ND	ND	217.2	559.3	90.74	241.4
Os	ND	ND	0.2268	ND	ND	0.2215	ND	ND	0.3725
Pd	ND	ND	16.7	ND	ND	4.14	ND	ND	33.27
Pr	ND	ND	27.47	ND	ND	2.759	ND	ND	4.457
Pt	ND	ND	11.87	ND	ND	3.638	ND	ND	5.067
Rb	ND	ND	14.12	ND	ND	15.6	32.25	6.992	13.91
Re	ND	ND	0.1708	ND	ND	0.08621	ND	ND	0.1208
Rh	ND	ND	0.6435	ND	ND	0.2565	ND	ND	7.24
Ru	ND	ND	1.321	ND	ND	1.39	ND	ND	28.79
Sb	36.58	1.338	0.2545	ND	ND	0.06633	0.9774	0.06412	0.1074
Sc	ND	ND	0.02183	0.1387	0.02452	0.006354	0.9004	0.03386	0.009828
Se	2.929	0.3095	1.379	28.61	1.048	1.527	23.88	1.033	2.191
Si	ND	ND	ND	ND	ND	167400	ND	ND	ND
Sm	ND	ND	0.1306	0.3737	0.02327	0.01922	2.391	0.09631	0.02873
Sn	ND	ND	51.39	ND	ND	29.18	ND	ND	59.19
Sr	ND	ND	66.24	ND	ND	9.818	ND	ND	20.57
Ta	ND	ND	0.2151	ND	ND	0.237	5.031	0.3578	0.1863
Tb	ND	ND	0.1145	ND	ND	0.1226	0.377	0.02938	0.1711
Te	ND	ND	5.053	ND	ND	4.364	ND	ND	3.553
Th	ND	ND	0.1836	ND	ND	0.08826	8.009	0.2908	0.2778
Ti	ND	ND	35.4	27.42	2.213	7.471	2267	80.98	35.37
Tm	42.75	5.719	0.3888	ND	ND	0.4278	ND	ND	0.7235
U	ND	ND	1.346	ND	ND	0.2028	2.587	0.1341	0.4226
V	1.369	0.05288	0.05571	0.5559	0.02585	0.01583	8.401	0.4683	0.2516
W	ND	ND	3.741	3.895	0.1838	0.6236	2.334	0.1753	0.9415
Y	ND	ND	3109	ND	ND	533.2	ND	ND	1057
Yb	ND	ND	0.2238	ND	ND	0.1274	1.303	0.06719	0.2704
Zn	1168	41.19	3.48	102.4	4.927	3.853	33.3	5.144	5.868
Zr	ND	ND	199.9	ND	ND	225.1	ND	ND	314

Element	G33797			G6876			G9699		
	Conc.	Unc.	LOD	Conc.	Unc.	LOD	Conc.	Unc.	LOD
Ag	ND	ND	1.066	ND	ND	0.5991	ND	ND	2.695
Al	166.6	5.964	0.6535	2.673	0.1991	0.266	692.4	24.32	0.7035
Ar	ND	ND	0.7921	ND	ND	0.2885	ND	ND	1.341
As	8.599	0.3157	0.2501	114.2	4.023	0.3302	537.9	18.85	0.9242
Au	0.005203	0.001219	0.004783	ND	ND	0.007452	0.1317	0.007268	0.02193
Ba	ND	ND	8.113	ND	ND	2.693	ND	ND	13.77
Br	ND	ND	0.2695	ND	ND	0.3925	1.595	0.348	1.362
Ca	405.9	27.48	69.73	ND	ND	52.54	ND	ND	80.32
Cd	ND	ND	4.658	ND	ND	8.016	ND	ND	24.94
Ce	ND	ND	0.7395	ND	ND	0.9006	ND	ND	3.175
Cl	56.73	2.421	3.805	4.529	0.5311	1.463	375.3	15.71	6.786
Co	4.745	0.2004	0.05384	61.72	3.089	0.104	2108	112.8	0.3806
Cr	ND	ND	0.2469	ND	ND	1.457	ND	ND	5.968
Cs	ND	ND	0.333	ND	ND	0.4032	ND	ND	1.206
Cu	17.66	2.487	1.502	ND	ND	1.056	109.3	4.66	6.062
Dy	ND	ND	0.03193	ND	ND	0.01503	ND	ND	0.09486
Er	ND	ND	2.381	ND	ND	1.851	ND	ND	10.99
Eu	ND	ND	0.01175	ND	ND	0.0109	ND	ND	0.03892
F	ND	ND	ND	ND	ND	ND	ND	ND	ND
Fe	446100	15620	86.44	424400	14870	105.3	456400	15990	359.9
Ga	ND	ND	3.22	ND	ND	1.274	ND	ND	6.935
Gd	ND	ND	1.688	ND	ND	0.7283	ND	ND	8.721
Ge	ND	ND	164.2	ND	ND	29.84	ND	ND	201.9
Hf	ND	ND	0.1472	ND	ND	0.1791	ND	ND	0.6033
Hg	ND	ND	1.227	ND	ND	0.5423	ND	ND	4.538
Ho	ND	ND	0.1366	ND	ND	0.2132	ND	ND	0.7394
I	ND	ND	0.7244	ND	ND	0.2001	ND	ND	1.06
In	0.07163	0.00331	0.004058	ND	ND	0.00488	0.1117	0.006006	0.007042
Ir	ND	ND	0.1391	ND	ND	0.2258	ND	ND	0.7345
K	37.99	7.759	24.22	ND	ND	40.8	ND	ND	176.6
La	0.02602	0.004516	0.01284	ND	ND	0.023	ND	ND	0.08932
Lu	ND	ND	1.082	ND	ND	0.5582	ND	ND	3.945
Mg	569.7	22	36.71	19.9	2.929	13.98	682.3	29.1	65.27
Mn	47.83	1.686	0.06162	0.8341	0.03251	0.02452	10.69	0.3994	0.1258
Mo	ND	ND	3.712	ND	ND	4.245	ND	ND	20.16
Na	11.63	1.815	ND	8.771	0.586	ND	253.6	11.62	ND
Nb	ND	ND	96.22	ND	ND	35.4	ND	ND	390.1
Nd	ND	ND	2.026	ND	ND	2.511	ND	ND	9.207
Ni	ND	ND	401.2	ND	ND	77.16	2943	168.9	334
Os	ND	ND	0.1787	ND	ND	0.2197	ND	ND	0.7934
Pd	ND	ND	7.36	ND	ND	2.1	ND	ND	21.72
Pr	ND	ND	0.7555	ND	ND	1.473	ND	ND	6.105
Pt	ND	ND	2.333	ND	ND	3.799	ND	ND	12.78
Rb	58.85	4.243	7.465	ND	ND	15.89	ND	ND	61.33
Re	ND	ND	0.05516	ND	ND	0.09012	ND	ND	0.2996
Rh	ND	ND	1.302	ND	ND	0.2734	ND	ND	2.647
Ru	ND	ND	1.17	ND	ND	1.425	ND	ND	4.583
Sb	0.2751	0.03804	0.1436	ND	ND	0.07529	4.14	0.3289	0.5197
Sc	ND	ND	0.02757	ND	ND	0.02757	0.1952	0.0283	0.02317
Se	13.65	0.5424	1.293	4.531	0.5305	1.549	71.74	2.727	5.136
Si	ND	ND	247000	ND	ND	87070	ND	ND	ND
Sm	ND	ND	0.01249	ND	ND	0.01977	ND	ND	0.06717
Sn	ND	ND	48.56	ND	ND	16.49	ND	ND	82.85
Sr	ND	ND	18.99	ND	ND	5.583	ND	ND	31.97
Ta	ND	ND	0.1995	ND	ND	0.2421	ND	ND	0.7825
Tb	ND	ND	0.103	ND	ND	0.1255	ND	ND	0.3961
Te	ND	ND	3.361	ND	ND	4.231	ND	ND	13.74
Th	ND	ND	0.1543	ND	ND	0.189	ND	ND	0.6236
Ti	ND	ND	12.04	ND	ND	4.758	ND	ND	65.21
Tm	ND	ND	0.3607	ND	ND	0.1565	ND	ND	1.127
U	ND	ND	0.06995	ND	ND	0.231	ND	ND	1.867
V	0.7427	0.05004	0.03511	0.02955	0.005893	0.009789	1.851	0.07395	0.1191
W	ND	ND	0.4498	ND	ND	0.2103	ND	ND	1.717
Y	ND	ND	925.2	ND	ND	268.3	ND	ND	1496
Yb	ND	ND	0.1602	ND	ND	0.2406	ND	ND	0.7518
Zn	281.4	10.49	3.259	ND	ND	1892	ND	ND	5502
Zr	ND	ND	189.9	ND	ND	231.7	ND	ND	709.2

Appendix B

Description of the geological settings of the 9 samples examined in detail in Chapter 5.

G20974 - Zeigler Mine, Sparta, Randolph Co., Illinois, USA.

The unique pyrite nodules, known popularly as pyrite dollars or pyrite suns, occur in black shale beds directly overlying coal seams in the Zeigler Mine adjacent to the town of Sparta, Illinois, USA. Despite the abundance of specimens from this locality on the international mineral specimen market, the authors have been unable to find a detailed account of the occurrence. These pyrite nodules have been known for many years, noted by Bannister [117] and Van Horn and Van Horn [118] who showed that the nodules are pyrite rather than marcasite. The coal sequence is of Pennsylvanian age (upper Carboniferous) and part of the Carbondale formation. The black shale layer is approximately 1m thick and the rock is brittle and highly fissile. It is said to contain so much organic matter that it is flammable. In general, pyrite and carbonate concretions are common in the black shales associated with the coal measures in Illinois. The distribution of fossils indicates that the shale was deposited in extremely quiet water where the substrate and part of the water column had very low oxygen levels [119]. These sediments must have been directly deposited in layers of peat. What is unclear is why these disk-like nodules only occur at Zeigler Mine at Sparta. The morphology of the nodules and the fact they are flattened parallel to the lamination in the shale could suggest that the concretions grew under a strong axial pressure, but the laminations in the shale at Sparta are not especially well developed. It is clear that pyrite in these black shales was originally deposited in low temperature anoxic conditions from the transformation of mackinawite (FeS_m). Rickard and Luther [5] note that trace amounts of organic contaminants could have an effect on the formation process.

G33033 - Ampliación a Victoria Mine, Navajún, La Rioja, Spain.

This is a world famous locality for well-formed pyrite cubes, which has been worked commercially since the 1970s for specimens for the mineral market [120]. The cubes occur disseminated in layers of marl of late Jurassic-Early Cretaceous age, overlain by sandstone units. The pyrite cubes are believed to have been formed by the hydrothermal sulfidation of chlorites in the marl. Reduced sulfur was supplied largely by thermochemical reduction of sulfate and with a small amount coming from sedimentary sulfides during metamorphism. The peak temperature during metamorphism is estimated to be 370°C, but the temperature at which the pyrite crystals grew is unknown [121-123]. The pyrite crystals commonly contain inclusions of chloritoid, rutile, quartz and muscovite [93].

G32419 - Black Cloud Mine, Leadville, Colorado, USA.

The Black Cloud Mine, is in the Leadville district of Colorado. The sulfide mineralisation is of a type known as Leadville type mineralisation (LTM) and consists of massive sulfide replacement of dolomite beds. The replacement ore bodies are dominated by pyrite with lesser sphalerite and galena. The ore bodies commonly exhibit layering of intergrowth of sulfides and gangue minerals parallel to the dolomite beds or to faults. Pyrite quartz and siderite are the earliest minerals in the LTM paragenetic sequence. Fluid inclusion studies on early quartz give a hydrothermal temperature range of 245 to 355°C with pressures of 1.2Kbar. The mineralization is dated to the Tertiary period fission track data gives a date of 33.8±5Ma [124].

G29969 - Paulsens Mine, Wyloo, Western Australia.

Paulsens Mine is an operational underground gold mine located 180km west of the mining town of Paraburdoo, Western Australia. The deposit is an orogenic, structurally controlled deposit in which the gold with massive and disseminated pyrite host in quartz veins [125]. The deposit is hosted in Archaean Fortescue Group metasediments and metavolcanics of the Hamersley Basin. The pyrite, probably of originally sedimentary origin, has been remobilised by hydrothermal fluids during a number of structural

deformations of the deposit. The PT and solution conditions for the hydrothermal remobilisation events have not been reported [126].

G23414 - Portland Limestone Quarry, Fermont Co., Colorado, USA.

Pyrite nodules to 2.5cm are found in dark shale layers of the Niobrara formation of Cretaecoius age. The nodules show lustrous, well developed faces. The origin of the pyrite is thought to be associated the decomposition of organic material [127]. The grade of the diagenesis of the deposit is unknown.

G32422 - Siglo XX Mine, Llallagua, Bolivia.

The Llallagua tin deposit is located in a conical subvolcanic stock of Tertiary age. It is a porphyry and porphyry breccia, which have subjected to extensive high temperature hydrothermal and have been altered such that the feldspar has been stripped from the porphyry. Dietrich *et al.* [128] obtained emplacement temperatures for the porphyry based on melt inclusion data of 620 to 740°C. Mineralisation is hydrothermal vein style; mineralisation tended to be higher temperature towards the top of the deposit, with lower temperatures towards to lower parts of the ore body. The pyrite used in this study were euhedral crystals dominated by octahedral {111} and cube {100} forms.

G33797 - Huanzala Mine, Huallanca District, Dos de Mayo, Peru.

Mineralisation occurs in veins associated with a granodiorite porphyry sheet dykes hosted in limestone. The porphyry dykes have been extensively sericitised (transformed to mica) and subject to sporadic pyritisation. The pyrite mineralisation can be group texturally into the compact, fine-grained type and the loosely bound. coarse grained type. The samples used in this study were euhedral masses of crystals up to 1cm across, so belong to the coarse grained type. The coarser-grained pyrite is the product of crystallisation by later hydrothermal solutions and is surrounded by sericitised or other hydrothermal altered rocks [129]. Decrepitation method of fluid inclusion geothermometry gives a hydrothemal temperature for the recrystallisation of the pyrite in the range of 250 to 330°C [129].

G17012 - Poona Mine, Moonta, South Australia.

The pyrite occurs as pyritohedral crystals to 2cm in diameter embedded in quartz vein. The deposit is a hydrothermal vein system, associated with the emplacement of the Moonta porphyry. Morales Ruano *et al.* [130] undertook a detailed fluid inclusion study of quartz from the Poona vein system and these gave homogenisation temperatures over a wide range (104 to 467°C). However, the fluid inclusions where subdivided into three groups: two phase vapour-rich, two phase liquid rich and solid bearing fluid inclusions. The pyrite sample used in the current study came from the upper part of the deposit and model for fluid mixing and fluid inclusion type proposed by Morales Ruano *et al.* [130] suggest a formation temperature in the lower end of the range possible 100 to 200°C.

G32427 - Ophir Hill Mine, Ophir, Tooele Co., Utah, USA.

The pyrite occurs as 5mm cubes, with highly altered hornfels, rhyolite and monzonite. The mineralisation, principally Pb-Zn sulfides, at the Ophir Hill Mine occurs as veins and massive replacement of skarn and marble. Both skarn alteration and ore zones are defined within fissures and faults. Skarn formation is followed by sulfide-tungstatefluorite-phyllosilicate mineralisation, and latest minor postore fluorite-phyllosilicate mineralisation. A thermal history for the hydrothermal skarn fluid gave temperatures between 200 and 350ºC and Wilson and Parry [131] concluded that sulfides precipitated as a result of boiling or by the mixing of a low salinity at about 300ºC.

References

1. Rickard, D., *Chapter 1 - Introduction*, in *Developments in Sedimentology*, R. David, Editor 2012, Elsevier. p. 1-29.

2. Lefticariu, L., Pratt, L.M., and Ripley, E.M., *Mineralogic and sulfur isotopic effects accompanying oxidation of pyrite in millimolar solutions of hydrogen peroxide at temperatures from 4 to 150 °C.* Geochimica et Cosmochimica Acta, **2006**. 70(19), p.4889-4905.

3. Abraitis, P.K., Pattrick, R.A.D., and Vaughan, D.J., *Variations in the compositional, textural and electrical properties of natural pyrite: a review.* International Journal of Mineral Processing, **2004**. 74(1-4), p.41-59.

4. Antonijevic, M.M., Dimitrijevic, M., and Jankovic, Z., *Leaching of pyrite with hydrogen peroxide in sulphuric acid.* Hydrometallurgy, **1997**. 46(1-2), p.71-83.

5. Rickard, D. and Luther, G.W.I.I.I., *Chemistry of Iron Sulfides.* Chemical Reviews **2007**. 107(2), p.514–562.

6. Egiebor, N.O. and Oni, B., *Acid rock drainage formation and treatment: a review.* Asia-Pacific Journal of Chemical Engineering, **2007**. 2(1), p.47-62.

7. Wiersma, C.L. and Rimstidt, J.D., *Rates of reaction of pyrite and marcasite with ferric iron at pH 2.* Geochimica et Cosmochimica Acta, **1984**. 48(1), p.85-92.

8. Chirita, P., *A Kinetic Study of Hydrogen Peroxide Decomposition in Presence of Pyrite.* Chemical & Biochemical Engineering Quarterly, **2007**. 21(3), p.257-264.

9. Wood, H.T., *Industrial England in the middle of the eighteenth century.* Nature, **1910**. 83(2113), p.264-268.

10. Schoonen, M.A.A., Harrington, A.D., Laffers, R., and Strongin, D.R., *Role of hydrogen peroxide and hydroxyl radical in pyrite oxidation by molecular oxygen.* Geochimica et Cosmochimica Acta, **2010**. 74(17), p.4971-4987.

11. Singer, P.C., *Oxygenation of ferrous iron.* Federal Water Quality Administration Department of the Interior, **1970**, p.224.

12. Lu, L., Wang, R.C., Chen, F.R., Xue, J.Y., Zhang, P.H., and Lu, J.J., *Element mobility during pyrite weathering: implications for acid and heavy metal pollution at mining-impacted sites.* Environmental Geology, **2005**. 49(1), p.82-89.

13. Bierens de Haan, S., *A review of the rate of pyrite oxidation in aqueous systems at low temperature.* Earth-Science Reviews, **1991**. 31(1), p.1-10.

14. Lottermoser, B.G., Ashley, P.M., and Lawie, D.C., *Environmental geochemistry of the Gulf Creek copper mine area, north-eastern New South Wales, Australia.* Environmental Geology, **1999**. 39(1), p.61-74.

15. U.S.E.P.A, *Technical Document: Acid Mine Drainage Prediction*, 1994, U.S. Environmental Protection Agency.

16. Osborne, O., *Oxidised Pyrite Sample*, 2007, South Australian Museum: Adelaide.

17. Osborne, O., *Untarnished Pyrite Sample*, 2007, South Australian Museum: Adelaide.

18. *The Handbook of Mineralogy*, J.W. Anthony, R.A. Bideaux, K.W. Bladh, and M.C. Nichols, Editors. 2003, Mineralogical Society of America: Chantilly.

19. Bragg, W.H. and Bragg, W.L., *The Reflection of X-rays by Crystals.* Proceedings of the Royal Society of London. Series A, Containing Papers of a Mathematical and Physical Character (1905-1934), **1913**. 88(605), p.428-549.

20. Lowson, R.T., *Aqueous oxidation of pyrite by molecular oxygen.* Chemical Reviews, **1982**. 82(5), p.461-497.

21. Jessey, D. *Sulfetos*. 2009 14/01/2009]; Available from: http://www.geologo.com.br/sulfetos.asp.

22. Lavinsky, R. *Pyrite-290488.jpg*. [Image] 2010 31/05/2013; Available from: http://wikimediafoundation.org/wiki/File:Pyrite-290488.jpg.

23. Lavinsky, R. *Pyrite-193871.jpg*. [Image] 2010 31/05/2013; Available from: http://wikimediafoundation.org/wiki/File:Pyrite-193871.jpg.

24. Weber, P.A., Stewart, W.A., Skinner, W.M., Weisener, C.G., Thomas, J.E., and Smart, R.S.C., *Geochemical effects of oxidation products and framboidal pyrite oxidation in acid mine drainage prediction techniques.* Applied Geochemistry, **2004**. 19(12), p.1953-1974.

25. Butler, I.B. and Rickard, D., *Framboidal pyrite formation via the oxidation of iron (II) monosulfide by hydrogen sulphide.* Geochimica et Cosmochimica Acta, **2000**. 64(15), p.2665-2672.

26. Ohfuji, H. and Rickard, D., *Experimental syntheses of framboids--a review.* Earth-Science Reviews, **2005**. 71(3-4), p.147-170.

27. Lehner, S., Savage, K., Ciobanu, M., and Cliffel, D.E., *The effect of As, Co, and Ni impurities on pyrite oxidation kinetics: An electrochemical study of synthetic pyrite.* Geochimica et Cosmochimica Acta, **2007**. 71(10), p.2491-2509.

28. Pridmore, D.F. and Shuey, R.T., *The electrical resistivity of galena, pyrite, and chalcopyrite.* American Mineralogist, **1976**. 61(3-4), p.248-259.

29. Doyle, F.M. and Mirza, A.H., *Electrochemical Oxidation of Pyrite Samples with known Composition and Electrical Properties*, in *Proceedins of the 4th International Symposium on Electrochemistry in Mineral and Metal Processing*, R. Woods, F.M. Doyle, and P. Richardson, Editors. 1996, The Electrochemical Society. p. 203-214.

30. Smith, F.G., *Variation in the properties of pyrite.* University of Toronto Studies., Geological Studies, **1942**. 44, p.83-93.

31. Rimstidt, J.D. and Vaughan, D.J., *Pyrite oxidation: a state-of-the-art assessment of the reaction mechanism.* Geochimica et Cosmochimica Acta, **2003**. 67(5), p.873-880.

32. Li, Y., Chen, J., Chen, Y., and Guo, J., *Density functional theory study of influence of impurity on electronic properties and reactivity of pyrite.* Transactions of Nonferrous Metals Society of China, **2011**. 21(8), p.1887-1895.

33. Deditius, A.P., Utsunomiya, S., Reich, M., Kesler, S.E., Ewing, R.C., Hough, R., and Walshe, J., *Trace metal nanoparticles in pyrite.* Ore Geology Reviews, **2011**. 42(1), p.32-46.

34. Cabri, L.J., Newville, M., Gordon, R.A., Crozier, E.D., Sutton, S.R., McMahon, G., and Jiang, D.-T., *Chemical speciation of gold in arsenopyrite.* The Canadian Mineralogist, **2000**. 38(5), p.1265-1281.

35. Demoisson, F. and Humbert, M.M.B., *Pyrite oxidation in acidic medium: overall reaction pathway.* Surface and Interface Analysis, **2008**. 40(3-4), p.343-348.

36. Descostes, M., Vitorge, P., and Beaucaire, C., *Pyrite dissolution in acidic media.* Geochimica et Cosmochimica Acta, **2004**. 68(22), p.4559-4569.

37. Jerz, J.K. and Rimstidt, J.D., *Pyrite oxidation in moist air.* Geochimica et Cosmochimica Acta, **2004**. 68(4), p.701-714.

38. Manaka, M., *Comparison of rate laws for the oxidation of five pyrites by dissolved oxygen in acidic solution.* Journal of Mineralogical and Petrological Sciences, **2007**. 102(1), p.24-38.

39. Nicholson, R.V., Gillham, R.W., and Reardon, E.J., *Pyrite oxidation in carbonate-buffered solution: 1. Experimental kinetics.* Geochimica et Cosmochimica Acta, **1988**. 52(5), p.1077-1085.

40. Borda, M.J., Strongin, D.R., and Schoonen, M.A., *A vibrational spectroscopic study of the oxidation of pyrite by ferric iron.* American Mineralogist, **2003**. 88(8-9), p.1318-1323.

41. Dimitrijevic, M., Antonijevic, M.M., and Dimitrijevic, V., *Investigation of the kinetics of pyrite oxidation by hydrogen peroxide in hydrochloric acid solutions.* Minerals Engineering, **1999**. 12(2), p.165-174.

42. Dimitrijevic, M., Antonijevic, M.M., and Jankovic, Z., *Kinetics of pyrite dissolution by hydrogen peroxide in perchloric acid.* Hydrometallurgy, **1996**. 42(3), p.377-386.

43. Lefticariu, L., Schimmelmann, A., Pratt, L.M., and Ripley, E.M., *Oxygen isotope partitioning during oxidation of pyrite by H2O2 and its dependence on temperature.* Geochimica et Cosmochimica Acta, **2007**. 71(21), p.5072-5088.

44. Holmes, P.R. and Crundwell, F.K., *The kinetics of the oxidation of pyrite by ferric ions and dissolved oxygen: an electrochemical study.* Geochimica et Cosmochimica Acta, **2000**. 64(2), p.263-274.

45. Moses, C.O., Kirk Nordstrom, D., Herman, J.S., and Mills, A.L., *Aqueous pyrite oxidation by dissolved oxygen and by ferric iron.* Geochimica et Cosmochimica Acta, **1987**. 51(6), p.1561-1571.

46. Williamson, M.A. and Rimstidt, J.D., *The kinetics and electrochemical rate-determining step of aqueous pyrite oxidation.* Geochimica et Cosmochimica Acta, **1994**. 58(24), p.5443-5454.

47. Antonijevic, M.M., Dimitrijevic, M.D., Serbula, S.M., Dimitrijevic, V.L.J., Bogdanovic, G.D., and Milic, S.M., *Influence of inorganic anions on*

electrochemical behaviour of pyrite. Electrochimica Acta, **2005**. 50(20), p.4160-4167.

48. Borah, D., Baruah, M.K., and Gogoi, P.C., *Model study of pyrite demineralization by hydrogen peroxide oxidation at 30ºC in the presence of metal ions (Ni^{2+}, Co^{2+} and Sn^{2+}).* Fuel Processing Technology, **2005**. 86(7), p.769-779.

49. Schoonen, M., Elsetinow, A., Borda, M., and Strongin, D., *Effect of temperature and illumination on pyrite oxidation between pH 2 and 6* Geochemical Transactions, **2000**. 1, p.23-33.

50. Smith, E.E. and Shumate, K.S., *Sulfide to sulfate reaction mechanism*. Water Pollution Control Research Series1970, Washington: U.S Federal Water Quality Administration. 122.

51. Borda, M.J., Elsetinow, A.R., Strongin, D.R., and Schoonen, M.A., *A mechanism for the production of hydroxyl radical at surface defect sites on pyrite.* Geochimica et Cosmochimica Acta, **2003**. 67(5), p.935-939.

52. Druschel, G. and Borda, M., *Comment on "Pyrite dissolution in acidic media" by M. Descostes, P. Vitorge, and C. Beaucaire.* Geochimica et Cosmochimica Acta, **2006**. 70(20), p.5246-5250.

53. Liu, R., Wolfe, A., Dzombak, D., Stewart, B., and Capo, R., *Comparison of dissolution under oxic acid drainage conditions for eight sedimentary and hydrothermal pyrite samples.* Environmental Geology, **2007**.

54. Garrels, R.M. and Thompson, M.E., *Oxidation of pyrite by iron sulfate solutions.* American Journal of Science, **1960**. 258A, p.56-67.

55. Liu, R., Wolfe, A.L., Dzombak, D.A., Horwitz, C.P., Stewart, B.W., and Capo, R.C., *Electrochemical study of hydrothermal and sedimentary pyrite dissolution.* Applied Geochemistry, **2008**. 23(9), p.2724-2734.

56. Cruz, R., Bertrand, V., Monroy, M., and Gonzalez, I., *Effect of sulfide impurities on the reactivity of pyrite and pyritic concentrates: a multi-tool approach.* Applied Geochemistry, **2001**. 16(7-8), p.803-819.

57. McKibben, M.A. and Barnes, H.L., *Oxidation of pyrite in low temperature acidic solutions: Rate laws and surface textures.* Geochimica et Cosmochimica Acta, **1986**. 50(7), p.1509-1520.

58. Sobek, A.A., Schuller, W.A., Freeman, J.R., and Smith, R.M., *Field and Laboratory Methods Applicable to Overburden and Minesoils*, 1978, U.S. Environmental Protection Agency.

59. Chirita, P., *Kinetics of aqueous pyrite oxidation by potassium dichromate-an experimental study.* Turkish Journal of Chemistry, **2003**. 27(1), p.111-118.

60. ASTM, *Standard Test Methods for Iron in Water*, in *Standard D1068 - 10*2010: ASTM International.

61. Method 6020A, 6000 Series Methods, 2007. Inductively Coupled Mass Spectrometry, Environmental Protection Agency http://www.epa.gov/osw/hazard/testmethods/sw846/pdfs/6020a.pdf

62. Krishna Murti, G.S.R., Moharir, A.V., and Sarma, V.A.K., *Spectrophotometric determination of iron with orthophenanthroline.* Microchemical Journal, **1970**. 15(4), p.585-589.

63. Tamura, H., Goto, K., Yotsuyanagi, T., and Nagayama, M., *Spectrophotometric determination of iron(II) with 1,10-phenanthroline in the presence of large amounts of iron(III).* Talanta, **1974**. 21(4), p.314-318.

64. Karamanev, D.G., Nikolov, L.N., and Mamatarkova, V., *Rapid simultaneous quantitative determination of ferric and ferrous ions in drainage waters and similar solutions.* Minerals Engineering, **2002**. 15(5), p.341-346.

65. Pal, S.K. and Lahiri, S.C., *Ferric-sulfosalicylate complex in several mixed solvents.* Zeitschrift fuer Physikalische Chemie (Leipzig), **1974**. 255(5), p.910-14.

66. Pullin, M.J. and Cabaniss, S.E., *Colorimetric flow-injection analysis of dissolved iron in high DOC waters.* Water Research, **2001**. 35(2), p.363-372.

67. Pascual-Reguera, M.I., Ortega-Carmona, I., and Molina-Díaz, A., *Spectrophotometric determination of iron with ferrozine by flow-injection analysis.* Talanta, **1997**. 44(10), p.1793-1801.

68. Oliveira, P.C.C. and Masini, J.C., *Sequential injection determination of iron (II) in anti-anemic pharmaceutical formulations with spectrophotometric detection.* Analytical Letters, **2001**. 34(3), p.389-397.

69. Benson, R.L. and Worsfold, P.J., *A flow-injection approach to the continuous monitoring of residual coagulants (aluminium and iron) in potable and treated waters.* The Science of The Total Environment, **1993**. 135(1-3), p.17-25.

70. Haghighi, B. and Safavi, A., *Simultaneous flow injection determination of iron(II) and iron(III) with opto-electrochemical detection.* Analytica Chimica Acta, **1997**. 354(1-3), p.43-50.

71. Pojanagaroon, T., Watanesk, S., Rattanaphani, V., and Liawrungrath, S., *Reverse flow injection spectrophotometric determination of iron(III) using norfloxacin.* Talanta, **2002**. 58(6), p.1293-1300.

72. Zagatto, E.A.G., Worsfold, P.J., Paul, W., Alan, T., and Colin, P., *FLOW ANALYSIS | Overview*, in *Encyclopedia of Analytical Science,* 2005, Elsevier: Oxford. p. 24-31.

73. Luque de Castro, M.D., Paul, W., Alan, T., and Colin, P., *FLOW INJECTION ANALYSIS | Principles*, in *Encyclopedia of Analytical Science* 2005, Elsevier: Oxford. p. 31-39.

74. Wagner, C., Armenta, S., and Lendl, B., *Developing automated analytical methods for scientific environments using LabVIEW.* Talanta, **2010**. 80(3), p.1081-1087.

75. Wisotzky, F., *Redox Reactions, Multi-Component Stability Diagrams and Isotopic Investigations in Sulfur- and Iron-Dominated Groundwater Systems*, in *Redox: Fundamentals, Processes and Applications*, J. Schüring, H.D. Schulz, W.R. Fischer, J. Böttcher, and W.H.M. Duijnisveld, Editors. 2000, Springer. p. 175-188.

76. Clescerl, L.S., Greenberg, A.E., and Eaton, A.D., *Standard Methods for the Examination of Water and Wastewater*, A.P.H. Association, Editor 1998, American Public Health Association: Washington DC. p. 1325.

77. Mahmoud, W.H., *Iron ion-selective electrodes for direct potentiometry and potentiotitrimetry in pharmaceuticals.* Analytica Chimica Acta, **2001**. 436(2), p.199-206.

78. de Jong, J., Schoemann, V., Tison, J.-L., Becquevort, S., Masson, F., Lannuzel, D., Petit, J., Chou, L., Weis, D., and Mattielli, N., *Precise measurement of Fe isotopes in marine samples by multi-collector inductively coupled plasma mass spectrometry (MC-ICP-MS).* Analytica Chimica Acta, **2007**. 589(1), p.105-119.

79. Pozdnyakov, I.P., Plyusnin, V.F., Grivin, V.P., Vorobyev, D.Y., Bazhin, N.M., and Vauthey, E., *Photolysis of sulfosalicylic acid in aqueous*

solutions over a wide pH range. Journal of Photochemistry and Photobiology A: Chemistry, **2006**. 181(1), p.37-43.

80. Agren, A., *The Complex Formation between Iron (III) Ion and Sulfosalicylic Acid.* Acta Chemica Scandinavica, **1954**. 8(2), p.266-279.

81. Foley, R.T. and Anderson, R.C., *Spectrophotometric Studies on Complex Formation with Sulfosalicylic Acid. I. With Iron III.* Journal of the American Chemical Society, **1948**. 70(3), p.1195-1197.

82. Ogawa, K.y. and Tobe, N., *A Spectrophotometric Study of the Complex Formation between Iron(III) and Sulfosalicylic Acid.* Bulletin of the Chemical Society of Japan, **1966**. 39(2), p.223-227.

83. Horstkotte, B., Tovar Sanchez, A., Duarte, C.M., and Cerda, V., *Sequential injection analysis for automation of the Winkler methodology, with real-time SIMPLEX optimization and shipboard application.* Analytica Chimica Acta. 658(2), p.147-155.

84. Pozdnyakov, I.P., Plyusnin, V.F., Tkachenko, N., and Lemmetyinen, H., *Photophysics of Fe(III)-sulfosalicylic acid complexes in aqueous solutions.* Chemical Physics Letters, **2007**. 445(4-6), p.203-207.

85. Zhao, H.-X., Frimmel, H.E., Jiang, S.-Y., and Dai, B.-Z., *LA-ICP-MS trace element analysis of pyrite from the Xiaoqinling gold district, China: Implications for ore genesis.* Ore Geology Reviews, **2011**. 43(1), p.142-153.

86. Bennett, J., Grave, P., and Stopic, A., *Establishing a basis for nuclear archaeometry in Australia using the 20 MW OPAL research reactor.* Journal of Radioanalytical and Nuclear Chemistry, **2012**. 291(1), p.13-17.

87. Koltov, V.P. and Corte, F.D., *Compilation of k0 and Related Data for Neutron-Activation Analysis (NAA) in the Form of an Electronic Database.* Pure and Applied Chemistry, **2004**. 76(10), p.1921-1925.

88. Greenberg, R.R., Bode, P., and De Nadai Fernandes, E.A., *Neutron activation analysis: A primary method of measurement.* Spectrochimica Acta Part B: Atomic Spectroscopy, **2011**. 66(3-4), p.193-241.

89. Popelka-Filcoff, R., Lenehan, C., Glascock, M., Bennett, J., Stopic, A., Quinton, J., Pring, A., and Walshe, K., *Evaluation of relative comparator and K0-NAA for characterization of Aboriginal Australian ochre.* Journal of Radioanalytical and Nuclear Chemistry, p.1-6.

90. Adesida, D.A., Agbaji, E.B., and Ekanem, E.J., *Characterisation and processing of some selected Nigerian solid mineral samples using short-lived nuclides of Neutron Activation Analysis (NAA).* ChemClass Journal, **2005**. 2, p.55-58.

91. Bennett, J., *Commissioning of NAA at the new OPAL reactor in Australia.* Journal of Radioanalytical and Nuclear Chemistry, **2008**. 278(3), p.671-673.

92. Glascock, M.D. and Neff, H., *Neutron activation analysis and provenance research in archaeology.* Measurement Science and Technology, **2003**. 14(9), p.1516-1526.

93. Lodders, K., Klingelhofer, G., and Kremser, D.T., *chloritoid inclusions in pyrite from Navajun, Spain.* The Canadian Mineralogist, **1998**. 36, p.137-145.

94. MacDougall, D. and Crummett, W.B., *Guidelines for data acquisition and data quality evaluation in environmental chemistry.* Analytical Chemistry, **1980**. 52(14), p.2242-2249.

95. De Corte, F. and Simonits, A., *Vade Mecum for k0 users* 1994.

96. Currie, L.A., *Limits for qualitative detection and quantitative determination. Application to radiochemistry.* Analytical Chemistry, **1968**. 40(3), p.586-593.

97. Cook, N.J., Ciobanu, C.L., Pring, A., Skinner, W., Shimizu, M., Danyushevsky, L., Saini-Eidukat, B., and Melcher, F., *Trace and minor elements in sphalerite: A LA-ICPMS study.* Geochimica et Cosmochimica Acta, **2009**. 73(16), p.4761-4791.

98. Sung, Y.H., Brugger, J., Ciobanu, C., Pring, A., Skinner, W., Danyushevsky, L., and Nugus, M., *Invisible gold in arsenian pyrite and arsenopyrite from a multistage Archaean gold deposit: Sunrise Dam, Eastern Goldfields Province, Western Australia.* Mineralium Deposita, **2009**. 44(7), p.793-793.

99. Vaughan, D.J. and Craig, J.R., *Cambridge Earth Science Series. Mineral Chemistry of Metal Sulfides*. Cambridge Earth Science Series, ed. W.B. Harland, S.O. Agrell, A.H. Cook, and N.F. Hughes1978, Cambridge: Cambridge University Press. 493 pp.

100. Huston, D.L., Sie, S.H., Suter, G.F., Cooke, D.R., and Both, R.A., *Trace elements in sulfide minerals from eastern Australian volcanic-hosted massive sulfide deposits; Part I, Proton microprobe analyses of pyrite, chalcopyrite, and sphalerite, and Part II, Selenium levels in pyrite; comparison with delta 34 S values and implications for the*

source of sulfur in volcanogenic hydrothermal systems. Economic Geology, **1995**. 90(5), p.1167-1196.

101. Savage, K.S., Stefan, D., and Lehner, S.W., *Impurities and heterogeneity in pyrite: Influences on electrical properties and oxidation products.* Applied Geochemistry, **2008**. 23(2), p.103-120.

102. Zeghbroeck, B.V. *Principals of Semiconductor Devices*. 29/03/2011 [cited 2012 15/03]; Available from: http://ecee.colorado.edu/~bart/book/.

103. Laird, J.S., Johnson, B.C., Ganesan, K., Kandasamy, S., Davidson, G., Borg, S., and Ryan, C.G., *Impurity mapping in sulphide minerals using Time-resolved Ion Beam Induced Current imaging.* Nuclear Instruments and Methods in Physics Research Section B: Beam Interactions with Materials and Atoms, **2010**. 268(11-12), p.1903-1910.

104. Schieck, R., Hartmann, A., Fiechter, S., Könenkamp, R., and Wetzel, H., *Electrical properties of natural and synthetic pyrite (FeS2) crystals.* Journal of Materials Research, **1990**. 5(07), p.1567-1572.

105. Hsu-Kim, H., Mullaugh, K.M., Tsang, J.J., Yucel, M., and Luther, G.W., 3rd, *Formation of Zn- and Fe-sulfides near hydrothermal vents at the Eastern Lau Spreading Center: implications for sulfide bioavailability to chemoautotrophs.* Geochem Trans, **2008**. 9, p.6.

106. Ruppert, D., *Statistical Analysis, Special Problems of: Transformations of Data*, in *International Encyclopedia of the Social & Behavioral Sciences*, J.S. Editors-in-Chief: Neil and B.B. Paul, Editors. 2001, Pergamon: Oxford. p. 15007-15014.

107. McKibben, M.A., *MINING GEOLOGY | Hydrothermal Ores*, in *Encyclopedia of Geology*, C.S. Editors-in-Chief: Richard, L.R.M. Cocks, and R.P. Ian, Editors. 2005, Elsevier: Oxford. p. 628-637.

108. Haymon, R.M., *TECTONICS | Hydrothermal Vents At Mid-Ocean Ridges*, in *Encyclopedia of Geology*, C.S. Editors-in-Chief: Richard, L.R.M. Cocks, and R.P. Ian, Editors. 2005, Elsevier: Oxford. p. 388-395.

109. Orem, W.H. and Finkelman, R.B., *7.08 - Coal Formation and Geochemistry*, in *Treatise on Geochemistry*, D.H. Editors-in-Chief: Heinrich and K.T. Karl, Editors. 2003, Pergamon: Oxford. p. 191-222.

110. Loftus-Hills, G. and Solomon, M., *Cobalt, nickel and selenium in sulphides as indicators of ore genesis.* Mineralium Deposita, **1967**. 2(3), p.228-242.

111. Price, B.J., *Minor elements in pyrites from the smithers map area, b.c. and exploration applications of minor element studies*, in *Dept. of Geology*1972, The university of British Columbia. p. 280.

112. Bralia, A., Sabatini, G., and Troja, F., *A revaluation of the Co/Ni ratio in pyrite as geochemical tool in ore genesis problems.* Mineralium Deposita, **1979**. 14(3), p.353-374.

113. Wilson, S.A., Ridley, W.I., and Koenig, A.E., *Development of sulfide calibration standards for the laser ablation inductively-coupled plasma mass spectrometry technique.* Journal of Analytical Atomic Spectrometry, **2002**. 17(4), p.406-409.

114. *GENESIS SPECTRUM*, 2006, EDAX INC.

115. Pitcairn, I.K., Teagle, D.A.H., Craw, D., Olivo, G.R., Kerrich, R., and Brewer, T.S., *Sources of Metals and Fluids in Orogenic Gold Deposits: Insights from the Otago and Alpine Schists, New Zealand.* Economic Geology, **2006**. 101(8), p.1525-1546.

116. Thomas, H.V., Large, R.R., Bull, S.W., Maslennikov, V., Berry, R.F., Fraser, R., Froud, S., and Moye, R., *Pyrite and Pyrrhotite Textures and Composition in Sediments, Laminated Quartz Veins, and Reefs at Bendigo Gold Mine, Australia: Insights for Ore Genesis.* Economic Geology, **2011**. 106(1), p.1-31.

117. Bannister, F., *The distinction of pyrite from marcasite in nodular growths.* Mineralogical Magazine, **1932**. 23(138), p.179-187.

118. Van Horn, F.R. and Van Horn, K.R., *X-ray study of pyrite or marcasite concretions in the rocks of the Cleveland, Ohio, quad rangles.* American Mineralogist, **1933**. 18, p.288-94.

119. Nelson, W.J. and Jacobson, R.J., *Pennsylvanian Subsystem and Permian System*, in *Geology of Illinois*, D.R. Kolata and C. Nimz, Editors. 2010, University of Illinois at Urbana-Champaign, Institute of Natural Resource Sustainability, Illinois State Geological Survey.

120. Calvo, M. and Sevillano, E., *Pyrite crystals from Soria and La Rioja provinces Spain.* The Mineralogical Record, **1989**. 20(6), p.451-456.

121. Alonso-Azcárate, J., Boyce, A.J., Bottrell, S.H., Macaulay, C.I., Rodas, M., Fallick, A.E., and Mas, J.R., *Development and use of in situ laser*

sulfur isotope analyses for pyrite-anhydrite geothermometry: An example from the pyrite deposits of the Cameros Basin, NE Spain. Geochimica et Cosmochimica Acta, **1999**. 63(3–4), p.509-513.

122. Alonso, A., Rodas, Bottrell, Raiswell, Velasco, and Mas, *Pathways and distances of fluid flow during low-grade metamorphism: evidence from pyrite deposits of the Cameros Basin, Spain.* Journal of Metamorphic Geology, **1999**. 17(4), p.339-348.

123. Alonso-Azcarate, J., Bottrell, S., and Tritlla, J., *Sulfur redox reactions and formation of native sulfur veins during low grade metamorphism of gypsum evaporites, Cameros Basin (NE Spain).* Chemical Geology, **2001**. 174(4), p.389-402.

124. Thompson, T., *Precious metals in the Leadville mining district, Colorado.* US Geol Surv Bull, **1857**, p.F32-F49.

125. Groves, D.I., Goldfarb, R.J., Gebre-Mariam, M., Hagemann, S., and Robert, F., *Orogenic gold deposits: a proposed classification in the context of their crustal distribution and relationship to other gold deposit types.* Ore Geology Reviews, **1998**. 13(1), p.7-27.

126. Abbot, J. and Ekers, B., *Mineral resource estimates for the Paulsens Gold Mine*, in *Unpublished Technical Report,* 2010, Intrepid Mines Pty Ltd. p. 65.

127. Eckel, E.B., Cobban, R.R., Collins, D.S., Foord, E.E., Kile, D.E., Modreski, P.J., and Murphy, J.A., *Minerals of Colorado*. Vol. 92. 1997: Fulcrum Publishing.

128. Dietrich, A., Lehmann, B., and Wallianos, A., *Bulk rock and melt inclusion geochemistry of Bolivian tin porphyry systems.* Economic Geology, **2000**. 95(2), p.313-326.

129. Imai, H., Kawasaki, M., Yamaguchi, M., and Takahashi, M., *Mineralization and paragenesis of the Huanzala Mine, central Peru.* Economic Geology, **1985**. 80(2), p.461-478.

130. Morales Ruano, S., Both, R., and Golding, S., *A fluid inclusion and stable isotope study of the Moonta copper–gold deposits, South Australia: evidence for fluid immiscibility in a magmatic hydrothermal system.* Chemical Geology, **2002**. 192(3), p.211-226.

131. Wilson, P.N. and Parry, W., *Thermal and Chemical Evolution of Hydrothermal Fluids at the Ophir Hill Mine Ophir District, Utah*, in *Energy and mineral Resources of Utah,* 1990, Utah Geological Association Publicaition 18.